Synthesis of IV-VI Transition Metal Carbide and Nitride Nanoparticles Using a Reactive Mesoporous Template for Electrochemical Hydrogen Evolution Reaction

Dissertation by

Nawal Alhajri

In Partial Fulfillment of the Requirements

For the Degree of

Doctor of Philosophy

King Abdullah University of Science and Technology

Thuwal, Kingdom of Saudi Arabia

EXAMINATION COMMITTEE APPROVALS FORM

The dissertation of Nawal Alhajri is approved by the examination committee.

Committee Chairperson Kazuhiro Takanabe

Committee Member Yu Han

Committee Member Jr-Hau He

Committee Member Harun Tüysüz

ABSTRACT

Synthesis of IV-VI Transition Metal Carbide and Nitride Nanoparticles Using a Reactive Mesoporous Template for Electrochemical Hydrogen Evolution Reaction

Nawal Alhajri

Interstitial carbides and nitrides of early transition metals in Groups IV-VI exhibit platinum-like behavior which makes them a promising candidate to replace noble metals in a wide variety of reactions. Most synthetic methods used to prepare these materials lead to bulk or micron size powder which limits their use in reactions in particular in catalytic applications. Attempts toward the production of transition metal carbide and nitride nanoparticles in a sustainable, simple and cheap manner have been rapidly increasing. In this thesis, a new approach was presented to prepare nano-scale transition metal carbides and nitrides of group IV-VI with a size as small as 3 nm through the reaction of transition metal precursor with mesoporous graphitic carbon nitride (mpg-C_3N_4) that not only provides confined spaces for nanoparticles formation but also acts as a chemical source of nitrogen and carbon.

The produced nanoparticles were characterized by powder X-ray diffraction (XRD), temperature-programmed reaction with mass spectroscopy (MS), CHN elemental analyses, thermogravimetric analyses (TGA), nitrogen sorption, X-ray photoelectron spectroscopy (XPS), and transmission electron microscopy (TEM).

The effects of the reaction temperature, the ratio of the transition metal precursor to the

reactive template (mpg-C_3N_4), and the selection of the carrier gas (Ar, N_2, and NH_3) on the resultant crystal phases and structures were investigated.

The results indicated that different tantalum phases with cubic structure, TaN, Ta_2CN, and TaC, can be formed under a flow of nitrogen by changing the reaction temperatures. Two forms of tantalum nitride, namely TaN and Ta_3N_5, were selectively formed under N_2 and NH_3 flow, respectively. Significantly, the formation of TaC, Ta_2CN, and TaN can be controlled by altering the weight ratio of the C_3N_4 template relative to the Ta precursor at 1573 K under a flow of nitrogen where high C_3N_4/Ta precursor ratio generally resulted in high carbide content rather than nitride.

In addition, the reactivity of the transition metals of group IV-VI with the reactive template was investigated under a flow of N_2 at different temperatures in the range of 1023 to 1573 K while keeping the weight ratio constant at 1:1. The results show that Ti, V, Nb, Ta, and Cr reacted with mpg-C_3N_4 at 1023 K to form nitride phase with face centered cubic structure. The nitride phase destabilized at higher temperature ≥1223 K through the reaction with the remaining carbon residue originated from the decomposition of the template to form carbonitride and carbide phases. Whereas, Mo and W produce a hexagonal structure of carbide irrespective of the applying reaction temperature. The tendency to form transition metal nitrides and carbides at 1023 K was strongly driven by the free energy of formation. The observed trend indicates that the free energy of formation of nitride is relatively lower for group IV and V transition metals, whereas the carbide phase is thermodynamically more favorable for group VI, in particular for Mo and W. The thermal stability of nitride decreases at high temperature due to the evolution of nitrogen gas.

The electrocatalytic activities of the produced nanoparticles were tested for hydrogen evolution reaction in acid media and the results demonstrated that molybdenum carbide nanoparticles exhibited the highest HER current with over potential of 100 mV vs. RHE, among the samples prepared in this study. This result is attributed to the sufficiently small particle size (8 nm on average) and accordingly high surface area (308 m^2 g^{-1}). Also, the graphitized carbon layer with a thickness of 1 nm on its surface formed by this synthesis provides excellent electron pathway to the catalyst which will improve the rate of electron transfer reaction.

Table of Contents

CHAPTER 1

Introduction

Transition metal carbides and nitrides of groups (IV-VI) have been attracting much attention because of their distinctive chemical and physical properties. They are refractory compounds with high melting points, exhibit resistance against corrosion and they demonstrate electric, magnetic and catalytic characteristics which make them potential substitute for noble metals in various applications in material science and heterogeneous catalysis.[1, 2, 3, 4]

Transition metal nitrides (TiN and CrN) are used as hard coatings, another nitride such as VN is used as refractory materials and as an electrode for supercapacitor.[1,5] NbC displays high conductivity which makes it suitable for many applications such as mechanical, chemical, and microelectronic industries.[6] TiC is broadly applied for cutting materials, abrasives and wear-resistant materials.[6] Other carbides show applications in catalysis such as TaC, NbC, and VN. WC and Mo_2C exhibit excellent catalytic properties similar or suppress to those of platinum in various reactions.[5,7]

Early transition metal carbides and nitrides of groups (IV-VI) are interstitial compounds with close-packed structure where carbon or nitrogen occupies specific interstitial sites of metal lattice.[1-3, 8, 9]

The typical crystalline structures of these compounds are face-centered cubic (fcc), hexagonal closed packed (hcp) and simple hexagonal (hex) structure. The largest interstitial site is an octahedral site in fcc and hcp which is occupied by carbon and nitrogen. As for simple hexagonal structure, carbon and nitrogen fit into trigonal prismatic sites (Fig.

1). In general, geometric and electronic factors found to be responsible for formulating the structures of carbides and nitrides. As for geometric aspect, studies show that, interstitial compounds can be formed when the ratio of the radius of the non-metal atom to the radius of the metal atom is less than 0.59.[2, 3,8,10]

The electronic factor was explained using the Engel-Brewer theory, which states that the resultant structure depends on the number of sp electrons. The metal Mo possesses a bcc structure, whereas its carbide Mo_2C and nitride Mo_2N are hcp and fcc, respectively. The structure changes from bcc to hcp to fcc with increasing amounts of sp electrons. The incomplete filling of the d-band for transition metals of group IV and V drives them to receive a high proportion of sp electrons and accordingly produce an fcc structure. However, transition metals in group VI possess an hcp structure with metal-rich stoichiometry because of the increased d-band filling.[2, 9, 11] Also, the formation of high stoichiometry was in accordance with an attempt to avoid filling of antibonding levels in the metal bands (Fig. 2).[12]

Interstitial carbides and nitrides exhibit ceramic-like behavior such as hardness, high melting points, thermal and chemical stability, thus, they are refractory compounds.

They show metal-like properties when it comes to electric and magnetic properties such as high thermal and electrical conductivity.[8, 13] Thus, the bonding in these compounds is a combination of metallic, covalent and ionic components.[3, 8]

Recent studies proved that the bonding in interstitial carbides and nitrides is most likely described as metallic rather than ionic or covalent.[14]

It is well known that the electronic properties of metal carbides and nitrides determine their reactivity and stability.[12, 14]

The modification occurred in metal d-band upon carbide and nitride formation is responsible for the excellent catalytic properties.[2] Studies confirmed that hybridization between d-orbital of the metal and p-orbital of non-metal causes an expansion of metal lattice which resulted in a contraction of the metal d-band. Consequentially, this contraction leads to a higher density of states (DOS) near the Fermi level approaching the d-band of Pt.[3, 9, 15, 16]

There are many conventional processes to synthesize transition metal carbides including gaseous metal-containing reagents such as metal carbonyl complexes, pyrolysis of metal complexes, electrochemical methods, metathesis reactions, gas–solid reactions, carbothermal reduction applied by microwave and solution state methods.[16, 17]

For example, TiC was prepared by the carbothermal reduction process through reaction of TiO_2 with carbon black, at high temperature (1700–2100 $^{\circ}$C). Also, gas phase reaction between $TiCl_4$ and appropriate gaseous hydrocarbons or pyrolysis of propylene gas at 1300 $^{\circ}$C can be used to obtain TaC phase. In addition, reaction of metallic magnesium with sodium carbonate and tantalum pentachloride at 600 $^{\circ}$C was also applied to prepare TaC with an average size of 40 nm.[6]

The traditional methods to prepare transition metal nitrides include the reactions of metals or metal oxides with nitrogen sources (such as ammonia or nitrogen) at high temperature (from 800 $^{\circ}$C up to 2000 $^{\circ}$C).[16]

Other approaches such as solid-state metathesis (SSM) route by using metal halides and Li_3N or NaN_3 (440–850 °C) or by reacting metal oxides with a-$C_3N_{3.69}$ or Li_3N (600–1200 °C) were applied for metal nitride production. Ammonolysis of organometallic precursors was also used to produce nitrides at relatively low temperature. Autoclave process was also used to prepare the following nanocrystals TiN, NbN, and TaN at 350 °C, through the reaction of transition metal chlorides with sodium azid.[6]

The traditional approaches used to synthesize transition metal carbides and nitrides limit their use in catalytic application because they suffer from many drawbacks such as high-energy consumption, large particle size, poor crystallinity, incomplete reaction which resulted in O, C and N contaminations.[17] Other synthetic methods can be used to produce nanoparticles at relatively moderate temperature but the manipulation over size and shape still remains difficult. Thus, considerable attention has been focused on developing effective methods that can directly allow switch from nitrides to carbides as well as provide a control over size and shape of the produced nanoparticles.

A possible approach reported in the literature is the urea-glass route, a sol-gel based process reported by Giordano.[1, 5, 18] This research presents a unique method to shift from nitrides to carbides Mo_2N to Mo_2C and W_2N to WC, respectively, simply by altering the ratio of urea to metal precursor. Low urea to metal ratio tends to produce nitride whereas carbide obtained at higher urea to metal ratio.[5, 18, 19] This method was applied to other transition metals and resulted in the following products TiN, VN, NbN, GaN, and TiC(N). However, Cr_3C_2 and NbC compounds were not possible to be obtained by urea glass rout method.[5,19]

Antonietti's research demonstrated the use of mesoporous graphite mpg-C_3N_4[20-23] to synthesize metal nitrides nanoparticles such as TiN,[24] VN,[25] GaN, Ta_3N_5,[21, 26] and ternary Al-Ga-N and Ti-V-N[27] nanoparticles. Utilizing mpg-C_3N_4 approach to synthesize transition metal carbides and nitride nanoparticles is a distinctive method because the template acts as confinement for particle growth and as a source of carbon and nitrogen. The template completely decomposes into reactive C and N fragments at 950 K, under inert atmosphere (e.g., N_2 or Ar)[28] while another conventional carbon requires air to be gasified.[21] During the synthesis no need for isolation or purification step due to the complete thermal decomposition of C_3N_4. Also, this approach provides control over size and shape of the resultant nanoparticles as they reflect the size and shape of the original silica template that used to generate mpg-C_3N_4. Applying different silica templates in C_3N_4 preparation result in various shapes and sizes of the pores which consequently produce different morphologies of the transition metal carbide and nitride.[21, 28, 29] In addition, the size and shape of the produced nanoparticles can be adjusted by controlling the filling rate of the nonreactor. The studies show that the control over size is associated with the concentration of metal precursor solution used during the synthesis. Concentrated solution yields larger particle size whereas smaller particle size is obtained from diluted one.[20]

As for catalytic applications, transition metal carbides and nitrides display catalytic properties comparable to those of noble metals in various reactions, including hydrogenolysis, hydrogenation, dehydrogenation, isomerization,[30] hydrodesulfurization (HDS), hydrodenitrogenation (HDN),[13] ammonia synthesis,[31] ammonia decomposition,[7] electrochemical reactions (Fig. 3).[15,16,24]

Driven by the need to alleviate environmental pollution caused by fossil fuel, technologies with higher efficiency and lower emissions are being developed and deployed in various industrial and consumer-centric applications. Hydrogen based technologies for transportation and power generation applications have been proposed and have the potential to achieve significant market penetration, due primarily to the fact that they are friendly to the environment and have high energy conversion efficiency.[32]

Currently, steam reforming or partial oxidation of methane is the most applied process to generate hydrogen from fossil fuels which cause the emission of greenhouse gasses such as carbon dioxide. Hence, developing effective methods to produce hydrogen with low cost from existing resources has been a challenge. Water electrolysis is a desired technology that generates hydrogen with greenhouse-gas-free in particular when the applied electricity is coming from renewable energy sources such as sunlight, the wind, rain and geothermal energy (Fig. 4).[16, 33, 34]

Electrolytic production of hydrogen from water is achieved through hydrogen evolution reaction which is the most extensively considered electrochemical reaction that requires an active and stable electrocatalyst. To date, Pt group metals are the most active and stable electrocatalysts that produce hydrogen with low overpotential. However, noble metals are scarce and expensive which drives researches to develop alternative inexpensive and abundant materials. Most non-noble metals are unstable in acidic media where high electrocatalytic activity of HER is expected.[35-37] Recently, many efforts and increased attention have been devoted to transition metal carbides, nitrides, sulfides, and phosphides.[38-46]

The remarkable electrocatalytic activities of molybdenum carbides, nitrides, sulfides and phosphides were due to distinct electronic structure resulted from the incorporation of the non-metal atoms in the metal lattice. The combination of good activities and high stability of these materials in acidic media makes them a good candidate to replace Pt group metals in various catalytic reactions.[40, 46, 47]

Experimental and theoretical investigations of early transition metal-based compounds were carried out to study their electronic structure and accordingly evaluate their catalytic activities.[16]

The study shows that early transition metals like molybdenum are inexpensive materials, but they make a strong bond with adsorbates which increase the activation energy (Fig. 5). Thus, alteration the electronic structure of the early transition metals through, the formation of carbides, nitrides, phosphides, and sulfides leads to significant improvement in the electrocatalytic activities compared to the original phase of the transition metals. Developing and designing non-noble electrocatalysts with moderate metal-hydrogen bond and high stability has been a widely studied option.[48,49]

The electrocatalytic activities of carbide materials depend on their surface composition and conditions which are strongly related to their synthetic methods.[50] The traditional approaches used to synthesize transition metal carbides resulted in microparticles which decrease the rate of electron transfer reaction. Literature show many attempts towards developing a new method to prepare nanoscale molybdenum carbide.[17] In this regard, Mo_2C/carbon nanotube (CNT) composites were reported by Chen et al. who synthesized the material by carburization process. The prepared composite was tested for HER which

high catalytic performance with an overpotential of 63 mV at 1 mA cm^{-2}, which considered to be the highest reported HER performance of molybdenum carbide.[40] Also, nanoporous Mo_2C nanowires demonstrated by Lei showed higher HER catalytic current with low overpotential .[38] In addition, Yang reported the synthesis of molybdenum carbide supported on graphene and the high activity of the produced nanoparticles was ascribed to the intimate interaction between Mo_2C and graphene.[51]

In this thesis, a general synthetic procedure was presented for the first time for preparing a whole class of early transition metal nitride, carbonitride and carbide nanoparticles of group IV, V, and VI by applying C_3N_4 template approach (Fig. 6).

A systematic study that changes the precursor ratio with respect to the reactive template, the synthesis temperature, and the carrier gas (N_2, Ar, NH_3) was performed as described in the third chapter for the synthesis of tantalum nitride and carbide nanoparticles.

Also, during the synthesis, some of the transition metal tend to bind to nitrogen fragments while other metals prefer to react with active carbon species. Thus, I investigated the reactivity of the transition metals (Ti, V, Nb, Ta, Cr, Mo, and W) with mpg-C_3N_4 under nitrogen flow at 1023 K while keeping the weight ratio of the transition metal to the template constant at 1:1 as described in the second chapter.

As for the electrochemical hydrogen evolution reaction, in the fourth chapter, a novel nanocomposite of molybdenum carbide and carbon was prepared through the reaction of a molybdenum precursor with mpg-C_3N_4 and its electrocatalytic activity was measured for

HER in acidic media and compared with the performance of previously reported bulk materials.

This study proved the effectiveness of such method to produce different phases of interstitial nitride, carbonitride and carbide nanoparticles which could be applied accordingly in a wide range of applications in chemistry and material science.

References

(1) Giordano, C.; Antonietti, M. *Nano Today* **2011**, *6*, 366.

(2) Chen, J. G. *Chemical Reviews* **1996**, *96*, 1477.

(3) Ham, D.; Lee, J. *Energies* **2009**, *2*, 873.

(4) Claridge, J. B.; York, A. P. E.; Brungs, A. J.; Green, M. L. H. *Chemistry of Materials* **1999**,*12*, 132.

(5) Giordano, C.; Erpen, C.; Yao, W.; Milke, B.; Antonietti, M. *Chemistry of Materials* **2009**, *21*, 5136.

(6) Zhu, Y.; Li, Q.; Mei, T.; Qian, Y. *Journal of Materials Chemistry* **2011**, *21*, 13756.

(7) Alexander, A.-M.; Hargreaves, J. S. J. *Chemical Society Reviews* **2010**, *39*, 4388.

(8) Pierson, H. **June 1996**.

(9) Oyama, S. T. *Catalysis Today* **1992**, *15*, 179.

(10) Toth, L. E. **1971**.

(11) Liu, Y.; Kelly, T. G.; Chen, J. G.; Mustain, W. E. *ACS Catalysis* **2013**, *3*, 1184.

(12) Ted Oyama, S. *Journal of Solid State Chemistry* **1992**, *96*, 442.

(13) Ramanathan, S.; Oyama, S. T. *The Journal of Physical Chemistry* **1995**, *99*, 16365.

(14) Oyama, S. T.; Haller, G. L. In *Catalysis: Volume 5*; Bond, G. C., Webb, G., Eds.; The Royal Society of Chemistry: 1982; Vol. 5, p 333.

(15) Dong, S.; Chen, X.; Zhang, X.; Cui, G. *Coordination Chemistry Reviews* **2013**, *257*, 1946.

(16) Chen, W.-F.; Muckerman, J. T.; Fujita, E. *Recent developments in transition metal carbides and nitrides as hydrogen evolution electrocatalysts*, 2013.

(17) Li, P. G.; Lei, M.; Sun, Z. B.; Cao, L. Z.; Guo, Y. F.; Guo, X.; Tang, W. H. *Journal of Alloys and Compounds* **2007**, *430*, 237.

(18) Giordano, C.; Erpen, C.; Yao, W.; Antonietti, M. *Nano Letters* **2008**, *8*, 4659.

(19) Yao, W.; Makowski, P.; Giordano, C.; Goettmann, F. *Chemistry – A European Journal* **2009**, *15*, 11999.

(20) Fischer, A.; Antonietti, M.; Thomas, A. *Advanced Materials* **2007**, *19*, 264.

(21) Fukasawa, Y.; Takanabe, K.; Shimojima, A.; Antonietti, M.; Domen, K.; Okubo, T. *Chemistry – An Asian Journal* **2011**, *6*, 103.

(22) Groenewolt, M.; Antonietti, M. *Advanced Materials* **2005**, *17*, 1789.

(23) Thomas, A.; Goettmann, F.; Antonietti, M. *Chemistry of Materials* **2008**, *20*, 738.

(24) Chen, J.; Takanabe, K.; Ohnishi, R.; Lu, D.; Okada, S.; Hatasawa, H.; Morioka, H.; Antonietti, M.; Kubota, J.; Domen, K. *Chemical Communications* **2010**, *46*, 7492.

(25) Zhao, H.; Lei, M.; Yang, X. a.; Jian, J.; Chen, X. *Journal of the American Chemical Society* **2005**, *127*, 15722.

(26) Yuliati, L.; Yang, J.-H.; Wang, X.; Maeda, K.; Takata, T.; Antonietti, M.; Domen, K. *Journal of Materials Chemistry* **2010**, *20*, 4295.

(27) Fischer, A.; Müller, J. O.; Antonietti, M.; Thomas, A. *ACS Nano* **2008**, *2*, 2489.

(28) Thomas, A.; Fischer, A.; Goettmann, F.; Antonietti, M.; Muller, J.-O.; Schlogl, R.; Carlsson, J. M. *Journal of Materials Chemistry* **2008**, *18*, 4893.

(29) Ohnishi, R.; Takanabe, K.; Katayama, M.; Kubota, J.; Domen, K. *The Journal of Physical Chemistry C* **2012**, *117*, 496.

(30) Neylon, M. K.; Choi, S.; Kwon, H.; Curry, K. E.; Thompson, L. T. *Applied Catalysis A: General* **1999**, *183*, 253.

(31) Mazumder, B.; Hector, A. L. *Journal of Materials Chemistry* **2009**, *19*, 4673.

(32) Alhajri, N. S.; Yoshida, H.; Anjum, D. H.; Garcia-Esparza, A. T.; Kubota, J.; Domen, K.; Takanabe, K. *Journal of Materials Chemistry A* **2013**, *1*, 12606.

(33) Turner, J. A. *Science* **2004**, *305*, 972.

(34) Garcia-Esparza, A. T.; Cha, D.; Ou, Y.; Kubota, J.; Domen, K.; Takanabe, K. *ChemSusChem* **2013**, *6*, 168.

(35) Trasatti, S. *Journal of Electroanalytical Chemistry and Interfacial Electrochemistry* **1972**, *39*, 163.

(36) Santos, E.; Schmickler, W. *ChemPhysChem* **2006**, *7*, 2282.

(37) Norskov, J. K.; Bligaard, T.; Rossmeisl, J.; Christensen, C. H. *Nat Chem* **2009**, *1*, 37.

(38) Liao, L.; Wang, S.; Xiao, J.; Bian, X.; Zhang, Y.; Scanlon, M. D.; Hu, X.; Tang, Y.; Liu, B.; Girault, H. H. *Energy & Environmental Science* **2014**, *7*, 387.

(39) Chen, W. F.; Wang, C. H.; Sasaki, K.; Marinkovic, N.; Xu, W.; Muckerman, J. T.; Zhu, Y.; Adzic, R. R. *Energy & Environmental Science* **2013**, *6*, 943.

(40) Pan, L. F.; Li, Y. H.; Yang, S.; Liu, P. F.; Yu, M. Q.; Yang, H. G. *Chemical Communications* **2014**, *50*, 13135.

(41) Yan, Y.; Xia, B.; Qi, X.; Wang, H.; Xu, R.; Wang, J.-Y.; Zhang, H.; Wang, X. *Chemical Communications* **2013**, *49*, 4884.

(42) Xie, J.; Li, S.; Zhang, X.; Zhang, J.; Wang, R.; Zhang, H.; Pan, B.; Xie, Y. *Chemical Science* **2014**, *5*, 4615.

(43) Voiry, D.; Yamaguchi, H.; Li, J.; Silva, R.; Alves, D. C. B.; Fujita, T.; Chen, M.; Asefa, T.; Shenoy, V. B.; Eda, G.; Chhowalla, M. *Nat Mater* **2013**, *12*, 850.

(44) Yan, Y.; Xia, B.; Xu, Z.; Wang, X. *ACS Catalysis* **2014**, *4*, 1693.

(45) Xiao, P.; Sk, M. A.; Thia, L.; Ge, X.; Lim, R. J.; Wang, J.-Y.; Lim, K. H.; Wang, X. *Energy & Environmental Science* **2014**, *7*, 2624.

(46) Kibsgaard, J.; Jaramillo, T. F. *Angewandte Chemie International Edition* **2014**, *53*, 14433.

(47) Tokash, J. C.; Logan, B. E. *International Journal of Hydrogen Energy* **2011**, *36*, 9439.

(48) Liu, P.; Rodriguez, J. *Catalysis Letters* **2003**, *91*, 247.

(49) Greeley, J. P.; Jaramillo, T.; Bonde, J.; Chorkendorff, I.; Nørskov, J. K. *Nature Materials* **2006**, *5*, 909.

(50) Alhajri, N. S.; Anjum, D. H.; Takanabe, K. *Journal of Materials Chemistry A* **2014**, *2*, 10548.

(51) Pan, L. F.; Li, Y. H.; Yang, S.; Liu, P. F.; Yu, M. Q.; Yang, H. G. *Chemical Communications* **2014**, *50*, 13135.

List of figures

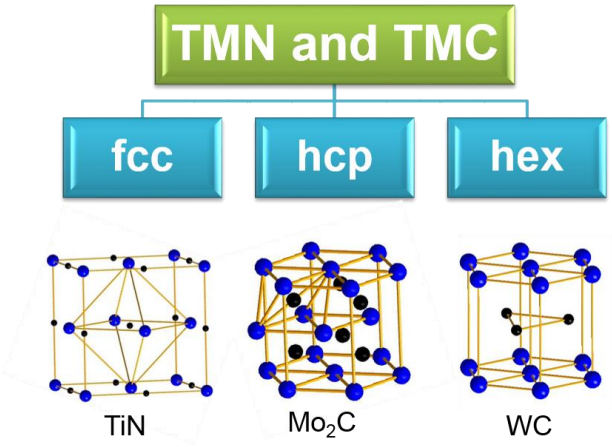

Fig. 1 Typical crystalline structures of transition metal carbide and nitride.

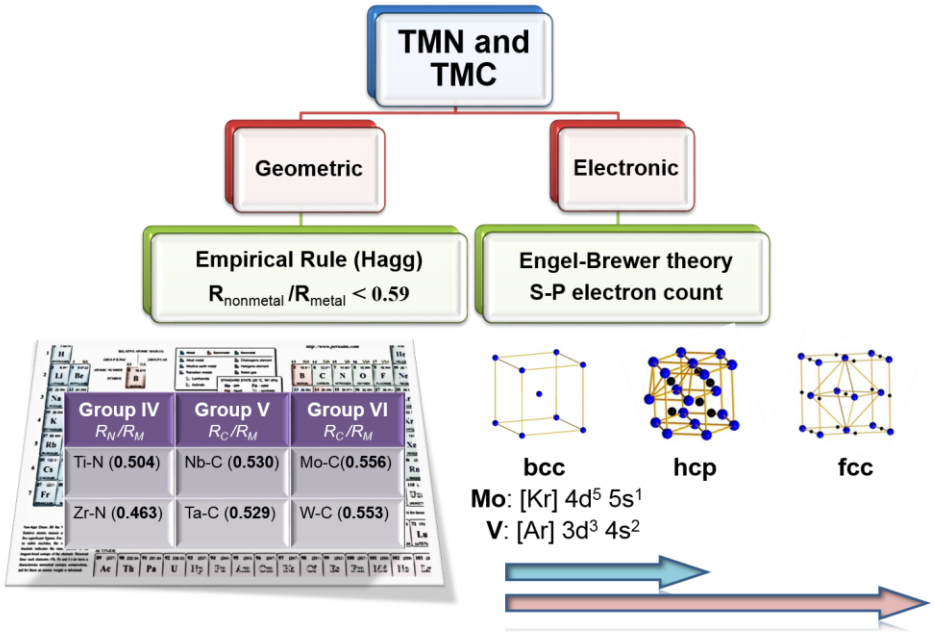

Fig. 2 Formation of transition metal carbide and nitride according to electronic and geometric factors.

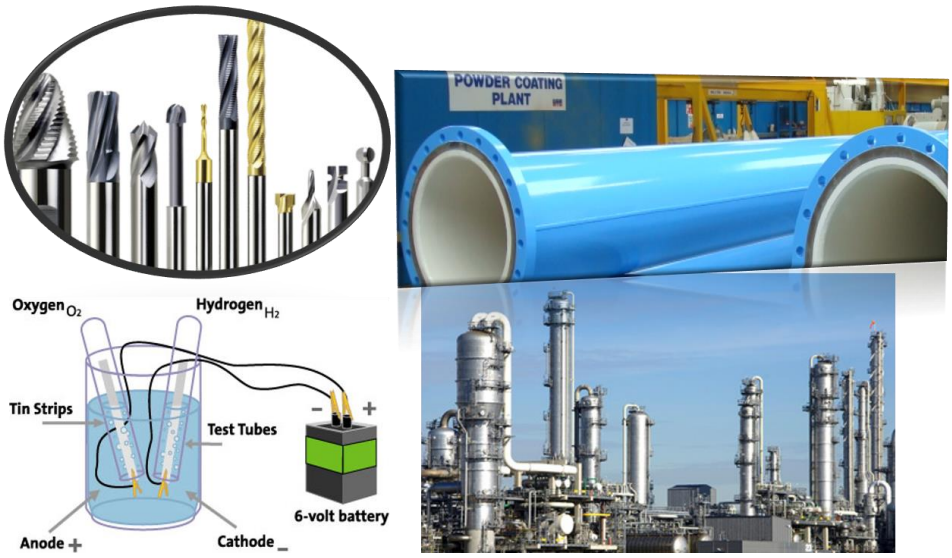

Fig. 3 General applications for transition metal nitride and carbide.

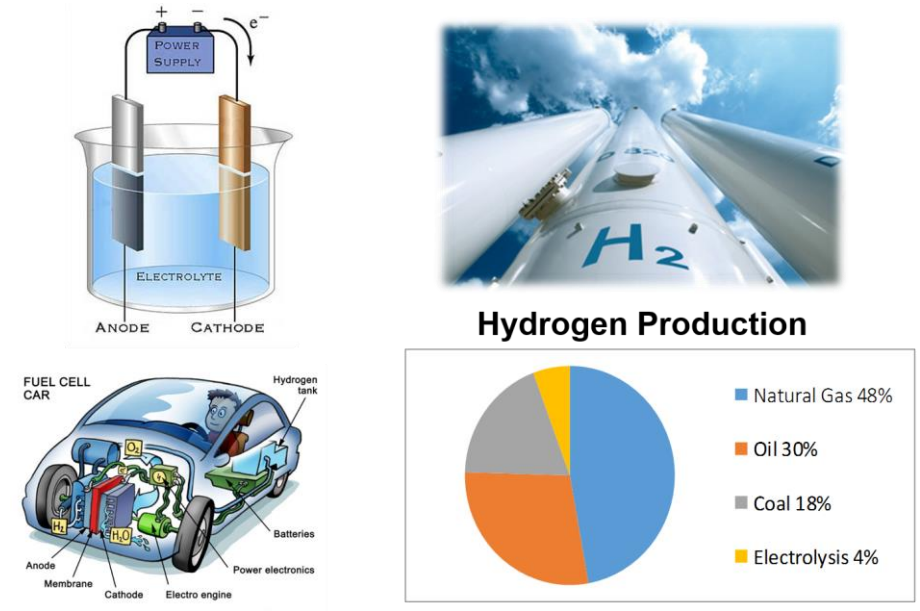

Fig. 4 Main approaches for hydrogen production.

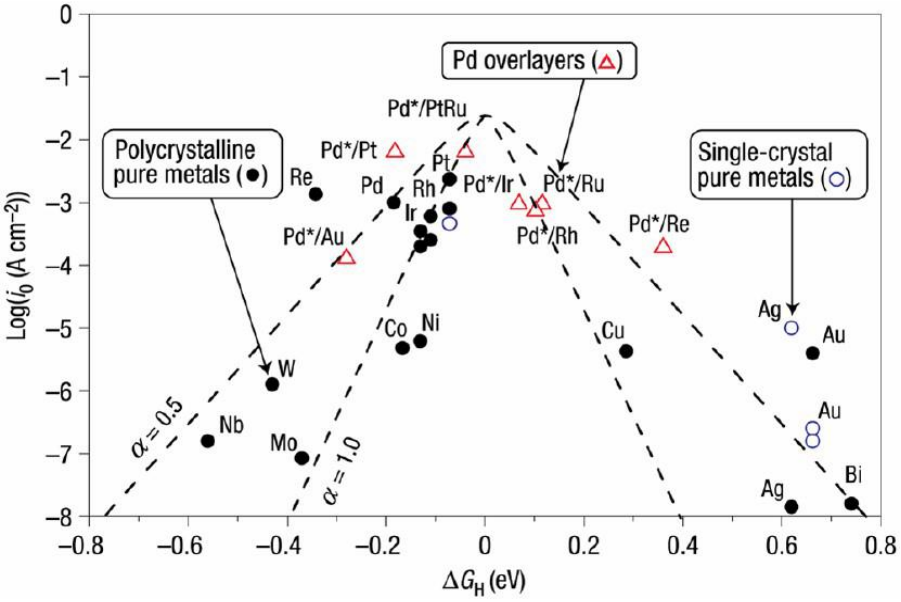

Fig. 5 Volcano plot for the HER for various pure metals.[49]

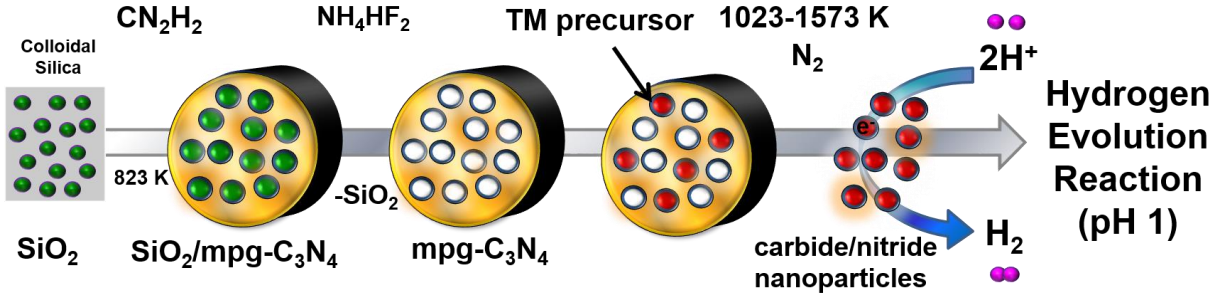

Fig. 6 Synthesis of interstitial nitride and carbide nanoparticles using mpg-C_3N_4.

CHAPTER 2

Synthesis of IV-VI transition metal carbide and nitride nanoparticles using a reactive mesoporous template

Introduction

Transition metal carbides and nitrides of groups (IV-VI) have been attracting much attention because of their distinctive chemical and physical properties. They are refractory compounds with high melting points, exhibit resistance against corrosion and they demonstrate electric, magnetic and catalytic characteristics which make them a potential substitute for noble metals in various applications in material science and heterogeneous catalysis.[1,2,3,4]

The catalytic activities of interstitial carbides and nitrides depend on their surface composition and conditions which are strongly related to their synthetic methods.[5,6]

There are many conventional processes to synthesize transition metal carbides including gaseous metal-containing reagents such as metal carbonyl complexes, pyrolysis of metal complexes, solution state methods, metathesis reactions, carbothermal reduction utilizing microwave.[5,7]

For example, TiC was prepared through the reaction of TiO_2 with carbon black, at high temperature (1700–2100 $^{\circ}$C). Tantalum carbide with a size of 40 nm was obtained by the reaction of metallic magnesium with sodium carbonate and tantalum pentachloride at 600 $^{\circ}$C.[8]

Literature show that the typical preparation method of tungsten and molybdenum carbides is temperature program reaction between metal oxide and mixture of methane and hydrogen at high temperature above 1100 °C.[9,10]

The traditional methods to prepare transition metal nitrides includes the reactions of metals or metal oxides with nitrogen sources (such as ammonia or nitrogen) at high temperature (from 800 °C up to 2000 °C).[5]

Other approaches such as solid-state metathesis (SSM) route by using metal halides and Li_3N or NaN_3 (440–850 °C) or by reacting metal oxides with a-$C_3N_{3.69}$ or Li_3N (600–1200 °C) were applied for metal nitride production. Ammonolysis of organometallic precursors was also used to produce nitrides at relatively low temperature. Autoclave process was also used to prepare the following nanocrystals TiN, NbN, and TaN at 350 °C, through the reaction of transition metal chlorides with sodium azid.[8]

The traditional approaches used to synthesize transition metal carbides and nitrides limit their use in catalytic application because they suffer from many drawbacks such as high-energy consumption, large particle size, poor crystallinity, an incomplete reaction which resulted in O, C and N contaminations.[7] Other synthetic methods can be used to produce nanoparticles at relatively moderate temperature, but the manipulation over size and shape still remains difficult. Thus, considerable attention has been focused on developing effective methods that can directly allow a switch from nitrides to carbides as well as provide a control over size and shape of the produced nanoparticles.

A possible approach reported in the literature is the urea-glass route, a sol-gel based process reported by Giordano.[1,11,12] This research presents a unique method to shift from nitrides

to carbides Mo_2N to Mo_2C and W_2N to WC, respectively, by altering the ratio of urea to metal precursor. Low urea to metal ratio tends to produce nitride whereas carbide obtained at higher urea to metal ratio.[11-13] This method was applied to other transition metals and resulted in the following products TiN, VN, NbN, GaN, and TiC(N). However, Cr_3C_2 and NbC compounds were not possible to be obtained by urea glass rout method.[12,13]

Antonietti's research demonstrated the use of mesoporous graphite mpg-C_3N_4[14-17] to synthesize metal nitrides nanoparticles such as TiN[18], VN[19], GaN[19], Ta_3N_5[15,20] and ternary Al-Ga-N and Ti-V-N[21] nanoparticles. Utilizing mpg-C_3N_4 approach to synthesize transition metal carbides and nitride nanoparticles is a distinctive method because the template acts as confinement for particle growth and as a source of carbon and nitrogen. The reactive template (g-C_3N_4) completely decomposes into reactive C and N fragments at approximately 950 K, under inert atmosphere (e.g., N_2 or Ar)[22] while another conventional carbon requires air to be gasified.[15] During the synthesis no need for isolation or purification step due to the complete thermal decomposition of C_3N_4. Also, this approach provides control over size and shape of the resultant nanoparticles as they reflect the size and shape of the original silica template that used to generate mpg-C_3N_4. Applying different silica templates in C_3N_4 preparation result in various shapes and sizes of the pores which consequently produce different morphologies of the transition metal carbide and nitride.[15,22,23] In addition, the size and shape of the produced nanoparticles can be adjusted by controlling the filling rate of the nonreactor. The studies show that the control over size is associated with the concentration of metal precursor solution used during the synthesis. Concentrated solution yields larger particle size whereas smaller particle size is obtained from diluted one.[14]

In this chapter, a general synthetic procedure was presented for the first time for preparing a whole class of early transition metal nitride and carbide nanoparticles of group IV, V and VI (Ti, V, Nb, Ta, Cr, Mo, and W) by applying C_3N_4 template approach. In addition, I studied the reactivity of the transition metals with mpg-C_3N_4 which acts as a chemical source of carbon or nitrogen for the formation of either nitride or carbide nanoparticles. This study proved the effectiveness of such method to produce different phases of interstitial nitride, carbonitride and carbide nanoparticles which could be applied accordingly in a wide range of applications in chemistry and material science.

Experimental

Synthesis of mesoporous graphitic carbon nitride

Transition metal carbide and nitride nanocrystals of groups IV, V, and VI were synthesized through the reaction of transition metal precursor with a mpg-C_3N_4 as a reactive template. Two templates of mpg-C_3N_4 were synthesized and used in this study. Following the reported procedure,[17] cyanamide (CA, 99% Aldrich) was mixed with an aqueous colloidal silica suspension composed of silica nanoparticles (LUDOX AS-30, 30 wt%, Aldrich) or (LUDOX SM-30, 30 wt%, Aldrich) while maintaining a 1:1 weight ratio of SiO_2 with respect to cyanamide. The mixture was heated at 313 K overnight. The obtained solid product was heated in a semi-closed crucible at 823 K for 4 h. In order to remove the silica, the final mixture was then thoroughly washed with a 4 M ammonium hydrogen difluoride (NH_4HF_2, ≥98.5% Fluka) aqueous solution followed by H_2O and ethanol.

Syntheses of transition metal carbide and nitride nanoparticles

The synthetic experiments were conducted at different temperatures in the range of 1023-1573 Kunder nitrogen flow while keeping the weight ratio of C_3N_4/metal precursor constant at 1:1. Typically, transition metal precursor was dissolved in ethanol. Then, a drop impregnation process was applied through immersing the pores of the template with the aforementioned solution. The final mixture was transferred to an alumina boat crucible and heated to different temperatures in the range of 1023 to 1573 K under a flow of 100 ml min^{-1} of N_2. Passivation process was applied before exposing the samples to ambient air by flowing 100 ml min^{-1} of 1% O_2 in He at room temperature. Caution is required during synthesis due to the release of hydrogen cyanide and cyanogen gasses resulted from thermal decomposition of C_3N_4.

Characterization

The synthesized samples were characterized using elemental analyses (C, H, and N), X-ray diffraction (XRD), N_2 sorption, thermogravimetric analyses (TGA), X-ray photoelectron spectroscopy (XPS), a temperature-programmed reaction with mass spectroscopy (MS), and transmission electron microscopy (TEM). Elemental analyses were performed using a Flash 2000 Thermo Scientific CHNS/O analyzer. The XRD patterns of the products were collected on a Bruker DMAX 2500 X-ray diffractometer equipped with a Cu Kα radiation source (λ = 0.154 nm). The N_2 sorption studies were conducted using a Micrometrics ASAP 2420 to determine the Brunauer–Emmett–Teller (BET) surface area, the Barrett–Joyner–Halenda (BJH) pore size, and the pore volume. The decomposition mechanism of the mpg-C_3N_4 template was investigated by detecting the

products in the gas phase using an OMNI Star (GSD320 O1) portable mass spectrometer equipped with a tungsten filament from Pfeiffer Vacuum. The mass spectrometer was connected at the furnace outlet to study the decomposition products under Ar flow of 100 ml min^{-1}. A Mettler- Toledo TGA/DSC1 Star system was utilized to carry out TGA under a 100 ml min^{-1} flow of air. XPS studies were carried out using a Kratos Axis Ultra DLD spectrometer equipped with a monochromatic Al Kα X-ray source (hν = 1486.6 eV) operating at 150 W, a multi-channel plate and a delay line detector under 1.0 $x10^{-9}$ Torr vacuum. The survey and high-resolution spectra were collected at fixed analyzer pass energies of 160 and 20 eV, respectively. A transmission electron microscope of model TITAN G^2 80-300 ST was used to characterize the sample morphology and to determine the particle size. The microscope was operated at an electron beam energy of 300 keV. Selected area electron diffraction (SAED) patterns were obtained to determine the inter-planar d-spacings of the crystalline phases present in the samples.

Results and Discussion

Characterization of the mpg-C_3N_4 template (AS-30)

The XRD pattern (Fig.1 A).shows a broad maximum peak at 27.3° with a d spacing of 0.33 nm, which well matches to the reported interlayer distance between the g-C_3N_4 sheets.[16] In order to determine the BET surface area and pore size, N_2 sorption experiments were carried out. The obtained graph is an IV isotherm according to the International Union of Pure and Applied Chemistry (IUPAC) and it shows a hysteresis loop confirming the mesoporous structure of the template. The BET surface area is 113 m^2 g^{-1}, and the pore

volume and average pore size were found to be 0.35 $cm^3\ g^{-1}$ and 10 nm, respectively. (Fig.1 B and C).

Characterization of the mpg-C_3N_4 template (SM-30)

The XRD pattern confirms the graphitic structure of the template (Fig.2 A). The elemental analysis suggests that the carbon nitride sample is nitrogen-rich as the carbon-to-nitrogen ratio is (0.55%) which found to be lower than the theoretical value of C_3N_4 (0.75%). This is due to the presence of C–NH_2, 2C–NH, and hydrogen bonded OH groups or absorbed water molecules on the surface.[24] N_2 sorption experiments were also performed and the BET surface area is 162 $m^2\ g^{-1}$ and the pore volume and average pore size is 0.35 $cm^3\ g^{-1}$ and 6 nm, respectively (Fig.2 B and C). The mass spectrum shows the produced gasses during the temperature-programmed decomposition of the mpg-C_3N_4 template under a flow of argon (100 ml min^{-1}) in the temperature range of 318 to 1573 K and at a heating rate of 14 K min^{-1} (Fig.2 D).The spectrum indicates the presence of three signals (27 amu), (28 amu) and (52 amu) at approximately 960 K, which corresponds to the formation of hydrogen cyanide, nitrogen and cyanogen respectively. In addition, C_3N_x residue was observed at the outlet and this experiment confirmed the complete volatilization of the template as there were no materials recovered at the end of the experiment. Based on the above findings, an equation (1), can be written as follows:[24]

$$2C_3N_{(4+x)}H_y \longrightarrow aN_2 + bHCN + cC_2N_2 + dC_3N_z \qquad (1)$$

Group IV (Ti)

Titanium nitride and carbonitride nanoparticles

The samples were synthesized under nitrogen flow at different temperatures from 1023 to 1573 K while keeping the ratio of mpg-C_3N_4/ TiF_4 at constant 1:1. The produced nanoparticles were characterized by XRD to determine the crystallite structure as shown in Fig.3. Scherrer equation was applied to obtain the crystallite size and listed in Table 1. The XRD pattern for the sample synthesized at 1023 K shows five major peaks 2θ= 36.7°(d=2.44315Å,(111)), 2θ=42.8°(d=2.10984Å,(200)), 2θ=62°(d=1.49369Å,(220)) , 2θ=74.4°(d=1.27326Å,(311)) and 2θ=78.3°(d=1.21939Å,(222)) that correspond to titanium nitride $(TiN)_{.88}$ (PDF-01-087-0630) that has a cubic structure with Fm-3m(225) space group.

The broadness of the peaks in the XRD pattern indicates that the powder is nanocrystalline material. Further increase of temperature to 1223 K, XRD pattern indicates the formation of mixtures of titanium nitride and carbonitride. Nitride phase $(TiN)_{.88}$ (PDF-01-087-0630) were detected at 2θ= 36.7°(d=2.44315Å,(111)), 2θ=42.7°(d=2.11336Å,(200)), 2θ=62.1°(d=1.49207Å,(220)) , 2θ=74.5°(d=1.27216Å,(311)) and 2θ=78.3°(d=1.21939Å,(222)). The XRD peaks were shifted to the high angel by about 0.2° with respect to the pure phase of $TiC_{.2}N_{.8}$ (PDF-01-076-2484) that has a cubic structure with Fm-3m(225) space group and observed at 2θ= 36.6°(d=2.44797Å,(111)), 2θ=42.6°(d=2.12045Å,(200)), 2θ=61.7°(d=1.50021Å,(220)) , 2θ=74°(d=1.27988Å,(311)) and 2θ=77.9°(d=1.22550Å,(222)). This shift is attributed to the formation of highly substoichiometric phase.[25]

Likewise, a mixture of titanium nitride and carbonitride phases were obtained at 1573 K. $TiN_{.90}$ (PDF-01-071-0299) that has a cubic structure with Fm-3m(225) space group were detected at 2θ= 36.6°(d=2.45281Å,(111)), 2θ=42.6°(d=2.12045Å,(200)), 2θ=61.8°(d=1.49858Å,(220)) , 2θ=74.1°(d=1.27766Å,(311)) and 2θ=78°(d=1.22332Å,(222)). Similarly, $TiC_{.2}N_{.8}$ phase (PDF-01-076-2484) was identified with primary diffraction peaks detected at 2θ= 36.6°(d=2.44797Å,(111)), 2θ=42.6°(d=2.12045Å,(200)), 2θ=61.7°(d=1.50021Å,(220)) , 2θ=74°(d=1.27988Å,(311)) and 2θ=77.8°(d=1.22629Å,(222)). As the reaction temperature increases, peaks become sharper because of the increase in crystallite size and particle aggregation. The crystalline size obtained from Scherrer equation ranges from 12 to 39 nm (Table 1).

Generally, XRD patterns for the samples synthesized under a flow of nitrogen tend to shift to low angle with increasing reaction temperature. This is attributed to the expansion of the lattice parameters associated with incorporation of carbon in the inorganic phase. Further heating of titanium nitride phase caused an increase in lattice parameters which resulted in replacing some of the nitrogen atoms by carbon with a larger radius (solid state diffusional reaction of carbon into TiN) producing titanium carbonitride solid solution. The incorporation of carbon in the nitride to produce carbonitride phase enhanced further at high temperature (1573 K) which caused larger shift of XRD pattern to lower angle compared to those prepared at lower temperatures (1023 K and 1223 K).[26]

Elemental analyses were performed to determine the concentrations of carbon and nitrogen in the synthesized samples (Table 1). The sample synthesized at 1023 K shows comparable

amounts of carbon (18.6%) and nitrogen (20.9%) and nitrogen content found to be in agreement with the theoretical value of nitrogen (20.5%) in $(TiN)_{.88}$. This finding matches well with the results obtained from XRD confirming that the produced phase is $(TiN)_{.88}$. The high concentration of carbon in the sample suggests that it is present as an amorphous phase as revealed from TEM images discussed below.[27] It should be noted that it is expected that minor carbon contents get incorporated in the inorganic phase.

Further increase in reaction temperature to 1223 K shows a decrease in nitrogen content to 16.3% whereas carbon content increased to 24.6%. The nitrogen content was found to be close to the theoretical value of nitrogen (18.2%) in $TiC_{.2}N_{.8.}$ However, carbon concentration exceeded the theoretical carbon stoichiometry in the $TiC_{.2}N_{.8}$ (3.9%) suggesting the presence of excess amount of carbon in a separate phase.[28] Likewise, the elemental analysis data of the sample prepared at 1573 K found to be almost similar to those obtained at 1223 K. This finding was consistent with the values of carbon and nitrogen contents in titanium carbonitride reported in the literature.[12] These results were in agreement with XRD data which confirmed that nitride-carbide solid solution was produced at high temperature (>1023 K).

TEM was performed on the samples synthesized under a flow of nitrogen with a weight ratio of 1:1 C_3N_4/TiF_4 in a temperature range from 1023 to 1573 K. The TEM images and SAED patterns of the samples are shown in Fig.4. The sample synthesized at 1023 K shows the formation of small nanocrystals with a size of 5 nm in the matrix of the carbonaceous species reflecting the original pore size of the mpg-C_3N_4 template. The corresponding

SAED patterns revealed three diffraction rings with radii of 0.248, 0.217 and 0.15 nm, corresponding to the interatomic spacings of titanium nitride and carbonitride cubic structure crystal planes (111), (200), and (220), respectively. These results were consistent with XRD pattern and the high carbon concentrations detected by elemental analysis was formed as a result of the decomposition of the C_3N_4 template which was observed as an amorphous phase in the matrix and between the nanoparticles. The sample prepared at 1223 K exhibits small nanoparticles in the size of 10 nm. The SAED pattern shows three diffraction rings with radii of 0.244, 0.213, and 0.15 nm, corresponding to the interatomic spacings represented by titanium nitride and carbonitride cubic structures crystal planes (111), (200), and (220), respectively; these results were in agreement with the XRD patterns. The sample synthesized at 1573 K shows nanoparticles in the size of 15 nm, suggesting the aggregation of the nanoparticles. The corresponding SAED pattern revealed more diffraction rings indicating the increase in crystallinity with increasing reaction temperature with radii of 0.249, 0.216, and 0.15 nm, corresponding with the interatomic spacings of titanium nitride and carbonitride cubic structure crystal planes (111), (200), and (220), respectively. The nanocrystals were surrounded with graphitized carbon with d-spacing of 0.35 nm. The obtained d-spacing corresponds with interatomic spacings of graphitized carbon[29] suggesting complete crystallization of the amorphous carbon originated from C_3N_4 decomposition. It should be noted that amorphous or graphitized carbon play an important role in dispersing the nanoparticles, prevent sever aggregation and functions as conductive substrates which proved to be very effective in wide range of applications, in particular enhancing electrochemical performance.[18]

XPS measurements were performed to study the surface chemical composition and oxidation state. The Ti 2p, N 1s, C 1s and O 1s spectra are shown in Fig. 5 A, B, C and D respectively. The XPS spectrum of Ti 2p for the sample synthesized at 1023 K showed the presence of the main doublet lines at 458.4 eV for Ti $2p_{3/2}$ and 464.1 eV for Ti $2p_{1/2}$, which are characteristic of amorphous TiO_2.[30,31] This surface oxide layer was formed during the passivation process that occurred at the end of the synthetic procedure as well as when the sample was exposed to ambient air once it is removed from the furnace at room temperature. The observed shoulder at 454.5 eV for Ti $2p_{3/2}$ in addition to the binding energy of N 1s at 396.4 eV both confirms the formation of TiN.[32,33]

Ti 2p shows the presence of a small peak at 456.4 eV which is difficult to identify due to the overlap of the signals emitted from Ti $2p_{3/2}$ of TiO_2 and TiN. As a result, this binding energy was attributed to the intermediate phase of Ti-O-N.[34] This finding was further confirmed by the presence of the associated peak observed at 395.8 eV in the N 1s spectrum which corresponds to oxynitride.[34]

The major peak for N 1s was observed at 398.1 accompanied with a shoulder at 399.4 eV which was assigned to nitrogen bounded in pyridine-like structure and to sp^3 C respectively.[35,36] This finding confirms that this sample has CN_x residue originated from C_3N_4 decomposition as confirmed by TEM and elemental analysis.

Similarly, XPS spectrum of Ti 2p for the sample prepared at 1223 K shows the presence of Ti 2p doublet for TiO_2 with a shift of 0.4 eV to higher binding energy in comparison with doublet peaks observed for the sample prepared at a lower temperature.[37,38] This shift could be due to the transformation of amorphous oxide to crystalline phase.[31]

Doublet lines of Ti 2p assigned to TiN were prominent and shifted to higher binding energy at 455.2 eV for Ti $2p_{3/2}$ and 460.9 for Ti $2p_{1/2}$ eV.[30,39] In addition, N 1s spectrum shows a major peak at 397.1 eV confirming the presence of TiN.[30,39-41]

The binding energy of the Ti $2p_{3/2}$ detected at 456.8 eV and N 1s at 396.3 eV were attributed to oxynitride phase.[34]

Other peaks for N 1s at 398.7 eV and 400.4 eV were assigned to nitrogen bounded to sp^3 C and NH bonds respectively.[36] For the sample synthesized at 1573 K, Oxide phase observed at lower temperature was decreased in intensity and shifted to higher binding energy at 459.3 eV and 464.8 eV indicating complete crystallization of TiO_2.[30,42] Ti 2p peak detected at 455.4 eV was assigned to Ti bounded to carbon or and Ti bounded to nitrogen.[30,43] C 1s core level spectrum shows the presence of a characteristic peak of Ti-C at 282.2 eV besides the N 1s binding energy at 397.3 eV for Ti-N.[30,44] This finding confirms the formation of titanium carbonitride phase at high temperature. The XPS results for C 1s and N 1s obtained from the sample prepared at 1023 K are in close agreement with elemental analysis and TEM images which confirm that the sample has an excess amount of carbon and nitrogen residue that are not incorporated in the inorganic phase and essentially resulted from the decomposition of the C_3N_4 template. XPS spectra of O 1s indicate the presence of TiO_2 at the following binding energies 529.8 eV, 530.2 eV and 530.6 eV for the samples prepared at 1023 K 1223 K and 1573 K respectively. The intensity of O 1s signal attributed in majority to Ti-O bound decreases with increasing reaction temperature.[30,38]

N_2 sorption measurements were carried out to determine the BET surface area of the synthesized samples (Table 1).The highest surface area (187 m^2 g^{-1}) was observed for the sample prepared at 1223 K. The observed high surface area may arise from the presence of graphitized carbon.[28]

TGA analyses were performed under air up to 1273 K to study the decomposition of the materials and accordingly determine their thermal stability. While oxidation of the carbonaceous residue is expected to decrease the weight, oxidation of the nitride (TiN) species leads to increase in weight. The TGA results are shown in Fig.6 and the obtained curve of the sample synthesized at 1023 K shows a slight weigh loss arising from the evaporation of adsorbed water on the surface of the sample. A drastic weight loss occurred in the temperature range of approximately 710 K to 810 K, which was consistent with the oxidation of carbonaceous residue from C_3N_4 remaining in the sample. The sample prepared at 1223 K shows a slight increase in weight (1.6%) at 727 K which is most likely attributed to the primary oxidation of titanium nitride or carbonitride then the weight decreased until 840 K associated with the presence of a large amount of carbon as a separate phase compared to other samples. TGA curve for the sample synthesized at 1573 K where TiN and $TiC_{.2}N_{.8}$ are present as major phases shows a weight increase (7.8%) at ~826 K, indicating the oxidation of the material. In addition, no decrease in weight in the temperature range, 700-800 K, was observed in this sample which confirmed that the separate phase of carbon detected in the sample synthesized at lower temperatures decreased at 1573 K due to its involvement in the formation of the solid solution. The TGA

analysis was in direct agreement with the data obtained by other characterization methods (i.e., XRD, XPS, TEM and elemental analysis).

Generally, metal orthoesters were created by the dissolution of the chlorides in alcohol followed by removal of HCl and once it is mixed with mpg-C_3N_4 and heated to 1023 K under N_2, $(TiN)_{.88}$ was formed through carbo-thermal reduction nitridation process (CRN). When the temperature increased further to 1223 K, nano-$(TiN)_{.88}$ reacted with the carbon residue detected by elemental analysis and TEM images through carbo-thermal reduction process, leading to the formation of the nitride-carbide solid solution. At 1573 K, N-doped metal carbide is still present in the form of nitride-carbide solid solution which could be due to the nitrophilicity of titanium species even at at high temperature[12] which may suggest that gas flow functions as nitrogen source to enhance the formation of nitride phase and accordingly prevents carbo-thermal reduction process required to produce pure phase of carbide.[45,46]

Group V (V, Nb, Ta)

Vanadium nitride and carbonitride nanoparticles

The samples were synthesized under nitrogen flow at different temperatures from 1023 to 1573 K while keeping the ratio of mpg-C_3N_4/ VCl_3 at constant 1:1. The produced nanoparticles were characterized by XRD to determine the crystallite structure as shown in Fig.7. Scherrer equation was applied to obtain the crystallite size and listed in Table 1. The XRD pattern for the sample synthesized at 1023 K shows broad peaks which attributed

to the formation of an amorphous phase or small particle size. The peaks were detected at 2θ= 37.5°(d=2.39604Å,(111)), 2θ=43.7°(d=2.06851Å,(200)), 2θ=63.4°(d=1.46513Å,(220)) and 2θ=76.1°(d=1.24892Å,(311)) which correspond to cubic structure of VN (PDF-00-035-0768) with Fm-3m(225) space group. Further increase of temperature to 1223 K, peaks became sharper and observed at 2θ= 37.5°(d=2.39143Å,(111)), 2θ=43.7°(d=2.06851Å,(200)), 2θ=63.4°(d=1.46513Å,(220)) and 2θ=76.1°(d=1.24868Å,(311)). The peaks were consistent with VN (PDF-00-035-0768) that has a cubic structure with Fm-3m (225) space group. Similarly, XRD pattern of the sample synthesized at 1573 K shows four major peaks detected at 2θ= 37.6°(d=2.38779Å,(111)), 2θ=43.7°(d=2.06881Å,(200)), 2θ=63.5°(d=1.46328Å,(220)) and 2θ=72°(d=1.24764Å,(311)) which correspond to VN (PDF-00-035-0768) that has a cubic structure with Fm-3m (225) space group. It should be noted that XRD peaks are shifted to the lower angel by 0.1° with respect to the expected position of the pure phase of VN. This shift is associated with the presence of other phase observed in the shoulders and the phase was detected at 37.6°(d=2.38902Å,(111)), 2θ=43.7°(d=2.06858Å,(200)), 2θ=63.5°(d=1.46226Å,(220)) and 2θ=76.3°(d=1.24679Å,(311)) which found to be consistent with the cubic crystalline structure of V_2CN (PDF-01-076-6064) with Fm-3m (225) space group.

As the synthesis temperature increases, the crystalline size increases from 14 to 48 nm as shown in Table 1.

The elemental analyses result determined the concentrations of carbon and nitrogen in the synthesized samples which are shown in Table 1. The concentration of nitrogen decreased from 9.6 % to 6 % with increasing reaction temperature. While carbon content increased from 6 % to 13.4 %. The increase in carbon contents suggests the incorporation of carbon residue originated from C_3N_4 decomposition in the inorganic phase to produce carbonitride solid solution at 1573 K. This finding is consistent with XRD data.

TEM was performed on the samples synthesized under a flow of nitrogen with a weight ratio of 1:1 C_3N_4/VCl_3 in a temperature range from 1023 to 1573 K. The TEM images and SAED patterns of the samples are shown in Fig.8 The sample synthesized at 1023 K shows the formation of small nanoparticles with a size of 3 nm to 5 nm in the matrix of the carbonaceous species. The corresponding SAED patterns revealed a weak ring of spots which is due to the lack of crystallinity or presence of ultrafine nanoparticles which is consistent with XRD pattern. The excess carbon concentrations detected by elemental analysis was formed as a result of the decomposition of the C_3N_4 template which was observed as an amorphous phase in the matrix and between the nanoparticles. The TEM images of the sample prepared at 1223 K exhibits small nanoparticles in the size range of 5-10 nm. Similarly, the sample synthesized at 1573 K shows irregular shaped nanoparticles in the size of 25 to 50 nm, suggesting the aggregation of the nanoparticles. The corresponding SAED pattern revealed more diffraction rings indicating the increase in crystallinity and particle size with increasing reaction temperature with radii of 0.203, 0.149, and 0.129 nm, corresponding with the interatomic spacings of vanadium nitride ,

carbide and carbonitride cubic structure crystal planes (200), (220), and (311), respectively.

The high contents of carbon and nitrogen detected by elemental analysis were observed in the matrix and between the nanoparticles and they were originated from the decomposition of the C_3N_4 template. Graphitized carbon was surrounded the obtained nanoparticles which suggests that amorphous phase of carbon residue that primarily originated from C_3N_4 decomposition at lower temperature transformed to crystalline phase at high temperature.

XPS measurements were performed to study the surface chemical composition and oxidation state of the metal. The V 2p, N 1s, C 1s and O 1s spectra are shown in Fig.9 respectively. The XPS spectra of V 2p core level for the sample synthesized at 1023 K shows the presence of two dominant peaks at the following binding energies: 517.0 eV for V $2p_{3/2}$ and 524.6 eV for V $2p_{1/2}$ which were assigned to V^{5+} in V_2O_5.[47-49] This surface oxide layer was formed during the passivation process that occurred at the end of the synthetic procedure as well as when the sample was exposed to ambient air once it is removed from the furnace at room temperature.[28] Additional doublet at 516.0 eV and 523.6 eV for V $2p_{3/2}$ and V $2p_{1/2}$ respectively was observed and found to be close to the reported value of V 2p for VO_2 phase.[50]

The N 1s core level spectrum indicates the presence of a peak at 401.2 eV which corresponds to nitrogen bonded to sp^2 carbon and small shoulder was observed at 399.6 eV found to be consistent with nitrogen bonded to sp^3 carbon.[36,51] C 1s tail observed in the range of 285-287 was assigned to C-N species originated from the decomposition of the C_3N_4 template.[52] The XPS results for C 1s and N 1s are in close agreement with elemental

analysis and TEM images confirming that the sample prepared at 1023 K has an excess amount of carbon and nitrogen residue that are not incorporated in the inorganic phase. Similarly, the XPS spectrum of V 2p core level for the sample synthesized at 1223 K shows two doublet lines, first V 2p doublet at 517.1 eV for V $2p_{3/2}$ and 524.5 eV for V $2p_{1/2}$ corresponds to V^{5+} in V_2O_5.[47-49]

The second V 2p doublet detected at 516.0 eV and 523.6 eV was attributed to VO_2.[50] A small signal appears around 513.4 eV corresponding to V $2p_{3/2}$ component of V 2p from VN.[53]

XPS spectrum of N 1s confirms the presence carbon residue by detecting a major peak at 401.2 eV corresponding to nitrogen bonded to sp^2 carbon and small shoulder observed at 399.5 eV assigned to nitrogen bonded to sp^3 carbon.[36,51] Also, a new signal was observed at 396.9 eV which well agrees with the characteristic value of N1s of VN.[54] C 1s shows a shift of the main peak to lower binding energy (284.4 eV) which is ascribed to sp^2 bonded carbon (graphite)[28,55] which is in agreement with TEM images. The tail observed in the range of 285-287 was assigned to C-N species originated from the decomposition of the C_3N_4 template.[52] The C 1s signal detected at 288.5 eV corresponds to C=O.[55] N 1s spectrum indicates the formation of VN and C1s show no characteristic peak for carbide which is consistent with XRD pattern suggesting that the produced phase at this temperature is VN. For the sample synthesized at 1573 K, the intensity of V 2p doublet lines for oxide phase observed at lower temperatures decreased while a second doublet at 513.3 eV and 520.9 eV for V$2p_{1/2}$ and V$2p_{3/2}$ respectively became prominent and attributed to vanadium bounded to carbon or/and to nitrogen.[47-49,53] XPS spectrum of N 1s indicates

the presence of a major signal at 397.3 eV which ascribed to N 1s of V-N.[54] There is a drastic decrease in intensity of the signal observed at 401.2 eV which indicates that the carbon and nitrogen residue detected by elemental analysis and observed in TEM images at lower temperature was used up at this temperature and contributed in the formation of the expected product. C 1s shows a rapid increase in the intensity of the signal observed at 284.4 eV which suggests that graphitization process enhanced at high temperature.[52] Also, the C 1s shows the appearance of a new signal at 282.5 eV which is consistent with the reported value of C 1s for vanadium bounded to carbon in V-C.[56] XPS spectra of V 2p, N 1s and C 1s confirmed that vanadium is bounded to both N and C forming carbonitride solid solution which is in agreement with XRD pattern.

The XPS spectrum of O 1s for all samples contained a characteristic signal at 530 eV that corresponds to O^{2-} in V_2O_5 and the intensity of this signal decreased at high temperature (1573 K).[49]

N_2 sorption measurements were performed to obtain the BET surface area of the synthesized samples. Table 1 shows that the surface area of the products decreased with increasing reaction temperature. This is attributed to the fact that at high temperature particles tend to aggregate producing larger size which is consistent with the trend observed in the crystalline size obtained by Scherrer equation from XRD patterns. Sample synthesized at 1023 K exhibited the highest surface area (171 $m^2 g^{-1}$) among the samples prepared in this study.

TGA analyses under air up to 1273 K were carried out for the produced nanoparticles as shown in Fig.10. TGA curves for the samples prepared at 1023 and 1223 K exhibit small weight decrease until 430 K suggesting evaporation of the adsorbed moisture on the surface. Then, an obvious weight loss was observed in the temperature range 500-726 K for the both samples and the weight decrease was higher in the case of the sample synthesized at 1023 K associated with the oxidation of larger amount of separate phase of carbon. Similarly, the TGA curve for the sample prepared at 1573 K displays a small weight loss from 560 to 690 K followed by a rapid weight increase (20%) suggesting a complete oxidation of the present phases (VN and V_2CN). Notably, the TGA analyses found to be consistent with the other characterization methods (XRD, XPS, TEM and elemental analysis).

Generally, dissolution of VCl_3 in ethanol resulted in metal orthoesters and subsequent removal of HCl and after mixing with mpg-C_3N_4 and heated to 1023 and 1223 K, VN phase was formed through carbothermal reduction nitridation process (CRN). When the reaction temperature increased to 1573 K, carbothermal reduction process of VN occurred and nitride-carbide solid solution (V_2CN) was produced by solid state diffusional reaction of VN with carbon residue originated from C_3N_4 decomposition at lower temperature detected by elemental analysis and observed in TEM image. These findings suggest that due to the high nitrophilicity of vanadium, the pure phase of carbide can not be produced even at high temperature and a mixture of nitride and carbonitride solid solution are formed instead.

Niobium nitride, carbonitride and carbide nanoparticles

The samples were synthesized under nitrogen flow at different temperatures from 1023 to 1573 K while keeping the ratio of mpg-C_3N_4/ $NbCl_5$ at constant 1:1. The produced nanoparticles were characterized by XRD to determine the crystallite structure as shown in Fig.11. Scherrer equation was applied to obtain the crystallite size and listed in Table 1. The XRD pattern for the sample synthesized at 1023 K shows a broad diffraction peak which attributed to the formation of amorphous phase or small particle size. Most likely, the broad peaks correspond to NbN (PDF-01-0773560) that has a cubic structure with Fm-3m (225) space group. Further increase of temperature to 1223 K, peaks became sharper and observed at 2θ= 35°(d=2.55935Å,(111)), 2θ=40.6°(d=2.21798Å,(200)), 2θ=58.8°(d=1.56713Å,(220)) , 2θ=70.4°(d=1.33507Å,(311)) and 2θ=74°(d=1.27857Å,(222)). The peaks were consistent with the formation of $NbC_{.6}$ (PDF-03-065-9878) that has a cubic structure with Fm-3m (225) space group. Also, the XRD peaks are shifted to a higher angel by 0.15° as compared to the expected position of pure phase of Nb_2CN (PDF-01-071-6041) that has a cubic structure with Fm-3m (225) space group and detected at 2θ= 34.9°(d=2.56394Å,(111)), 2θ=40.5°(d=2.22286Å,(200)), 2θ=58.7°(d=1.56974Å,(220)) , 2θ=70.2°(d=1.33946Å,(311)) and 2θ=73.8°(d=1.28184Å,(222)).

XRD pattern of the sample synthesized at 1573 K shows five major peaks which assigned to $NbC_{.87}$ and/or NbC. $NbC_{.87}$ (PDF-01-089-4306) that has a cubic structure with Fm-3m (225) space group were detected at 2θ= 34.8°(d=2.57465Å,(111)), 2θ=40.3°(d=2.23242Å,(200)), 2θ=58.4°(d=1.57722Å,(220)) , 2θ=69.8°(d=1.34498Å,(311)) and 2θ=73.4°(d=1.28794Å,(222)). Whereas NbC (PDF-00-

010-0181) that has a cubic structure with Fm-3m (225) space group were observed at 2θ= 34.7°(d=2.57964Å,(111)), 2θ=40.3°(d=2.23094Å,(200)), 2θ=58.3°(d=1.58112Å,(220)) , 2θ=69.7°(d=1.34797Å,(311)) and 2θ=73.2°(d=1.29066Å,(222)).

XRD pattern of niobium nitride produced at 1023 K was shifted to low angle with increasing reaction temperature. This is due to the increase in lattice parameters which resulted in replacing some of the nitrogen atoms by carbon that has a larger radius (solid state diffusional reaction in NbN + C system) producing niobium carbonitride phase. The shift was prominent in the XRD pattern of the sample prepared at 1573 K associated with complete replacing of nitrogen in niobium carbonitride by carbon to produce niobium carbide phase.

As the synthesis temperature increases, the crystalline size increases from 6 to 36 nm as shown in Table 1.

The elemental analyses results determined the concentrations of carbon and nitrogen in the synthesized samples as shown in (Table 1). Overall, the concentration of carbon increased with increasing reaction temperature. While nitrogen content decreased until reached a value close to zero (~0.8) and this is in agreement with phases obtained by XRD suggesting that as the reaction temperature increased, the carbothermal reduction process reinforced towards formation of carbide phase rather than nitride. Sample synthesized at 1023 K shows comparable amounts of carbon and nitrogen which indicates that sample has C and N species not incorporated in the inorganic phase and observed in the matrix as will be confirmed later by TEM images. The sample synthesized at 1223 K indicates the presence

of 4.5% of nitrogen which is below the theoretical value of nitrogen (6.6%) in Nb_2CN. The reduction of nitrogen concentration indicates that the carbothermal reduction process started to take place and the small amount of nitrogen may incorporate in the inorganic phase forming N-doped metal carbide. Whereas carbon concentration (10%) found to exceed the stoichiometric value for Nb_2CN (5.6%) and is in a close agreement with the theoretical value of carbon (11.4% and 10% for NbC and $NbC_{.87}$ respectively) suggesting the formation of niobium carbide phase. The sample synthesized at 1573 K shows a drastic reduction of nitrogen content to 0.8%. The carbon concentration increased to 14% which is above the stoichiometric value for niobium carbide 10% and 11% for NbC and $NbC_{.87}$ respectively. These findings were consistent with XRD patterns.

TEM was performed on the samples synthesized under a flow of nitrogen with a weight ratio of 1:1 $C_3N_4/NbCl_5$ in a temperature range from 1023 to 1573 K. The TEM images and SAED patterns of the samples are shown in Fig.12. The TEM image of the sample synthesized at 1023 K exhibits small nanoparticles with a size of 3 nm in the matrix of the carbonaceous species. The corresponding SAED patterns show weak ring of spots which could be due to the lack of crystallinity or presence of ultrafine nanoparticles which is consistent with XRD pattern.

The TEM images of the sample prepared at 1223 K formed small nanoparticles in the size of 10 nm. The SAED pattern shows more diffraction rings with radii of 0.261, 0.227, and 0.159 nm, corresponding to the interatomic spacings of niobium carbonitride and carbide cubic structures crystal planes (111), (200), and (220), respectively; these results were in

agreement with the XRD patterns. The sample synthesized at 1573 K shows larger particles in the size of 15 to 20 nm, suggesting the aggregation of the nanoparticles. The corresponding SAED patterns revealed more diffraction rings indicating the increase in crystallinity and particle size with increasing reaction temperature with radii of 0.262, 0.227, and 0.161 nm, corresponding with the interatomic spacings of niobium carbide cubic structure crystal planes (111), (200), and (220), respectively. Graphitized carbon that surrounded the obtained nanoparticles was observed which indicates the complete crystallization of the observed amorphous phase of carbon residue that primarily originated from C_3N_4 decomposition at the lower temperature.

XPS measurements were performed to study the surface chemical composition and oxidation state of the metal. The Nb 3d, N 1s, C 1s and O 1s spectra are shown in Fig.13 respectively. The XPS spectrum of the core level Nb 3d for the sample synthesized at 1023 K shows the presence of three distinctive peaks at the following binding energies: 204.2 eV, 207.6 eV, and 210.4 eV.

The doublet lines at 207.6 eV for Nb $3d_{5/2}$ and 210.4 eV for Nb $3d_{3/2}$ were assigned to Nb^{5+} in Nb_2O_5.[57,58] Due to the passivation process conducted at the end of the synthetic procedure in addition to the exposure of the sample to ambient air, oxide surface was formed on the sample.[28] The peak at 204.2 eV corresponds to Nb $3d_{5/2}$ component for NbN phase.[59] The formation of nitride phase was further confirmed by detecting a characteristic peak at 397.3 eV observed in the N 1s core level spectrum related to NbN.[60] Additional peak was observed in the N 1s spectrum at 400.2 eV attributed to C-N bond.[36]

The Nb 3d core level spectrum of the sample synthesized at 1223 K reveals the presence of three peaks at 204.0 eV, 207.6 eV and 210.4 eV. The binding energies at 207.6 eV and 210.4 eV correspond to the Nb 3d doublet for Nb_2O_5.[57,58] The peak detected at 204.0 eV was assigned to Nb $3d_{5/2}$ component for Nb bounded to nitrogen and/or carbon.[61] N1s peak was observed at 400.5 eV ascribed to bridging nitrogen atoms $(C)_3–N$[62]. The peak at 397.3 eV observed in the N 1s spectrum was attributed to nitrogen bounded to niobium in NbN phase that already observed for the sample prepared at lower temperature confirming the presence of Nb-N bound. Furthermore, Nb bound to C was confirmed by examining C 1s spectrum which shows the appearance of a new peak at 282.7 eV characteristic for the carbidic bond. These findings suggest that Nb_2CN is formed at this temperature as confirmed by XRD.[58,63] These finding suggests that the produced phase is Nb_2CN, which is in close agreement with XRD pattern.

The sample synthesized at 1573 K shows a drastic decrease of the intensity for oxide phase. The doublet lines at 204.0 eV and 206.8 ascribed to Nb-N and/or Nb-C bounds became prominent.[60,61] Distinguishing between the two bounds can be achieved by investigating the XPS spectra of N 1s and C 1s. The results indicate that the intensity of N 1s signal observed at 397.3 eV ascribed to Nb-N in nitride phase was decreased while C 1s signal characteristic for carbidic bound (282.7) increased confirming that the produced phase at this temperature is NbC.[58,63] Further analysis of C1s spectrum reveals a shift of the main peak to lower binding energy (284.6 eV) confirming graphitization of amorphous carbon which is in agreement with TEM images.[64]

The XPS spectrum of O 1s for all samples show a characteristic peak at 530.8 eV that is

assigned to O^{2-} in Nb_2O_5 and the intensity of this signal decreased with increasing reaction temperature.[57]

N_2 sorption measurements were performed to obtain the BET surface area of the synthesized samples. The results are also listed in Table 1 which showed that the surface area of the products decreased with increasing reaction temperature from 157 to 90 $m^2 g^{-1}$. This is attributed to the fact that at high temperature particles tend to aggregate producing larger size which is consistent with the trend observed in the crystallite size obtained by Scherrer equation from XRD pattern. Sample synthesized at 1023 K exhibited the highest surface area (157 $m^2 g^{-1}$) among the samples prepared in this study.

The thermal stability of the produced nanoparticles was investigated in the air up to 1273 K as shown in Fig.14. TGA curve of the sample prepared at 1023 K shows a gradual decrease in weight which continued until 860 K. This weight loss is attributed to the evolution of carbon oxide resulted from the oxidation of carbon residue present as a separate phase in the sample. High temperature synthesis where niobium carbide is formed led to a weight gain attributed to the oxidation of the material. The onset oxidation for the sample prepared at 1223 K (480 K) was found to be lower than that of the sample synthesized at the higher temperature. This difference could be due to the fact that sample synthesized at 1223 K has a smaller particle size which accordingly possesses higher surface energy and can be oxidized by air at lower temperature in comparison with that prepared at 1573 K.[65] However, the observed weight gain was higher for the sample

synthesized at 1573 K, which is consistent with the oxidation of the pure phase of niobium carbide. The data obtained by TGA analyses was in close agreement with XRD, XPS, TEM and elemental analyses.

Overall, the sample synthesized at 1023 K formed NbN through carbothermal reduction nitridation process (CRN) of the mixture of metal orthoester with the C_3N_4 template. When the reaction temperature increased further to 1223 K, carbothermal reduction process took place through solid state diffusional reaction of carbon into NbN phase to produce a mixture of Nb_2CN and $NbC_{.6}$. At 1573 K carbothermal reduction process of Nb_2CN enhanced further and nitrogen atoms in Nb_2CN phase were replaced by the carbon to produce pure phase of $NbC_{.87}$ or/and NbC.

Tantalum nitride, carbonitride and carbide nanoparticles

XRD analysis was performed to determine the crystal structure of the samples synthesized under the nitrogen flow at different temperatures from 1023 to 1573 K while keeping the ratio of mpg-C_3N_4/$TaCl_5$ at constant 1:1 (Fig.15). Crystallite sizes obtained using the Scherrer equation are listed in Table 1. The XRD pattern for the sample synthesized at 1023 K shows broad diffraction peaks, which can be interpreted as either an ultrafine particle or an amorphous phase. The XRD pattern corresponds to TaN (PDF-03-065-9404) that has a cubic structure with Fm-3m (225) space group. The XRD pattern for the sample synthesized at 1223 K matches well with tantalum carbonitride (Ta_2CN: PDF 03-065-8774), with a cubic structure with a Fm-3m (225) space group, and/or with defective tantalum carbide (C_3Ta_4 PDF 03-065-3191 and $Ta_4C_{3.04}$ PDF 01-089-2121), with a cubic

structure with a pm-3m (221) space group, thus making it difficult to unambiguously assign a specific phase. At higher temperature 1573 K, XRD pattern shows the formation of a tantalum carbide phase TaC (PDF 00-002-1023) that has a cubic structure with a Fm-3m (225) space group. TEM was also performed on the samples with sizes of 3 and 15 nm for the samples synthesized at 1023 and 1573 respectively (Fig.16). (Further study on the synthesis, characterization and electrocatalytic activities of the tantalum based samples are discussed in details in chapter 3).

Group VI (Cr, Mo, W)

Chromium nitride and carbide nanoparticles

The samples were synthesized under nitrogen flow at different temperatures from 1023 to 1573 K while keeping the ratio of mpg-C_3N_4/ $CrCl_2$ at constant 1:1. The produced nanoparticles were characterized by XRD to determine the crystallite structure as shown in Fig. 17. Scherrer equation was applied to obtain the crystallite size and listed in Table 1. The XRD pattern for the sample synthesized at 1023 K shows four major diffraction peaks observed at 2θ= 37.5°(d=2.39199Å,(111)), 2θ=43.6°(d=2.06976Å,(200)), 2θ=63.4°(d=1.46471Å,(220)) and 2θ=76.1°(d=1.24877Å,(311)) which correspond to CrN (PDF-00-011-0065) that has cubic structure with Fm-3m (225) space group.

Similarly, when the temperature increased further to 1223 K, XRD pattern shows the presence of cubic structure of CrN (PDF-00-011-0065) with Fm-3m(225) space group detected at 2θ= 37.4°(d=2.40143Å,(111)), 2θ=43.7°(d=2.06632Å,(200)),

2θ=63.5°(d=1.46313Å,(220)) and 2θ=76.1°(d=1.24877Å,(311)) space group. XRD pattern of the sample synthesized at 1573 K was well matched the formation of Cr_3C_2 (PDF-00-035--0804) that has orthorhombic with pbnm (62) space group.

As the synthesis temperature increases, the crystalline size increases from 24 to 34 nm as shown in Table 1.

The elemental analyses results determined the concentrations of carbon and nitrogen in the synthesized samples are shown in Table 1. Overall, the concentration of carbon increased with increasing reaction temperature. While nitrogen content decreased until reached a value close to zero (~0.5).Samples synthesized at 1023 and 1223 K show a comparable amount of carbon and nitrogen which indicates the presence of carbon nitride residue. However, the sample prepared at 1573 K shows a drastic decrease in nitrogen content to 0.5 % and carbon content (17 %) was higher than the theoretical value of carbon (13 %) in Cr_3C_2.

Confirming the presence of excess amount of carbon. This result is in agreement with phases obtained by XRD suggesting that as the reaction temperature increased, the carbothermal reduction process enhanced towards the formation of pure carbide phase at 1573 K.

TEM was performed on the samples synthesized under a flow of nitrogen with a weight ratio of 1:1 $C_3N_4/CrCl_2$ in a temperature range from 1023 to 1573 K. The TEM images and SAED patterns of the samples are shown in Fig.18. The TEM image of the sample

synthesized at 1023 K exhibits small nanoparticles with a size of 5 nm in the matrix of the carbonaceous species. The corresponding SAED patterns revealed three diffraction rings with radii of 0.245, 0.209, and 0.15 nm, corresponding to the interatomic spacings of CrN cubic structure crystal planes (111), (200), and (220), respectively. The TEM images of the sample prepared at 1223 K formed nanoparticles in the size range of 20 to 25 nm. The SAED pattern shows more diffraction rings confirming the increase in crystallinity; these results were in agreement with the XRD patterns. The sample synthesized at 1573 K shows large particles, suggesting sever aggregation of the nanoparticles. The corresponding SAED pattern revealed more diffraction rings indicating the increase in crystallinity and particle size with increasing temperature. Graphitized carbon was observed for the samples prepared at high temperatures.

XPS measurements were performed to study the surface chemical composition and oxidation state of the metal. The Cr 2p, N 1s, C 1s and O 1s spectra are shown in Fig.19 respectively. The analysis of the Cr 2p is difficult due to the multiple splitting effects.[66] The XPS spectrum of Cr 2p core level for the sample synthesized at 1023 K shows a doublet line at 575.6 eV for Cr $2p_{3/2}$ and 585.3 eV for Cr $2p_{1/2}$ corresponding to Cr^{3+} from Cr_2O_3.[67,68] A shoulder observed at 574.4 eV for Cr $2p_{3/2}$ was assigned to Cr^{3+} from CrN. The nitride phase was further verified by detecting the characteristic peak at 396.4 eV.[67,69] The N 1s core level spectrum shows also a broad structure in the binding energy range (398.0 to 402.0 eV) corresponding to varies states of nitrogen most likely originated from CNx residues.[36] Similarly, the sample synthesized at 1223 K shows the presence of a doublet

line 575.6 eV for Cr $2p_{3/2}$ and 585.3 eV for Cr $2p_{1/2}$ corresponding to Cr^{3+} from Cr_2O_3.[68,70] The shoulder peak at 574.5 for Cr $2p_{3/2}$ in addition to characteristic peak at 396.4 eV found to well match the chromium nitride phase.[67,69,71] Also, the N 1s spectrum shows a decrease of the characteristic peak of CNx residue observed at the lower temperature.[36]

Sample synthesized at 1573 K shows a doublet lines at 574.4 eV for Cr $2p_{3/2}$ and 583.7 eV for Cr $2p_{1/2}$ corresponding to chromium carbide.[71] The carbide phase was further confirmed by detecting a characteristic peak at 282.8 eV.[72]

The intensity of chromium oxide observed in Cr 2p core level spectrum decreased. N 1s core level spectrum shows no peaks attributed to nitride and CNx residue confirming the presence of a pure phase of chromium carbide.

Molybdenum carbide nanoparticles

XRD patterns for the samples synthesized under nitrogen flow at different temperatures from 1023 to 1573 K while keeping the ratio of mpg-C_3N_4/$MoCl_5$ at constant 1:1 are shown in Fig.20. Crystallite sizes obtained using the Scherrer equation is listed in Table 1. The XRD pattern for the sample synthesized at 1023 K shows broad diffraction peaks, which can be interpreted as either an ultrafine particle or an amorphous phase. The XRD patterns for the samples synthesized at 1023, 1223 K and 1573 K , show eight major peaks at 2θ=34.4°, 38°, 39,4°, 52.2°, 61.7°, 69.5°, 74.5° and 75.3° which are indexed as (100), (002), (101), (102), (110), (103), (112) planes of hexagonal Mo_2C (PDF-00-001-1188) or (PDF-00-035-0787).

TEM was performed on the samples with sized of 3 and 15 nm for the samples synthesized at 1023 and 1573 K respectively (Fig.21). (Further study on the synthesis, characterization and electrocatalytic activities of the molybdenum based samples are discussed in details in chapter 4).

Tungsten carbide nanoparticles

The XRD pattern (Fig. 22) for the sample shows broad diffraction peaks that correspond to W_2C (PDF-01-079-0743), which has a hexagonal structure with the p-31 m (162) space group. In addition, broad peaks ascribable to WC(N) phase was also observed, with small shoulder peak of metallic phase for W, which confirms that the reductive process happens during this synthesis in the case of W.[24]

The elemental analysis indicated the presence of a trace amount of nitrogen (0.3%). The carbon content is 3.5%, which agrees well with the theoretical value of carbon in the W_2C phase (3.16%) (Table 1).

The TEM image and SAED pattern are shown in Fig. 23. The sample has very fine 5 nm spherical particles, apparently due to the confinement effects of such small spacings on the template.

The W 4f, C 1s, N 1s and O 1s XPS spectra are shown in Fig. 24. The XPS spectrum of the W 4f core level shows characteristic peaks at 38.1 and 35.9 eV which were assigned to W $4f_{7/2}$ and W $4f_{5/2}$ doublet for tungsten oxide.[73-75] A doublet line was detected at binding

energy 31.8 eV for W $4f_{7/2}$ and 34.0 eV for W $4f_{5/2}$ characteristic for tungsten carbide. This assignment was further confirmed by the presence of a peak at 283.2 eV in the C 1s spectrum corresponding to tungsten carbide.[76,77] N 1s shows the presence of characteristic peak at 397.1-397.4 eV which corresponds to of WN.[78]

The N_2 sorption measurement yielded a BET surface area of 17.5 m^2 g^{-1} for the synthesized sample (Table 1).

Discussion regarding transition metal nitride and carbide nanoparticles syntheses

Different phases of transition metal nitride and carbide nanoparticles are produced through the reaction of the metal precursor with the mpg-C_3N_4 template which acts as confinement for particle growth and as a source of carbon and nitrogen. The reaction was conducted at different temperatures in the range of 1023 to 1573 K under nitrogen flow while keeping the weight ratio of C_3N_4 to the metal precursor constant at 1:1.

The expected reaction pathway may include the following steps; first, metal orthoester was created by the dissolution of the metal chloride in alcohol followed by the removal of HCl. Then a drop impregnation method of the solution was applied on the mpg-C_3N_4 template and at room temperature, there is no reaction and M-C or M-N is impossible to form accordingly. When the mixture is heated to 960 K, the reactive template C_3N_4 decomposed to active carbon and nitrogen species as shown in MS Fig. 2.The active carbon and nitrogen fragments will bond the oxygen atoms, reduce the metal center and produce corresponding

nitride or carbide through either carbothermal reduction nitridation or carbothermal reduction followed by a carburizing process.

In general, carbon or nitrogen active species compete in binding the transition metal atoms. As a result transition metal nitride or carbide are formed based on the reactivity of transition metals towards carbon and nitrogen fragments.

The research study shows that Ti, V, Nb, Ta and Cr reacted with nitrogen active species originated from the decomposition of the template at 1023 K under a flow of N_2 while keeping the weight ratio of reactants constant at unity to produce face centered cube of nitride phase (Fig. 25). Further increase in temperature ≥1223 K drives the nitride to react with the remaining carbon residue generated from the decomposition of the template to produce carbonitride and carbide phases as confirmed from XRD, XPS, elemental analysis and TEM. Carbide phase with hexagonal structure was observed in group VI (Mo and W) (Fig. 25).

The observed trend for the samples synthesized at 1023 K was found to depend on the electronic structure of d-band of the transition metals. Carbon and nitrogen donate one and two electrons respectively to *d* band of the transition metal which was split into bonding and antibonding portion. Due to the decreased d-band filling of group IV transition metals, they tend to receive more electrons which are associated with the binding to an interstitial atom that provides high ratio of electrons to the metal. As a result, the most stable IV nitride phase is produced associated with half-filled d-shell. On the other hand, group VI transition metals with increased d-band filling produced carbide phase rather than nitride with an attempt to avoid occupation of the antibonding level of the transition metals.[45]

The above trend was also correlated with the free energy of formation of transition metal carbide and nitride which indicates that the free energy of formation of nitride is lower for transition metal of group IV and VI whereas carbide phase is thermodynamically more favorable for group VI in particular for W and Mo (Table 2). In addition, the thermal stability of the produced nitride phases decreases at high temperature because of the evolution of nitrogen gas.[79,80]

This study shows the successful formation of transition metal carbide and nitride nanoparticles with a size of 3 nm in a matrix of the carbonaceous species and with increasing reaction temperature, the amorphous carbon seems to decrease or disappear due to its involvement in the formation of carbide phase and also it is converted to graphitized carbon surrounded the nanoparticles. It should be noted that amorphous or graphitized carbon plays an important role in dispersing the nanoparticles, prevents sever aggregation and functions as conductive substrates which proved to be very effective in wide range of applications, in particular enhancing electrochemical performance.

Conclusions

This study introduced a new procedure to synthesize a whole class of interstitial nitride, carbonitride and carbide nanoparticles with a size as small as 3 nm through the reaction of a metal precursor with the mpg-C_3N_4 template in the temperature range of 1023-1573 K under nitrogen flow while marinating a constant weight ratio of precursor to the template 1:1. The characterization results for the samples prepared at 1023 K proved a trend in the formation of nitride and carbide phases which primarily depends on the properties and electronic structure of the transition metals. The study shows that nitride phase was produced through the reaction of Ti, V, Nb, Ta and Cr with carbon nitride at 1023 K. Whereas, Mo and W have the tendency to produce carbide rather than nitride. The experimental results found to be in agreements with the thermodynamics of interstitial nitride and carbide formation. The applied synthetic procedure provides a control over size and shape of the produced nanoparticles which can be achieved by adjusting the size and shape of the original silica used to prepare the reactive template. Thus, this method offers chances to prepare the desired size, shape and phase of transition metal carbide and nitride suitable for a specific reaction which is undoubtedly the optimum objectives in materials chemistry.

References

(1) Giordano, C.; Antonietti, M. *NANO TODAY* **2011**, *6*, 366.

(2) Chen, J. G. *Chem. Rev.* **1996**, *96*, 1477.

(3) Ham, D.; Lee, J. *Energies* **2009**, *2*, 873.

(4) Claridge, J. B.; York, A. P. E.; Brungs, A. J.; Green, M. L. H. *Chem. Mater.* **1999**, *12*, 132.

(5) Chen, W.-F.; Muckerman, J. T.; Fujita, E. *Chem. Commun.***2013**, *49*, 8896.

(6) Chen, W. F.; Wang, C. H.; Sasaki, K.; Marinkovic, N.; Xu, W.; Muckerman, J. T.; Zhu, Y.; Adzic, R. R. *Energy Environ Sci* **2013**, *6*, 943.

(7) Li, P. G.; Lei, M.; Sun, Z. B.; Cao, L. Z.; Guo, Y. F.; Guo, X.; Tang, W. H. *J. Alloys Compd.* **2007**, *430*, 237.

(8) Zhu, Y.; Li, Q.; Mei, T.; Qian, Y. *J. Mater. Chem.* **2011**, *21*, 13756.

(9) Hanif, A.; Xiao, T.; York, A. P. E.; Sloan, J.; Green, M. L. H. *Chem. Mater.* **2002**, *14*, 1009.

(10) Bondarenko, V. P.; Pavlotskaya, É. G. *Powder Metall. Met. Ceram.* **1996**, *34*, 508.

(11) Giordano, C.; Erpen, C.; Yao, W.; Antonietti, M. *Nano Lett.* **2008**, *8*, 4659.

(12) Giordano, C.; Erpen, C.; Yao, W.; Milke, B.; Antonietti, M. *Chem. Mater.* **2009**, *21*, 5136.

(13) Yao, W.; Makowski, P.; Giordano, C.; Goettmann, F. *Chem. Eur. J* **2009**, *15*, 11999.

(14) Fischer, A.; Antonietti, M.; Thomas, A. *Adv. Mater.* **2007**, *19*, 264.

(15) Fukasawa, Y.; Takanabe, K.; Shimojima, A.; Antonietti, M.; Domen, K.; Okubo, T. *Chem Asian J* **2011**, *6*, 103.

(16) Groenewolt, M.; Antonietti, M. *Adv. Mater.* **2005**, *17*, 1789.

(17) Thomas, A.; Goettmann, F.; Antonietti, M. *Chem. Mater.* **2008**, *20*, 738.

(18) Chen, J.; Takanabe, K.; Ohnishi, R.; Lu, D.; Okada, S.; Hatasawa, H.; Morioka, H.; Antonietti, M.; Kubota, J.; Domen, K. *Chem. Commun.* **2010**, *46*, 7492.

(19) Zhao, H.; Lei, M.; Yang, X. a.; Jian, J.; Chen, X. *J. Am. Chem. Soc.* **2005**, *127*, 15722.

(20) Yuliati, L.; Yang, J.-H.; Wang, X.; Maeda, K.; Takata, T.; Antonietti, M.; Domen, K. *J. Mater. Chem.* **2010**, *20*, 4295.

(21) Fischer, A.; Müller, J. O.; Antonietti, M.; Thomas, A. *ACS Nano* **2008**, *2*, 2489.

(22) Thomas, A.; Fischer, A.; Goettmann, F.; Antonietti, M.; Muller, J.-O.; Schlogl, R.; Carlsson, J. M. *J. Mater. Chem.* **2008**, *18*, 4893.

(23) Ohnishi, R.; Takanabe, K.; Katayama, M.; Kubota, J.; Domen, K. *J. Phys. Chem. C* **2012**, *117*, 496.

(24) Garcia-Esparza, A. T.; Cha, D.; Ou, Y.; Kubota, J.; Domen, K.; Takanabe, K. *ChemSusChem* **2013**, *6*, 168.

(25) Polychronopoulou, K.; Rebholz, C.; Baker, M. A.; Theodorou, L.; Demas, N. G.; Hinder, S. J.; Polycarpou, A. A.; Doumanidis, C. C.; Böbel, K. *Diamond Relat. Mater.* **2008**, *17*, 2054.

(26) S. Nazari1, A. S., A. Shafyei *Journal of Advanced Materials and Processing* **2013**, *Vol. 1, No. 1* 9.

(27) Ohnishi, R.; Katayama, M.; Cha, D.; Takanabe, K.; Kubota, J.; Domen, K. *J. Electrochem. Soc.* **2013**, *160*, F501.

(28) Alhajri, N. S.; Anjum, D. H.; Takanabe, K. *J. Mater. Chem* **2014**, *2*, 10548.

(29) Wang, R.; Yang, J.; Shi, K.; Wang, B.; Wang, L.; Tian, G.; Bateer, B.; Tian, C.; Shen, P.; Fu, H. *RSC Advances* **2013**, *3*, 4771.

(30) Saha, N. C.; Tompkins, H. G. *J. Appl. Phys.* **1992**, *72*, 3072.

(31) Lu, F.-H.; Chen, H.-Y. *Thin Solid Films* **1999**, *355–356*, 374.

(32) Vasile, M. J.; Emerson, A. B.; Baiocchi, F. A. *J Vac Sci Technol A* **1990**, *8*, 99.

(33) Irie, H.; Watanabe, Y.; Hashimoto, K. *J. Phys. Chem. B* **2003**, *107*, 5483.

(34) Drygaś, M.; Czosnek, C.; Paine, R. T.; Janik, J. F. *Chem. Mater.* **2006**, *18*, 3122.

(35) Tucker, M. D.; Czigány, Z.; Broitman, E.; Näslund, L.-Å.; Hultman, L.; Rosen, J. *J. Appl. Phys.* **2014**, *115*, 144312.

(36) Rodil, S. E. M., N. A. ; Robertson, J. ; Milne, W. I. *Phys. Status Solidi A* **1999**, *174*, 25.

(37) Garfunkel, E.; Mayer, J. T.; Diebold, U.; Madey, T. E. *J. Electron. Spectrosc. Relat. Phenom.* **1995**, *73*, 1.

(38) Avasarala, B.; Haldar, P. *Electrochim. Acta* **2010**, *55*, 9024.

(39) Wu, M. *J. Alloys Compd.* **2009**, *486*, 223.

(40) Joshi, U. A.; Chung, S. H.; Lee, J. S. *J. Solid State Chem.* **2005**, *178*, 755.

(41) Elangovan, T.; Kuppusami, P.; Thirumurugesan, R.; Ganesan, V.; Mohandas, E.; Mangalaraj, D. *Materials Science and Engineering: B* **2010**, *167*, 17.

(42) Zhang, X.-J.; Ma, T.-Y.; Yuan, Z.-Y. *J. Mater. Chem.* **2008**, *18*, 2003.

(43) Delplancke-Ogletree, M.-P.; Monteiro, O. R. *J Vac Sci Technol A* **1997**, *15*, 1943.

(44) Chang, Y. H.; Won, S. J.; Oh, J. E.; Paek, S. H.; Lee, H. D.; Choi, J. S.; Lee, S. I.; Ahn, S. T.; Lee, J. G. *Jpn. J. Appl. Phys.* **1995**, *34*, L907.

(45) Pierson, H. O. *Handbook of Refractory Carbides and Nitrides*; William Andrew Publishing: Norwich, United States, 1996.

(46) Izhevskyi, V. A.; Genova, L. A.; Bressiani, J. C. *Materials Research* **1999**, *2*, 271.

(47) Hryha, E.; Rutqvist, E.; Nyborg, L. *Surf. Interface Anal.* **2012**, *44*, 1022.

(48) Sricharoenchai, C. L. a. P. *JOM-J MIN MET MAT S* **2012**, *22*, 7.

(49) Choi, J.-G. *Appl. Surf. Sci.* **1999**, *148*, 64.

(50) Romanyuk, A.; Steiner, R.; Marot, L.; Spassov, V.; Oelhafen, P. *Thin Solid Films* **2008**, *516*, 8513.

(51) Liu, J.; Zhang, T.; Wang, Z.; Dawson, G.; Chen, W. *J. Mater. Chem.* **2011**, *21*, 14398.

(52) Alhajri, N. S.; Yoshida, H.; Anjum, D. H.; Garcia-Esparza, A. T.; Kubota, J.; Domen, K.; Takanabe, K. *J. Mater. Chem* **2013**, *1*, 12606.

(53) Haasch, R. T.; Lee, T.-Y.; Gall, D.; Greene, J. E.; Petrov, I. *Surf. Sci. Spectra* **2000**, *7*, 233.

(54) de Souza, E. F.; Chagas, C. A.; Ramalho, T. C.; de Alencastro, R. B. *Dalton Transactions* **2012**, *41*, 14381.

(55) Zhang, F.; Zhang, T.; Yang, X.; Zhang, L.; Leng, K.; Huang, Y.; Chen, Y. *Energy Environ Sci* **2013**, *6*, 1623.

(56) Ma, S.-f.; Liang, J.; Zhao, J.-f.; Xu, B.-s. *CrystEngComm* **2010**, *12*, 750.

(57) Özer, N.; Rubin, M. D.; Lampert, C. M. *Sol. Energy Mater. Sol. Cells* **1996**, *40*, 285.

(58) Jouve, G.; Séverac, C.; Cantacuzène, S. *Thin Solid Films* **1996**, *287*, 146.

(59) Brown, I. *J VAC SCI TECHNOL A* **2001**, *19*, 2048.

(60) Newport, A. C.; Bleau, J. E.; Carmalt, C. J.; Parkin, I. P.; O'Neill, S. A. *J. Mater. Chem.* **2004**, *14*, 3333.

(61) Thiede, T. B.; Parala, H.; Reuter, K.; Passing, G.; Kirchmeyer, S.; Hinz, J.; Lemberger, M.; Bauer, A. J.; Barreca, D.; Gasparotto, A.; Fischer, R. A. *Chem. Vap. Deposition* **2009**, *15*, 334.

(62) Dong, F.; Li, Y.; Ho, W.; Zhang, H.; Fu, M.; Wu, Z. *Chin. Sci. Bull.* **2014**, *59*, 688.

(63) Ramanathan, S.; Oyama, S. T. *J. Phys. Chem. A* **1995**, *99*, 16365.

(64) He, C.; Jiang, S. P.; Shen, P. K. *Sci. Rep.* **2013**, *3*.

(65) Ma, J.; Wu, M.; Du, Y.; Chen, S.; Jin, W.; Fu, L.; Yang, Q.; Wen, A. *J. Alloys Compd.* **2009**, *475*, 415.

(66) Biesinger, M. C.; Brown, C.; Mycroft, J. R.; Davidson, R. D.; McIntyre, N. S. *Surf. Interface Anal.* **2004**, *36*, 1550.

(67) Jiang, T.; Odnevall Wallinder, I.; Herting, G. *isrn corros.* **2012**, *2012*, 10.

(68) Allen, G. C.; Curtis, M. T.; Hooper, A. J.; Tucker, P. M. *J. Chem. Soc., Dalton Trans.* **1973**, 1675.

(69) Conde, A.; Cristóbal, A. B.; Fuentes, G.; Tate, T.; de Damborenea, J. *Surf. Coat. Technol.* **2006**, *201*, 3588.

(70) Hassel, M.; Hemmerich, I.; Kuhlenbeck, H.; Freund, H.-J. *Surf. Sci. Spectra* **1996**, *4*, 246.

(71) Maury, F.; Ossola, F. *Appl. Organomet. Chem.* **1998**, *12*, 189.

(72) Detroye, M.; Reniers, F.; Buess-Herman, C.; Vereecken, J. *Appl. Surf. Sci.* **1999**, *144–145*, 78.

(73) Khyzhun, O. Y. *J. Alloys Compd.* **2000**, *305*, 1.

(74) Xie, F. Y.; Gong, L.; Liu, X.; Tao, Y. T.; Zhang, W. H.; Chen, S. H.; Meng, H.; Chen, J. *J. Electron. Spectrosc. Relat. Phenom.* **2012**, *185*, 112.

(75) Kerkhof, F. P. J. M.; Moulijn, J. A.; Heeres, A. *J. Electron. Spectrosc. Relat. Phenom.* **1978**, *14*, 453.

(76) Ganesan, R.; Lee, J. S. *Angew. Chem.* **2005**, *117*, 6715.

(77) Krasovskii, P. V.; Malinovskaya, O. S.; Samokhin, A. V.; Blagoveshchenskiy, Y. V.; Kazakov, V. A.; Ashmarin, A. A. *Appl. Surf. Sci.* **2015**, *339*, 46.

(78) Bchir, O. J.; Kim, K. C.; Anderson, T. J.; Craciun, V.; Brooks, B. C.; McElwee-White, L. *J. Electrochem. Soc.* **2004**, *151*, G697.

(79) Lohmar, J.; Rickert, H. *J. Chem. Thermodyn.* **1978**, *10*, 1209.

(80) Wriedt, H. A. *Bull Alloy Phase Diagr* **1989**, *10*, 358.

List of figures

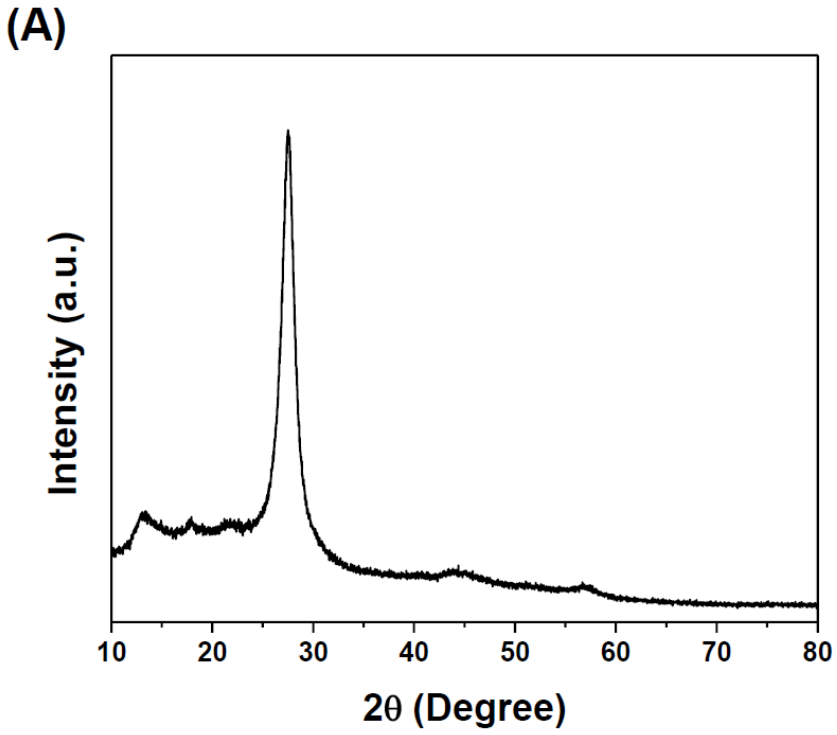

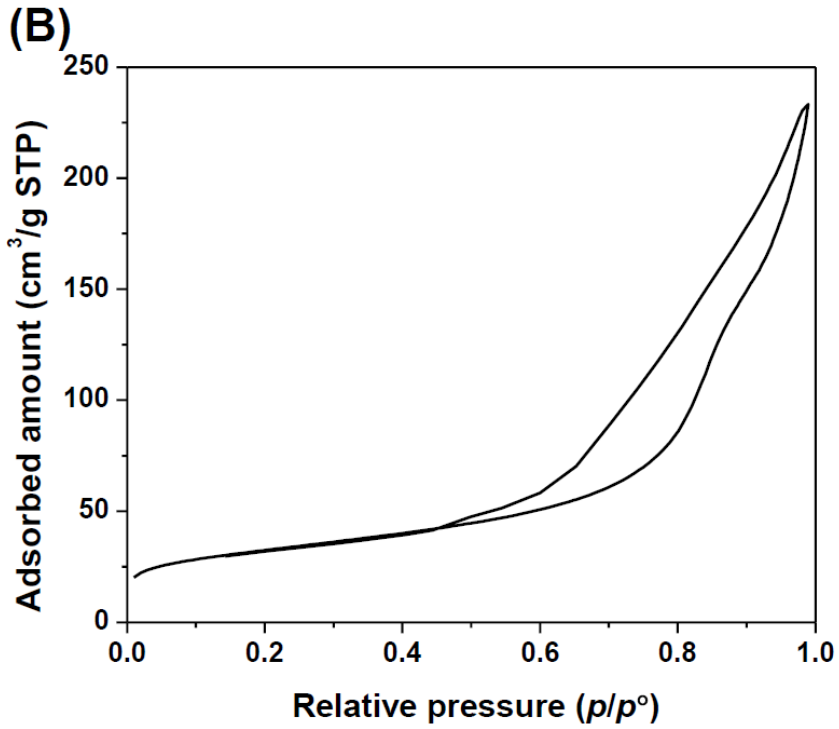

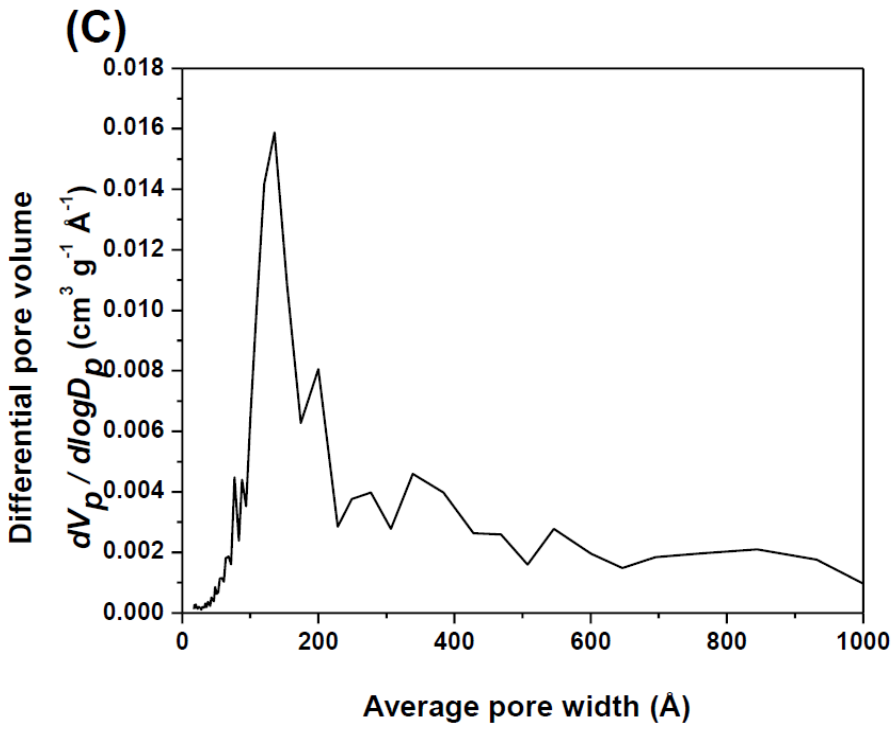

Fig. 1 (A) XRD patterns, (B) N_2 adsorption–desorption isotherms, and (C) the pore size distributions obtained from the N_2 desorption studies at 77 K for the mpg-C_3N_4 template used in this study.

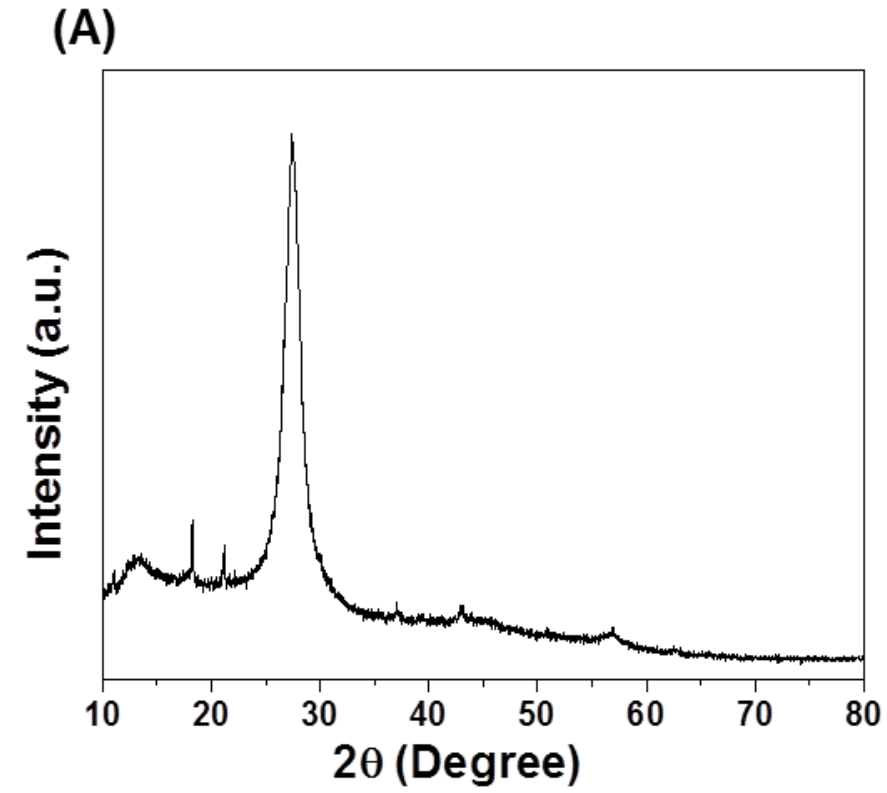
(A)
Intensity (a.u.)
10
20
30
40
50
60
70
80
2θ (Degree)

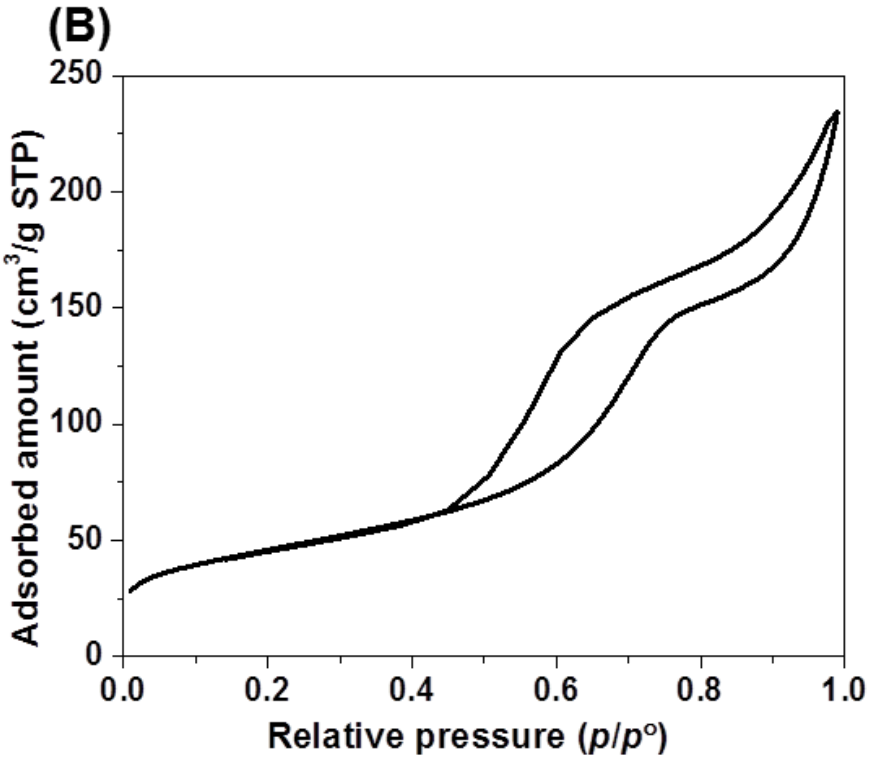
(B)
Adsorbed amount (cm3/g STP)
250
200
150
100
50
0
0.0
0.2
0.4
0.6
0.8
1.0
Relative pressure (p/p°)

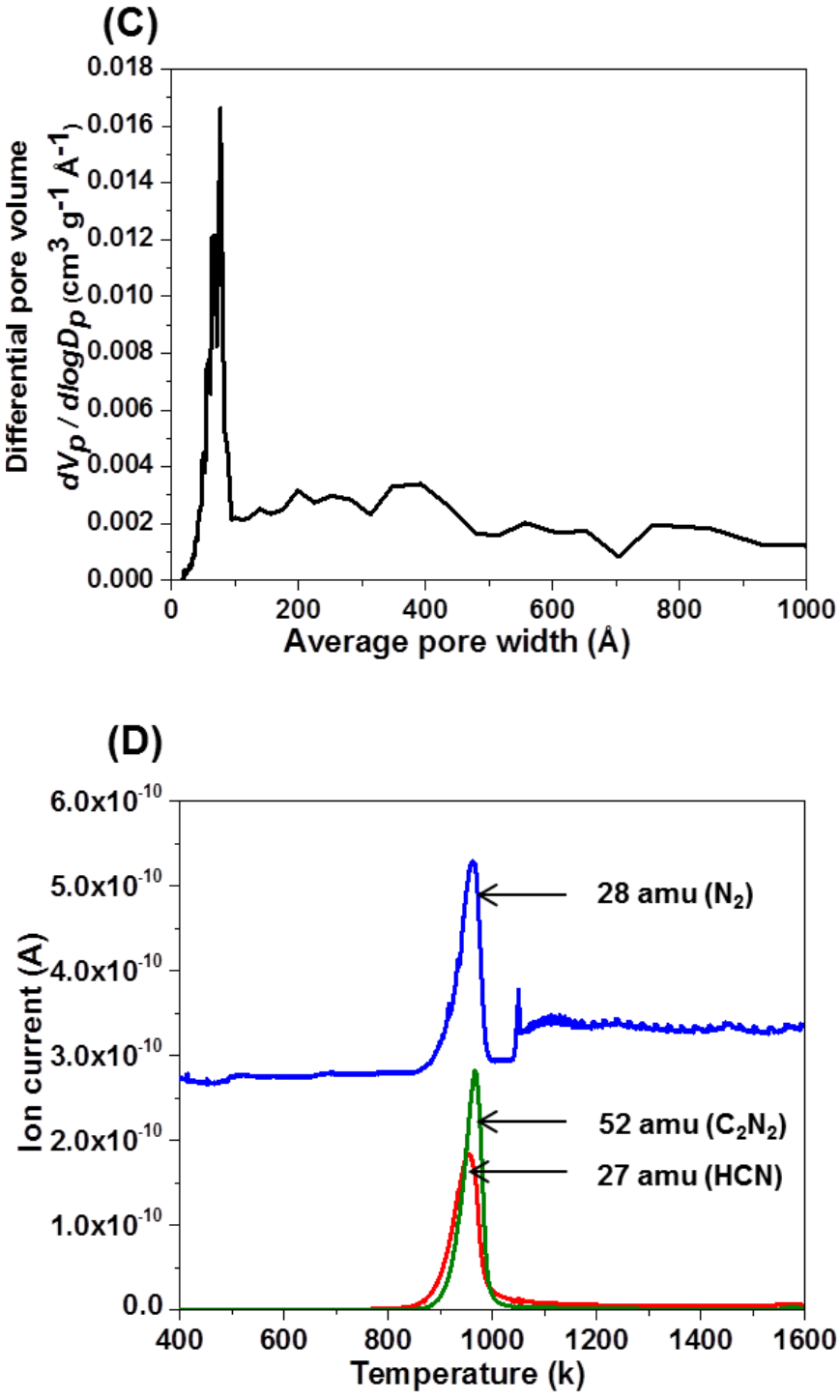

Fig. 2 (A) XRD patterns, (B) N_2 adsorption–desorption isotherms, (C) the pore size distributions obtained from the N_2 desorption studies at 77 K, and (D) MS signals obtained under Ar during the temperature programmed decomposition of the mpg-C_3N_4 template used in this study.

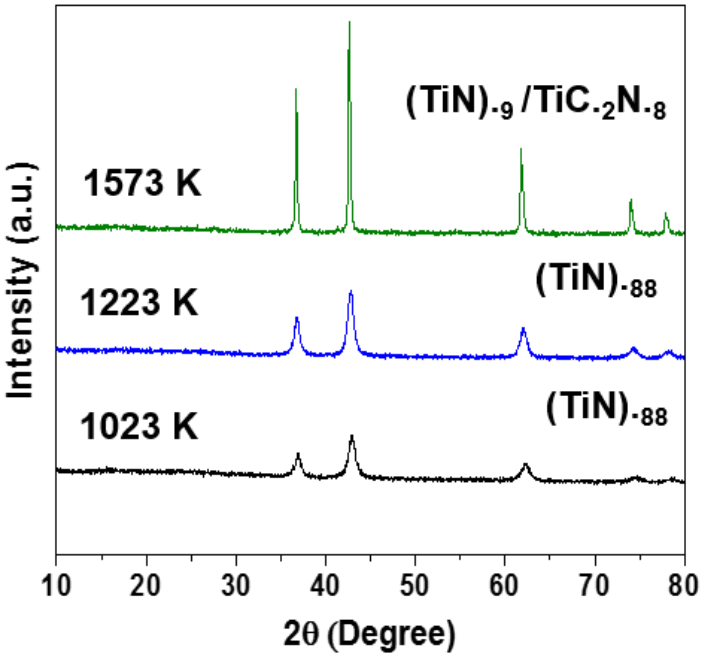

Fig. 3 The effects of the reaction temperature on the XRD patterns of the titanium –based products synthesized under N_2 flow.

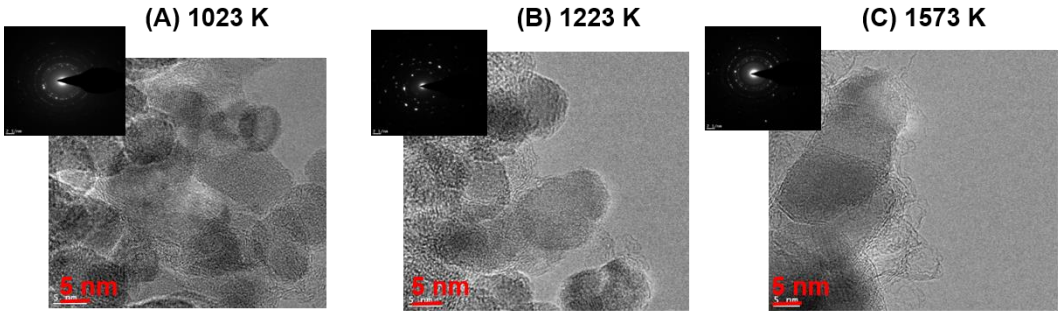

Fig. 4 TEM micrographs of titanium based products synthesized at different temperatures.

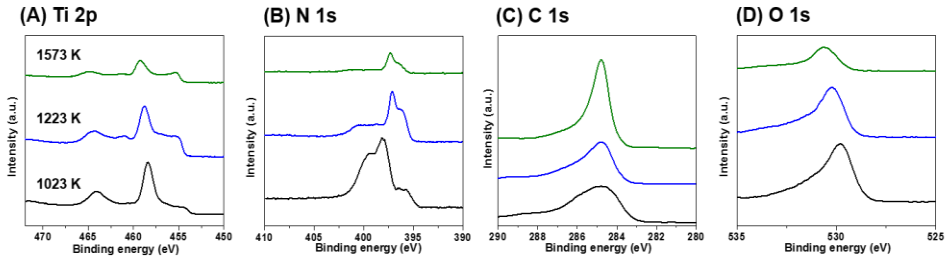

Fig. 5 XPS spectra for (A) Ti 2p (B) N 1s (C) C 1s and (D) O 1s of titanium based products obtained at different temperatures under N_2 flow.

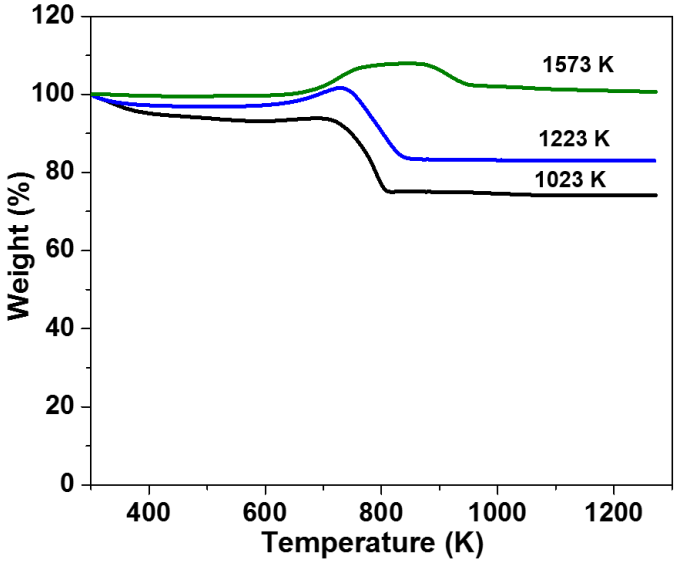

Fig. 6 TGA results of titanium based products synthesized at different temperatures under air flow.

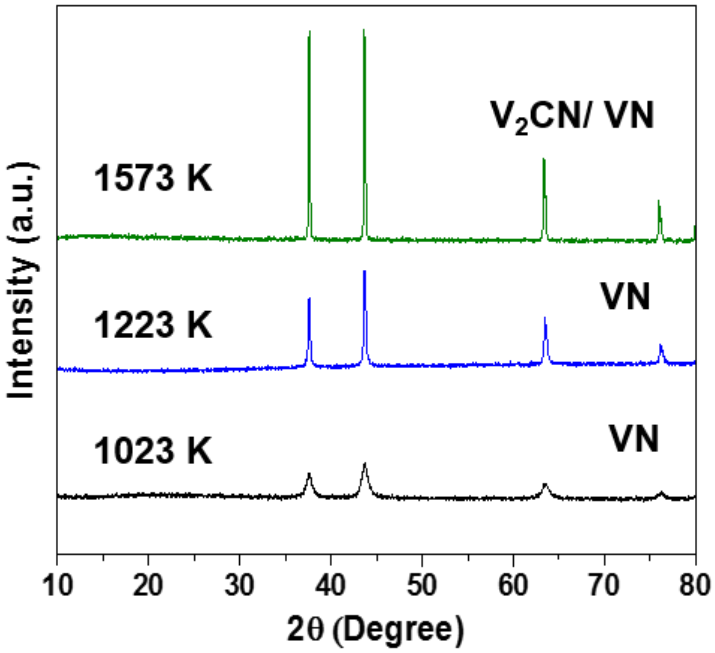

Fig. 7 The effects of the reaction temperature on the XRD patterns of the vanadium based products synthesized under N_2 flow.

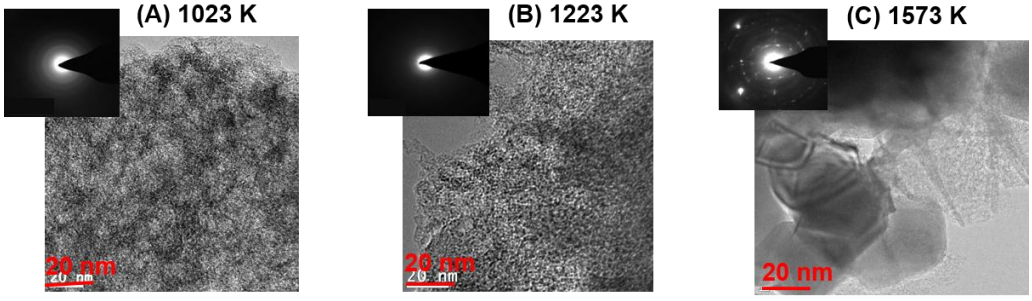

Fig. 8 TEM micrographs of vanadium based products synthesized at different temperatures.

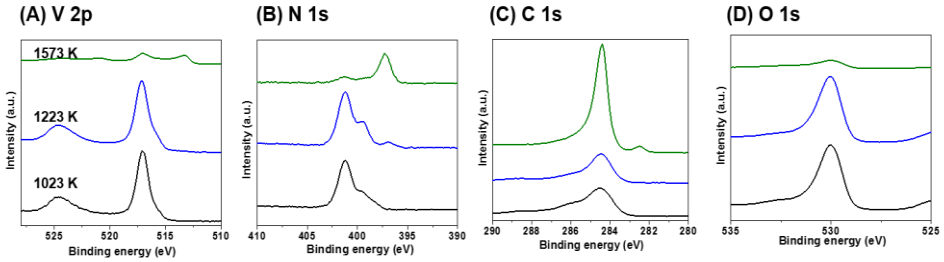

Fig. 9 XPS spectra for (A) V 2p (B) N 1s (C) C 1s and (D) O 1s of vanadium based products obtained at different temperatures under N_2 flow.

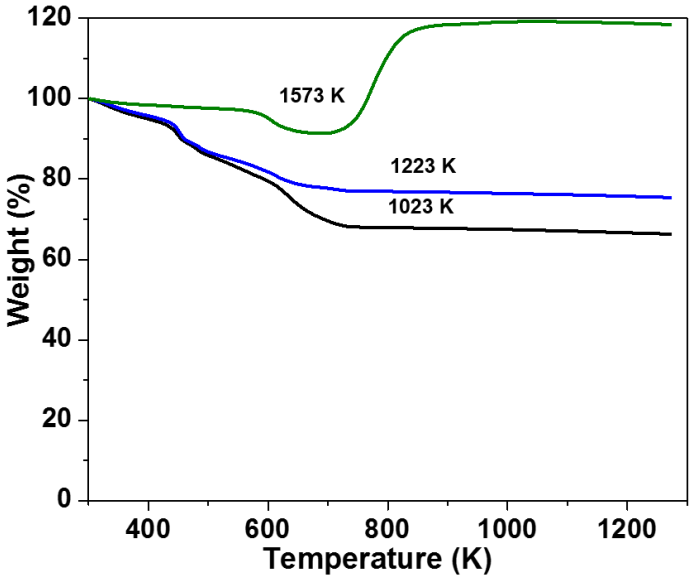

Fig. 10 TGA results of vanadium based products synthesized at different temperatures under air flow.

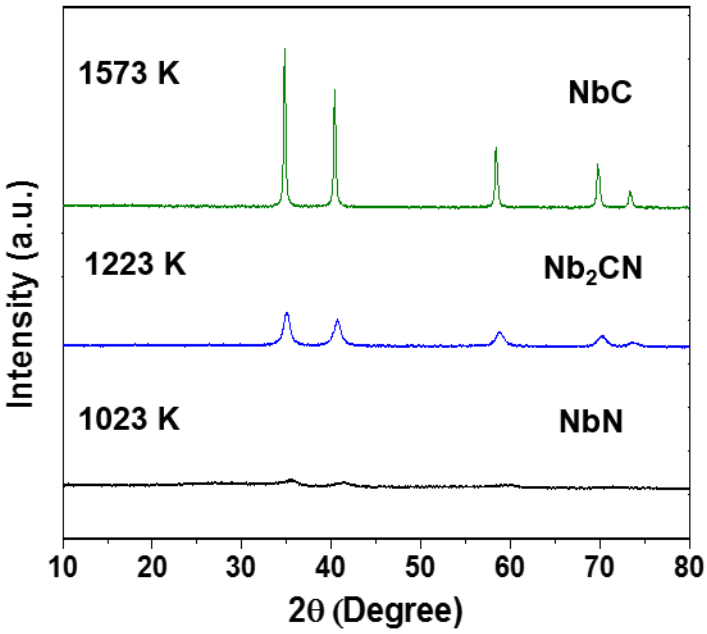

Fig. 11 The effects of the reaction temperature on the XRD patterns of the niobium –based products synthesized under N_2 flow.

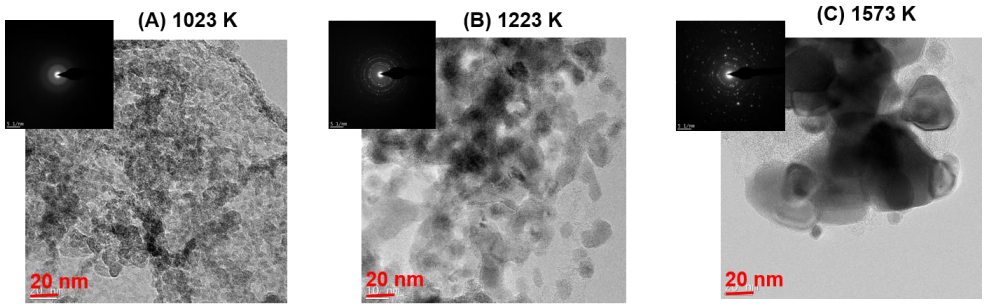

Fig. 12 TEM micrographs of niobium based products synthesized at different temperatures.

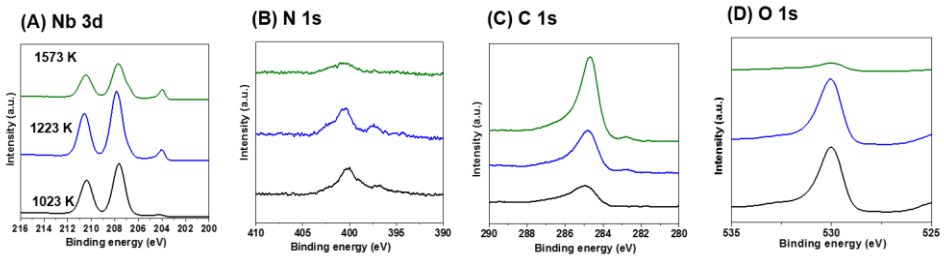

Fig. 13 XPS spectra for (A) Nb 3d (B) N 1s (C) C 1s and (D) O 1s of niobium based products obtained at different temperatures under N_2 flow.

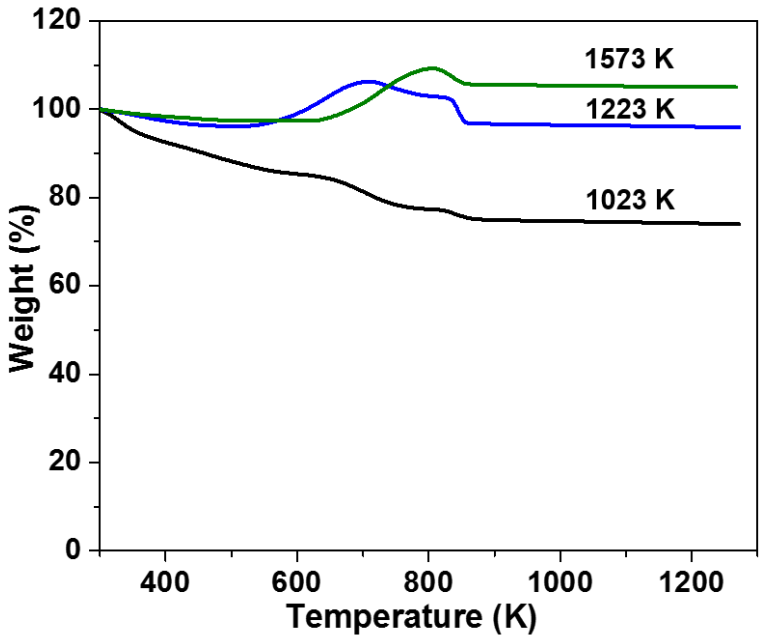

Fig. 14 TGA results of niobium based products synthesized at different temperatures under air flow.

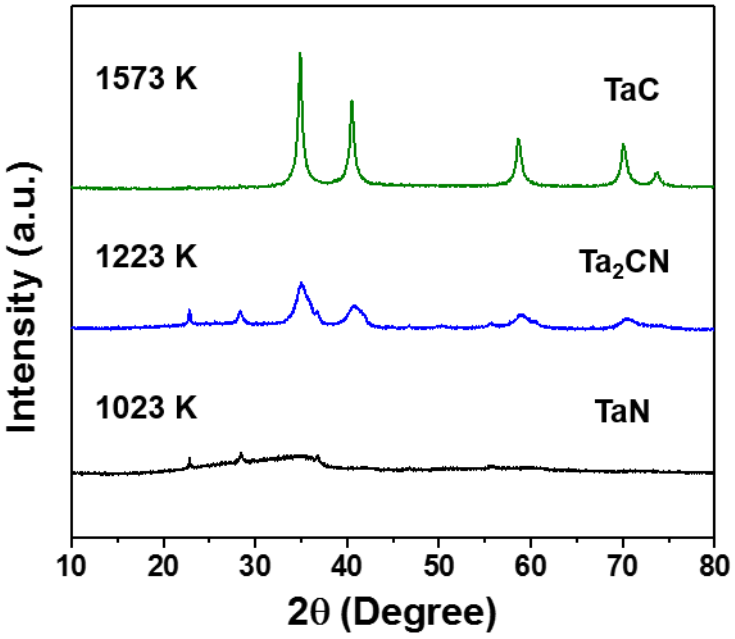

Fig. 15 The effects of the reaction temperature on the XRD patterns of the tantalum –based products synthesized under N_2 flow.

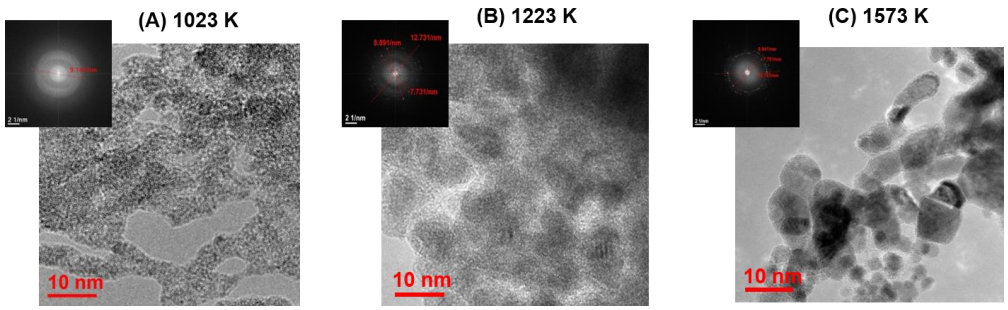

Fig. 16 TEM micrographs of tantalum based products synthesized at different temperatures.

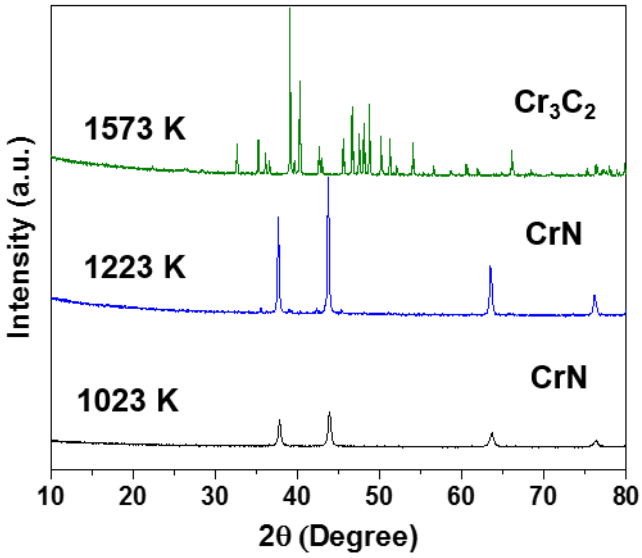

Fig. 17 The effects of the reaction temperature on the XRD patterns of the chromium – based products synthesized under N_2 flow.

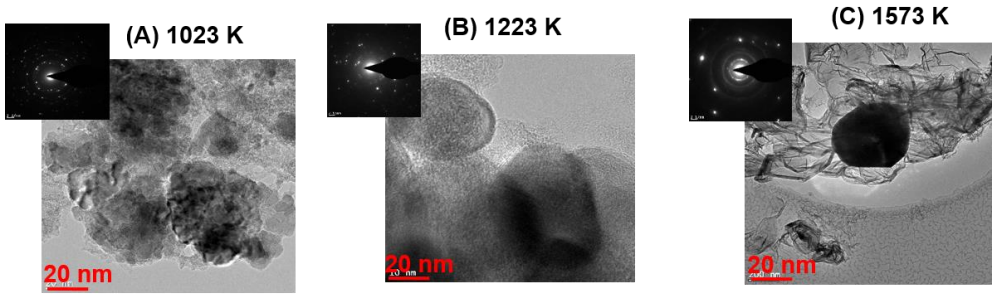

Fig. 18 TEM micrographs of chromium based products synthesized at different temperatures.

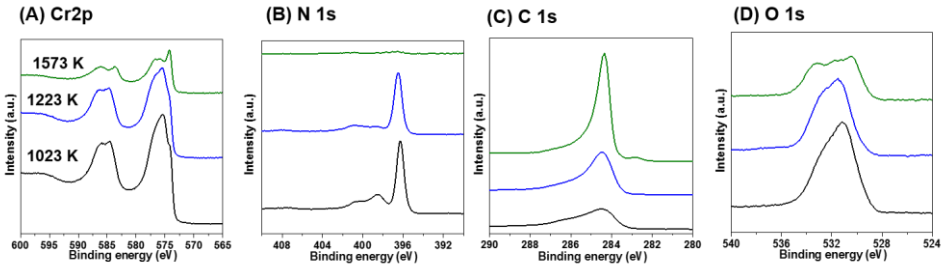

Fig. 19 XPS spectra for (A) Cr 2p (B) N 1s (C) C 1s and (D) O 1s of chromium based products obtained at different temperatures under N_2 flow.

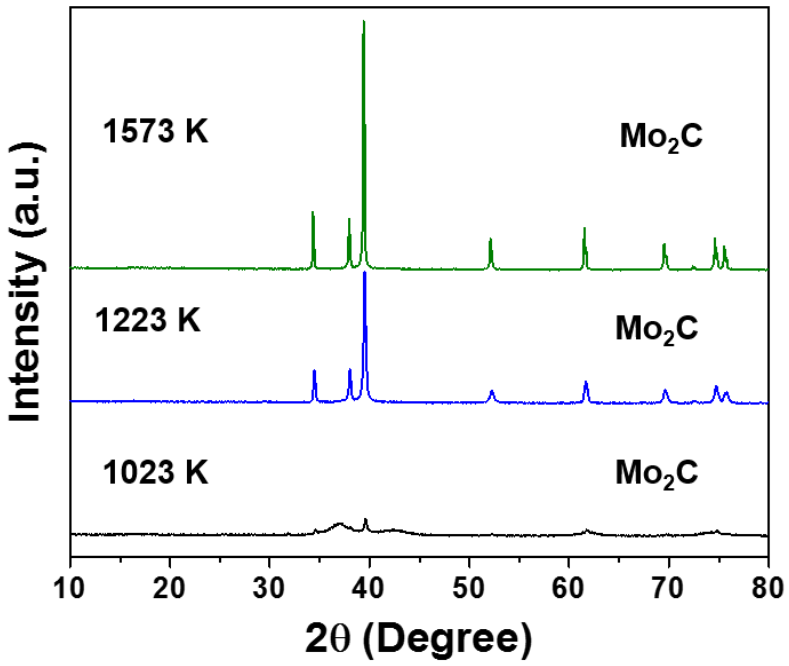

Fig. 20 The effects of the reaction temperature on the XRD patterns of molybdenum carbide–carbon nanocomposites synthesized under N_2 flow.

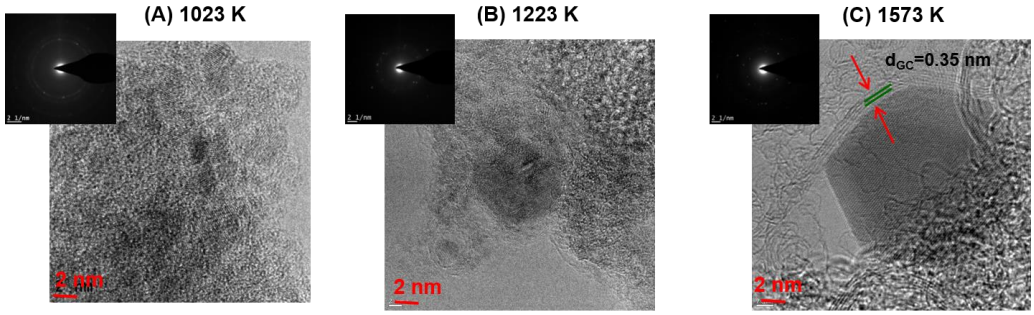

Fig. 21 TEM micrographs of molybdenum carbide–carbon nanocomposites synthesized at different temperatures.

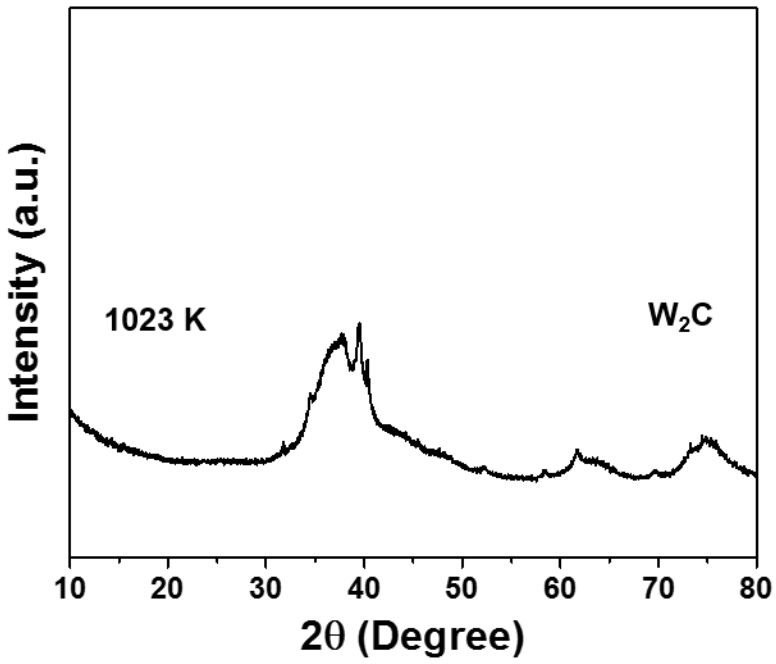

Fig. 22 XRD pattern of tungsten carbide synthesized under N_2 flow at 1023 K.

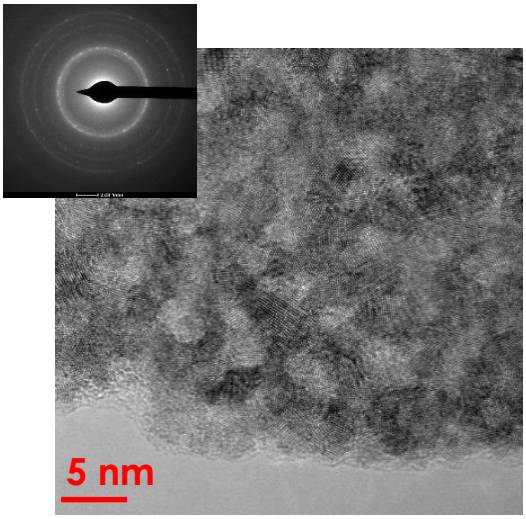

Fig. 23 TEM micrographs of tungsten carbide synthesized under flow of N_2 at 1023 K.

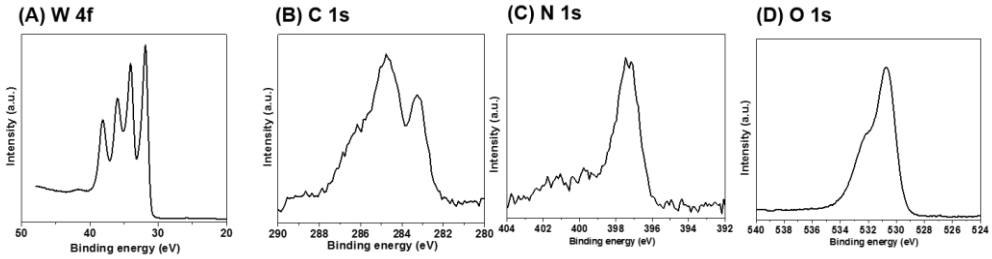

Fig. 24 XPS spectra for (A) W 4f (B) C 1s and (C) N 1s and (D) O 1s of tungsten carbide synthesized under flow of N_2 at 1023 K.

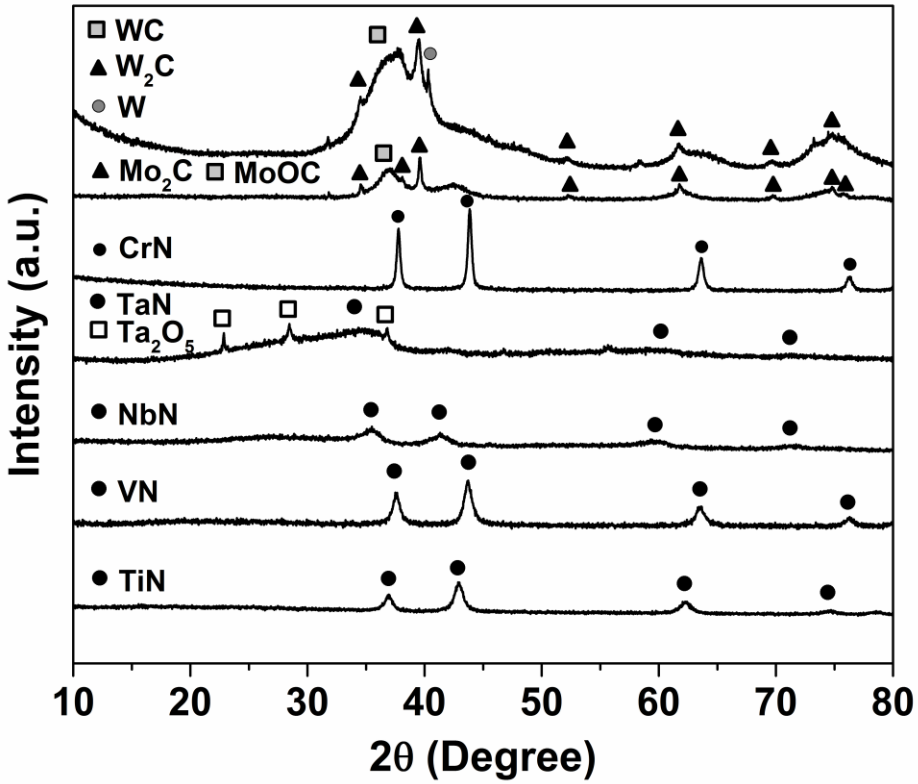

Fig. 25 XRD patterns for various samples synthesized at 1023 K under flow of N_2 at constant weight ratio of 1:1 (TM/C_3N_4).

List of tables

Transition metals	Temperature (K) under N_2 flow	C (%)	N (%)	Crystallite size (nm)	BET Surface area (m^2/g)	Phase
Ti	1023	18.6	20.9	12	146	$(TiN)_{.88}$
	1223	24.6	16.3	14	187	$(TiN)_{.88}$ $TiC_{.2}N_{.8}$
	1573	20.8	15.3	39	152	$(TiN)_{.90}$ $TiC_{.2}N_{.8}$
V	1023	10.1	9.1	14	171	VN
	1223	9.1	9.4	36	168	VN
	1573	20	6.1	48	95	VN V_2CN
Nb	1023	9.3	6.8	-	157	NbN
	1223	10	4.5	11	127	Nb_2CN
	1573	14	0.8	36	90	NbC
Ta	1023	3.7	4.8	-	107	TaN
	1223	4.8	3	6	81	Ta_2CN
	1573	10.5	0.9	19	99	TaC
Cr	1023	8	12	24	15.5	CrN
	1223	10	10	38	-	CrN
	1573	17	0.5	-	-	Cr_3C_2
Mo	1023	21	1.3	-	120	Mo_2C
	1223	22	0.6	27	300	Mo_2C
	1573	24	0.0	52	277	Mo_2C
W	1023	3.5	0.3	-	17.5	W_2C

Table 1 Synthesis temperature, elemental analyses, phase assignments from the XRD diffractograms, crystallite size evaluations from the Scherrer equation, and BET surface areas for interstitial nitride and carbide nanoparticles obtained at various temperatures under N_2 flow.

Nitride	ΔG°_{298}	Carbide	ΔG°_{298}
$Ti + 1/2N_2 \rightarrow TiN$	-309	$Ti + C \rightarrow TiC$	-181
$V + 1/2N_2 \rightarrow VN$	-191	$V + C \rightarrow VC$	-99
$Nb + 1/2N_2 \rightarrow NbN$	-206	$Nb + C \rightarrow NbC$	-136.9
$Ta + 1/2N_2 \rightarrow TiN$	-224	$Ta + C \rightarrow TiC$	-142.6
$Cr + 1/2N_2 \rightarrow CrN$	-92.8	$Cr + 3/2C \rightarrow 1/3Cr_3C_2$	-102.1
$Mo + 1/4N_2 \rightarrow 1/2Mo_2N$	-27.3	$Mo + 1/2C \rightarrow Mo_2C$	-58.82
$W + 1/4N_2 \rightarrow 1/2W_2N$	+39.0	$W + C \rightarrow WC$	-38.48

Table 2 Standard formation energy of various transition metal nitrides and carbides.[79,80]

CHAPTER 3

Synthesis of tantalum carbide and nitride nanoparticles using a reactive mesoporous template for electrochemical hydrogen evolution

Tantalum carbide and nitride nanocrystals were prepared through the reaction of a tantalum precursor with mesoporous graphitic (mpg)-C_3N_4. The effects of the reaction temperature, the ratio of the Ta precursor to the reactive template (mpg-C_3N_4), and the selection of the carrier gas (Ar, N_2 and NH_3) on the resultant crystal phases and structures were investigated. The produced samples were characterized using powder X-ray diffraction (XRD), CHN elemental analyses, thermogravimetric analyses (TGA), nitrogen sorption, a temperature-programmed reaction with mass spectroscopy (MS), X-ray photoelectron spectroscopy (XPS), and transmission electron microscopy (TEM). The results indicate that the different tantalum phases with cubic structure, TaN, Ta_2CN, and TaC, can be formed under a flow of nitrogen when formed at different temperatures. The Ta_3N_5 phase with a Ta^{5+} oxidation state was solely obtained at 1023 K under a flow of ammonia, which gasified the C_3N_4 template and was confirmed by detecting the decomposed gaseous products via MS. Significantly, the formation of TaC, Ta_2CN, and TaN can be controlled by altering the weight ratio of the C_3N_4 template relative to the Ta precursor at 1573 K under a flow of nitrogen. The high C_3N_4/Ta precursor ratio generally resulted in high carbide content rather than a nitride one, consistent with the role of mpg-C_3N_4 as a carbon source. Electrochemical measurements revealed that the synthesized nanomaterials were consistently able to produce hydrogen under acidic conditions (pH 1). The obtained Tafel slope indicates that the rate-determining step is the Volmer discharge step, which is

consistent with adsorbed hydrogen being weakly bound to the surface during electrocatalysis.

Introduction

Electrochemical and photoelectrochemical energy conversions serve key roles in carbon-free energy systems obtained from renewable energy sources when solar, wind, and geothermal energy are converted to chemical energy.[1–3] Among the reactions related to energy conversion, the hydrogen evolution reaction (HER) is one of the most intensively studied electrochemical reactions in water and chloro-alkali electrolysis; this reaction requires an effective catalyst to overcome the large overpotential and to produce hydrogen in an affordable manner.[4–10] A good catalyst candidate for HER has a metal d band situated at the Fermi level that interacts adequately with the adsorbate and broadens its valence orbital, thereby decreasing the activation energy.[5–8] Selecting catalytically active materials for HER that possess large active surface areas per unit volume as well as materials with high stability at significant current densities in extreme reaction conditions (typically highly acidic or highly basic) is important.[1]To date, electrolytic HER depends on the use of noble metals, such as platinum, as stable electrocatalysts, which are active at low overpotentials.[4,5,8–10] However, noble metals are scarce and expensive, hence the fact that non-noble metal electrocatalysts remain a widely studied option. Under acidic conditions, where a high HER current is mechanistically expected, most non-noble metals are unstable, while some recent efforts have been devoted to the use of transition metal sulfide,[11–13] carbide,[14–16] and nitrides[17] due to their high tolerance to acid. These compounds possess a unique combination of physical and chemical properties, which have attracted researchers

working on both the fundamental investigations and on practical applications of these materials.[18,19] A tremendous amount of attention has been focused on molybdenum sulfides as HER electrocatalysts;[11,12] however, the stability of these materials is questionable, especially at their resting potential or while they are under just slightly oxidizing conditions. In contrast, group IV–VI transition metal carbides and nitrides are stable under a wide range of electrocatalytic operating conditions.[14,19] These metals are interstitial alloys in which the carbon and nitrogen atoms occupy the interstitial lattice positions of the metal.[18] These metal alloys have properties similar to those of noble metals, as well as properties that result from strong metal-to carbon bonds.[20] Synthesis of carbide and nitride materials has been performed through various methods that generally require high temperatures and high pressures.[21–28] Many transition metal carbides and nitrides are able to form solid solutions (carbonitride phases) that can be tailored by controlling the C/N ratio.[25,26] Therefore, electronic structure studies of transition metal carbides and nitrides are of great significance in the theoretical and experimental sciences.[18,19] However, the use of nanoscale nitrides and carbides in catalysis has been limited because of the difficulty in their syntheses. While their metallic nature allows for their utilization as bulk components,[14] the electrocatalytic performances of these bulk components remain unattractive due to non-negligible resistances and a lack of active sites per unit area.[14,19] More recently, the synthetic procedures of metal nitride nanoparticles, such as TiN, TaN, and VN, were reported using nanometer-sized confinement conditions in mesoporous graphitic (mpg-C_3N_4) as a reactive hard template.[29–32] Giordano et al. also reported a soft urea glass method to produce molybdenum and tungsten carbides and nitrides with sizes on the order of ten nanometers.[33–36] Interestingly, the urea-to-metal precursor ratio has a

significant effect on the final composition of the nanoparticles: as the concentration of urea increases, there is a corresponding increase in carbide formation.[33] The literature demonstrated that nano-scale tungsten carbide particles, which can be synthesized using mpg-C_3N_4 as a reactive template, showed a high performance and a high stability for HER that was approaching the performance of Pt.[15] Thus, this approach to form nanocarbide crystals presents a tremendous opportunity for their utilization and is worth investigating for use in catalytic applications, such as electrochemical HER. In this study, different crystal phases of tantalum carbides, carbonitrides, and nitrides were synthesized for the first time after reacting a tantalum precursor with mpg-C_3N_4 at different temperatures under flows of nitrogen, argon, and ammonia gases. A series of experiments that varied the precursor ratio with respect to the reactive template, the synthesis temperature, and the carrier gas clearly demonstrated the formation of different compositions and structures in the final products. The electrocatalytic activities of the obtained samples for HER in acidic media possessed very stable performances with significant improvement in their catalytic performances when compared to previously reported bulk materials.

Experimental

Syntheses of tantalum carbide, carbonitride, and nitride nanoparticles

A series of experiments were conducted that varied the ratio of the mpg-C_3N_4 with respect to the precursor, the synthesis temperatures, and the carrier gas (N_2, Ar, or NH_3). First, a colorless solution was prepared from tantalum chloride (0.6 g; $TaCl_5$; ≥99.9% Aldrich) that was dissolved in ethanol (0.72 ml). Then, the pores of the reactive template (0.6 g) were immersed with the aforementioned solution. The final mixture was placed in an alumina

boat crucible and heated to different temperatures in the range of 1023 to 1573 K under a flow of 100 ml min^{-1} of one of the different gases (N_2, Ar, or NH_3). At the end of the synthetic procedure, a passivation process was applied by flowing 100 ml min^{-1} of 1% O_2 in He at room temperature. Notably, caution is required when working with this process because thermal decomposition of C_3N_4 causes the formation of hydrogen cyanide and cyanogen gases.

Characterization

The synthesized samples were characterized using elemental analyses (C, H, and N), X-ray diffraction (XRD), N_2 sorption, thermogravimetric analyses (TGA), X-ray photoelectron spectroscopy (XPS), a temperature-programmed reaction with mass spectroscopy (MS), and transmission electron microscopy (TEM). Elemental analyses were performed using a Flash 2000 Thermo Scientific CHNS/O analyzer. The XRD patterns of the products were collected on a Bruker DMAX 2500 X-ray diffractometer using Cu Kα radiation (λ = 0.154 nm). The N_2 sorption studies were conducted using a Micrometrics ASAP 2420 to determine the Brunauer–Emmett–Teller (BET) surface area, the Barret–Joyer–Halenda (BJH) pore size, and the pore volume. The tantalum carbide decomposition products in the gas phase during nanoparticle synthesis were monitored using an OMNI Star (GSD320 O1) portable mass spectrometer with a tungsten filament from Pfeiffer Vacuum. The mass spectrometer was connected at the furnace outlet to study the decomposition products under an Ar flow of 100 ml min^{-1}. TGA were performed in a Mettler–Toledo TGA/DSC1 Star system under a flow of 100 ml min^{-1} of air. The XPS spectra were obtained from AMICUS/ESCA 3400 KRATOS using Mg anodes at 12 kV

and 10 mA. A prominent maximum peak of carbon 1s at 284.8 eV was used as a reference to calibrate the XPS spectrum. A TITAN ST transmission electron microscope operated at 300 kV was used to characterize the sample and obtain the particle size distribution. Fast-Fourier transforms (FFT) of the acquired micrographs were calculated to measure the inter-planar spacings (d-spacings) of the crystalline phases present in the samples.

Electrochemical measurements

The electrocatalytic activities of the samples for HER were studied using a rotating disk electrode (RDE). The working electrode was first prepared utilizing the following procedure. First, 2mg of a tantalum-based sample was dispersed in 56.3 mL of a 25% nafion solution that had been diluted by ethanol. The solution was then sonicated for 30 min. Then, 2 mL of the suspension was drop-coated onto a glassy carbon electrode (GCE) with a geometric surface area of 0.071 cm^2 to provide a weight density of 0.25 mg cm^{-2}. Finally, the electrode was put in an oven and heated at 373 K under air for 1 h. The electrocatalytic measurements were conducted using a 16-channel, research grade potentiostat system (VMP3) from BioLogic Science Instruments. The electrochemical cell used in this study was a three-electrode cell. An Ag/AgCl electrode saturated in KCl was used as a reference electrode. The counter electrode was a carbon rod and all of the electrodes were immersed in the same electrolyte solution (0.05 M H_2SO_4; Fisher Chemical, Trace Metal grade). Cyclic voltammetry (CV) experiments were performed with a 5 mV s^{-1} scan rate between -0.5 and 0.3 V vs. reversible hydrogen electrode (RHE) for hydrogen evolution while maintaining a constant rotational speed of 1600 rpm.

Results and discussion

Temperature-programmed reaction of C_3N_4 with mass spectroscopy

The gaseous products produced during the nanoparticle syntheses were monitored using MS to follow the reaction of the reactive C_3N_4 template with the Ta precursor. Fig. 1 shows the MS signals for selected masses under the flow of inert Ar (100 ml min^{-1}) or NH_3 (100 ml min^{-1}) with a heating rate of 14 K min^{-1}. Under a flow of Ar (Fig. 2A), the major peaks started to appear at ~700 K, and the peak maxima occurred at ~950 K for signals 27, 28, and 52, which are assigned to HCN, N_2, and C_2N_2, respectively, as a result of mpg-C_3N_4 decomposition.[15] Other observed signals were 14 amu (N), 30 amu (NO), 44 amu (CO_2), and 46 amu (NO_2) at fairly minor intensities. Oxygen-containing products may have arisen from the precursor and the solvent (ethanol) that was used. Under a flow of NH_3 (Fig. 2B), drastic signal changes occurred >~900 K. The only major peak that was apparent was attributed to HCN, while the C_2N_2 signal was 52 amu (C_2N_2), which was drastically suppressed when compared to the corresponding signal under the flow of Ar. Simultaneously, the N_2 signal of 28 amu was increased monotonically and remained high due to decomposition of NH_3 to N_2 and H_2. Significantly, Ar or NH_3 yields different gaseous products, resulting in different phases of Ta products might arise. Indeed, in later discussions, TaN/C (with a lower oxidation state of Ta) was obtained under Ar (or N_2) flow, whereas Ta_3N_5 (with a Ta^{5+} state) was obtained under NH_3. These data suggest that NH_3 reacts with carbonaceous residue originating from the C_3N_4 template to form HCN, which avoids the carbo-thermal reduction with solid carbon residue prevalent at high temperatures. Additionally, the crystal phase of the tantalum product can be effectively tuned as a result of the different reactions between the different gases (inert gas or NH_3)

with the C_3N_4 template. Noteworthy, the lowest temperature of the synthesis in this study was 1023 K, which is at the end of the C_3N_4 decomposition (Fig. 2A and B).

X-ray diffraction (XRD)

The produced samples synthesized under the various conditions were characterized by XRD to determine the crystal structure. The XRD patterns are shown in Fig. 2 for the samples synthesized under nitrogen flow at different temperatures from 1023 to 1573 K while keeping the ratio of mpg-C_3N_4/$TaCl_5$ constant at 1: 1. Crystallite sizes obtained using the Scherrer equation are listed in Table 1. The XRD pattern for the sample synthesized at 1023 K shows no apparent diffraction peaks, which can be interpreted as either an ultrafine particle or an amorphous phase. For the 1123 K sample, four major peaks are evident, which corresponds to a tantalum nitride phase (TaN) (PDF 03-065-9404) that has a cubic structure with a Fm-3m (225) space group, which is in agreement with a previous report.[17,23] The XRD pattern for the sample synthesized at 1223 K matches well with tantalum carbonitride (Ta_2CN: PDF 03-065-8774), with a cubic structure with a Fm-3m (225) space group, and/or with defective tantalum carbide (C_3Ta_4 PDF 03-065-3191 and Ta_4C_3.04 PDF 01-089-2121), with a cubic structure with a pm-3m (221) space group, thus making it difficult to unambiguously assign a specific phase. At higher temperatures (1323 and 1573 K), XRD patterns show the formation of a tantalum carbide phase TaC (PDF 00-002-1023) that has a cubic structure with a Fm-3m (225) space group. The peaks become sharper as the synthesis temperature increases, most likely due to increases in crystallite size and particle aggregation. In all of the samples, some additional peaks are observed, which can be assigned to a β-Ta_2O_5 phase (PDF 01-089-2843 or PDF 01- 079-1375) that

has an orthorhombic structure with a C2mm (38) or a Pmm2 (25) space group, respectively. The oxide was likely formed during the passivation treatment with O_2 followed by exposure of the nanoparticles to the ambient conditions.

Next, the effects of C_3N_4/Ta precursor weight ratio on the crystal structure were investigated and the XRD patterns of the obtained samples are shown in Fig. 3. The XRD pattern for the high C_3N_4/Ta ratio (2: 1) shows peaks similar to at the results when the ratio of C_3N_4/Ta ratio (1: 1), which is ascribable to TaC formation. Contrastingly, at a low C_3N_4/Ta ratio (1: 2), two additional nitrides, $TaN0_{.8}$ (PDF 00-025-1279) and/or TaN (PDF 03-065-9405 or PDF 03-065-6783), which have hexagonal structure, were observed in addition to the TaC phase. Apparently, the C_3N_4 serves as a reactive template, and higher amounts of C_3N_4 lead to a carbide phase rather than to a nitride phase. This observation agrees well with the results obtained by Giordano et al. for the urea glass method,[33–35] who reported that increasing the urea to metal precursor ratio yielded a transition from a nitride to a carbide. In this manner, the syntheses of different phases from nitride to carbide were tunable while maintaining small particle sizes.

The XRD patterns of the samples synthesized under NH_3 by varying the starting precursor weight ratio at a constant temperature of 1023 K are shown in Fig. 4. Irrespective of the precursor ratio, the formation of a pure phase of Ta_3N_5 (PDF 01-069-5200) was observed, which has a monoclinic structure with a C2/m (12) space group. This result is consistent with previous reports, clearly demonstrating Ta_3N_5 nanoparticles.[37] The XRD patterns of the sample synthesized under argon at 1573 K with the weight ratio constant at 1: 1 reveals the formation of a pure phase of tantalum carbide, TaC (PDF 00- 035-0801). This result is

similar to what was obtained under nitrogen flow, confirming that nitrogen gas did not participate in the reaction at high temperatures.[25]

Elemental analyses (CHN)

Elemental analyses were performed to determine the concentrations of carbon and nitrogen in the synthesized samples. The results for the samples synthesized under a flow of N_2 at different temperatures from 1023 to 1573 K while maintaining the weight ratio of mpg-C_3N_4/$TaCl_5$ at 1: 1 are shown in Table 1. The table indicates that the carbon concentrations gradually increase from 3.7% to 10.5% with increasing reaction temperature. Contrastingly, the nitrogen concentration decreased from 4.8% to 0.9% with increasing reaction temperature. The nitrogen and carbon concentrations in stoichiometric TaN and TaC are 7.1% and 6.2%, respectively. These data suggests that as the reaction temperature increases, the samples have the tendency to form a carbide phase, which is consistent with the XRD results. From the MS results (Fig. 2), nitrogen was observed to be removed in the form of N_2 or C_2N_2. The low concentration of nitrogen in this sample (2%) may represent the possibility of a carbonitride phase formation. These results are consistent with the XRD patterns that indicate the formation of a Ta carbonitride phase (Fig. 3). At 1573 K, the nitrogen concentration further decreased to 0.9%, and the carbon concentration was as high as 10.5%. This carbon concentration exceeded the theoretical carbon stoichiometry in the tantalum carbide phase TaC (6.2%), suggesting the presence of excess carbon in a separate phase. Similarly, the elemental analyses results of the sample synthesized under argon at 1573 K confirmed the formation of a tantalum carbide phase when the nitrogen

concentration was 0.7%, thus implying that there was no inclusion of the nitrogen gas in the structure at high temperatures.

The elemental analyses data for the samples synthesized by varying the C_3N_4/Ta precursor weight ratio (2 : 1 and 1 : 2) under a flow of nitrogen while maintaining the temperature constant at 1573 K are also displayed in Table 1. The sample with the high C_3N_4/Ta ratio (2: 1) possesses high and low concentrations of C (7.3%) and N (0.8%), respectively, whereas the sample with the low C_3N_4/Ta ratio (1:2) possesses low and high concentrations of C (2.3%) and N (3.8%), respectively. These results indicate that the high C_3N_4/$TaCl_5$ ratio (2: 1) resulted in a carbide phase, while the low C_3N_4/$TaCl_5$ ratio (1: 2) resulted in more tantalum carbonitride and nitride phases, which were confirmed in the XRD results (Fig. 3). The elemental analyses for the samples synthesized under NH_3 flow with different Ta weight ratios (C_3N_4/$TaCl_5$ 1: 1, 2: 1, 1: 2) at 1023 K are compiled in Table 2. The results show that all of the samples consisted of high nitrogen concentrations, between 8.8 and 10.8%, with low carbon concentrations (<1%). The values are close to the stoichiometric values of Ta_3N_5 (N: 11.4%), consistent with the results obtained from XRD analyses. The low concentration of carbon confirms that the NH_3 gas reacts with the carbon in C_3N_4 or with its residue.

N_2 sorption

N_2 sorption measurements were performed to obtain the BET surface area of the synthesized samples. The results are also listed in Tables 1 and 2. The data showed that the surface area of the products decreased with increasing reaction temperature, most likely because at higher temperatures, the particles are more aggregated and the particle sizes are

increased, which is in agreement with the crystalline size trend calculated with the Scherrer equation from XRD data (Table 1). The highest surface area (107 m^2 g^{-1}) was observed for the sample that was synthesized at 1023 K. Notably, the observed high surface area of the sample synthesized at 1573 K with a TaC phase because of the presence of graphitized carbon, For the synthesis that occurred under NH_3 flow (Table 2), a surface area as high as ~30 m^2 g^{-1} was obtained for the Ta_3N_5 nanocrystal, which is consistent with the previous reports.[37]

X-ray photoelectron spectroscopy (XPS)

XPS measurements were performed to study the surface chemical composition and oxidation state. The Ta 4f, N 1s, and C 1s spectra are shown in Fig. 5 A, B and C, respectively. The XPS Synthesized at 1023 K showed the presence of two peaks at the following binding energies: 26.3 eV for Ta $4f_{7/2}$ and 28.2 eV for Ta $4f_{5/2}$, which were assigned to Ta^{5+} (most likely Ta_2O_5).[18,26] This surface oxide layer was likely formed during the passivation process that occurred in diluted O_2 before the samples were removed into ambient conditions. In Fig. 6 B for the N 1s and Ta $4p_{3/2}$ regions, the peaks were observed at 396.6, 400, and 404.5 eV, which correspond to a metal nitride (Ta–N),[18,26] the N–C groups in the remaining C_3N_4 fragment, and Ta^{5+} $4p_{3/2}$, respectively. In Fig. 6C, the C 1s tail in the range from 285–287 eV can be ascribed to a C–N species from the C_3N_4-originated residue.[15] Similarly, the XPS spectra of the sample synthesized at 1123 K indicated the presence of a Ta^{5+} surface with a C–N residue. The minor signal at ~24.0 eV in Ta $4f_{7/2}$ (Fig. 6A) corresponds to a Ta nitride (N–Ta).[18,26] which also corresponds with a N 1s peak at ~397 eV (Fig. 6B). These results are consistent with XRD data (Fig. 3), which

show a TaN nanocrystal in those samples that were synthesized at relatively low temperatures (1023 and 1123 K). From the XPS data, these TaN nanocrystal surfaces remained at the highest oxidation state of Ta (Ta^{5+}), which is most likely the result of an oxide passivation layer. When the synthesis temperature was increased to 1223 K, the XRD pattern indicated the formation of TaC and/or Ta_2CN (Fig. 3), and distinct signals of Ta $4f_{7/2}$ at 23.6 eV and Ta $4f_{5/2}$ at 25.5 eV were detected (Fig. 6A), all of which corresponded to a Ta carbide or nitride species.[18,26] Accordingly, a C 1s spectrum (Fig. 6C) clearly shows the characteristic peak of TaC at 283.0 eV as well as a N 1s shoulder peak at 396.8 eV, which indicates the presence of a metal carbonitride. The XPS signals of Ta $4f_{7/2}$ at 23.6 eV (Fig. 6A) and C 1s at 283.0 eV (Fig. 6C) became more prominent for the sample synthesized at 1323 K, which demonstrated that the carbide/carbonitride formation was also more prominent. For the sample synthesized at 1573 K, the peak of N 1s at 398.0 eV decreased in intensity, but the peak of C 1s at 283.0 eV remained clear. In addition, the peaks of Ta $4f_{7/2}$ at 23.6 eV and Ta $4f_{5/2}$ at 25.5 eV (Ta–C) became more predominant, while the peaks at 26.3 and 28.2 eV (Ta–O) decreased in intensity (Fig. 6A). All of these XPS results are also consistent with elemental analyses (Table 1), indicating that increasing temperatures lead to higher and lower carbon and nitrogen concentrations, respectively.

Transmission electron microscopy (TEM)

TEM was performed on the samples synthesized under a flow of nitrogen with a weight ratio of 1: 1 $C_3N_4/TaCl_5$ in a temperature range from 1023 to 1573 K. The TEM images and FFT patterns of the samples are shown in Fig. 6. The sample synthesized at 1023 K exhibited very fine spherical particles with a size of ~3 nm in the matrix of the

carbonaceous species, apparently utilizing the confinement effects of such small spacings. The corresponding FFT patterns revealed a weak ring of spots arising from the interatomic spacings of the crystalline nanoparticles (Fig. 7A) and confirmed a lack of crystallinity obtained from the XRD pattern (Fig. 3). The excess carbon and nitrogen concentrations determined by elemental analysis would have originated from a residue of the C_3N_4 template that was observed between the nanoparticles of the sample. Fig. 7B (1123 K) shows the formation of small spherical nanoparticles in the size range of 3–5 nm. The FFT pattern (Fig. 7B) shows three diffraction rings whose radii were measured to be 0.250, 0.216, and 0.155 nm, corresponding to the interatomic spacings of the TaC/N cubic structure crystal planes (111), (200), and (220), respectively; these results were consistent with the XRD patterns. Fig. 7C (1223 K) shows the formation of small nanoparticles in the size range of 10 nm. The carbonaceous residue observed from the low temperature synthesis was less prominent in the image. The FFT pattern showed three diffraction rings whose radii were measured to be 0.258, 0.225, and 0.159 nm, corresponding to the cubic crystal planes (111), (200), and (220), respectively. The samples synthesized at 1323 K and at 1573 K formed nanoparticles in the size range of 15 and 20 nm, respectively, suggesting the aggregation of the particles at the high reaction temperatures. The corresponding FFT pattern revealed more diffraction rings, which indicated an increase in the particle size and crystallinity of the sample in comparison with the samples synthesized at lower temperatures. FFT patterns showed three diffraction rings whose radii were measured to be 0.259, 0.223–0.227, and 0.156–0.158 nm, corresponding to the interatomic spacings represented by the TaC cubic structures (111), (200), and (220), respectively. Overall, the TEM images clearly indicate the successful formation of nanocrystals using the

confinement of the mpg- C_3N_4 reactive template. At lower temperatures, the carbon residue captures the Ta-nanoparticles and makes aggregates that are connected between the particles. Above 1223 K, the carbonaceous residue seems to disappear, most likely due to its involvement in the formation of carbide and concurrent particle aggregation.

Thermogravimetric analyses (TGA)

TGA analyses on the synthesized samples under an air flow with temperatures of ≤1273 K were performed to provide an estimate with regards to the composition of the synthesized material and to predict its thermal stability in air. While oxidation of the carbonaceous residue is expected to decrease the weight, oxidation of the nitride (TaN) and the carbide (TaC) species leads to an increase in weight with theoretical weight gain values of 13.3 and 14.5%, respectively. The TGA results are shown in Fig. 7. The obtained TGA curves of the samples showed three different trends in the following temperature ranges: 500–700, 700–950, and 950–1050 K. For the sample synthesized at 1023 K, the low temperature synthesis led to a gradual decrease in weight throughout, which was consistent with the fact that the large amount of carbonaceous residue from C_3N_4 remained in the sample. For the other samples (synthesis temperatures of 1123–1573 K), a weight increase was observed starting at 500 K; this weight increase was most likely due to nitride and carbide oxidation. A weight loss observed at 700–900 K corresponded to the decomposition of C_3N_4 or related template residue, which can be relatively easily removed at low temperatures. Therefore, reactions at the higher temperatures lead to a lower degree of weight loss in this range. For the sample synthesized at 1573 K where TaC formation is predominant, a clear weight increase was observed at ~900 K, suggesting this temperature

is required to oxidize the carbide. In a high temperature range, 950–1050 K, all of the samples decreased in weight, suggesting that the graphite or carburized residues are finally oxidized and combusted at these temperatures. Indicating to what degree what species remain is challenging; however, the TGA analyses confirmed a consistent trend of the crystal phases in the samples measured through other characterization methods (i.e., XRD, XPS, and elemental analysis).

Discussion regarding tantalum carbide and nitride syntheses

Overall, the syntheses of tantalum based nitride–carbide nanoparticles were achieved after tuning the temperature, the precursor ratio, and the gas atmosphere. C_3N_4 decomposition finishes at approximately 1050 K (MS in Fig. 2), but a significant amount of carbonaceous species remained depending on the initial C_3N_4 amount (TEM image, Fig. 7; elemental analyses, Table 1; TGA, Fig. 8). At relatively low reaction temperatures (≤1123 K), an ultrafine tantalum nitride phase (TaN) was formed (XRD; Fig. 3), while the original pore size of the mpg-C_3N_4 was maintained, as indicated by the crystalline size from the XRD data (Table 1) and the TEM image (Fig. 7), all of which strictly reflect the confinement of the hard template. The nanoparticles are surrounded with the residue of the template, as shown in the TEM image in Fig. 7. This remaining carbon does not react with the Ta precursors ≤~1200 K (XRD, Fig. 3; XPS, Fig. 6). Thus, TaN is the major phase obtained at the relatively lower temperatures. Depending upon the relative ratio between the C_3N_4 and the Ta precursor, the amount of the carbon remaining can be adjusted; increasing the presence of C_3N_4 generates a higher amount of carbon residue relative to the nitrogen residue (Table 1 and Fig. 4). The synthesized nano- TaN in turn reacts with the carbon

residue at high temperatures (~1223 K; carbo-thermal reduction), leading to formation of the nitride–carbide solid solution (Fig. 4). A lower carbon residue obtained with a lower C_3N_4/Ta ratio essentially leaves TaN due to the lack of reactive carbon remaining even in the high temperature synthesis (1573 K; Fig. 4). An extensive addition of carbon by a higher C_3N_4/Ta ratio instead leads to a more pure carbide form at higher temperatures (XRD, Fig. 4).

For the ammonia treatment, as evidenced by temperature programmed reaction via MS, the major decomposition product in gas phase was HCN (Fig. 2), and only a trace amount of carbon was detected by elemental analyses (Table 1). The product obtained at 1023 K was a Ta_3N_5 phase irrespective of the C_3N_4/Ta precursor ratio, suggesting that NH_3 reacts with C_3N_4 or the decomposed products. This reaction then renders lower reducing conditions during the synthesis than the carbo-reduction with solid carbon under an inert gas flow and is most likely the reason why the oxidation state of Ta^{5+} is maintained rather than Ta^{3+} (TaN) or an even more reduced state in the case of the carbides.

One of the benefits of this nanoparticle synthesis method is the ability to tune the particle size, depending on the pore size of mpg-C_3N_4 reactive template reflecting the starting SiO_2 nanoparticle size.[37] The limitation of the synthesis is also that the presence of the template is essential, potentially inhibiting the mass production of the nanoparticles. However, direct nanoparticle synthesis on a support, such as carbon, has been demonstrated starting from mpg-C_3N_4/carbon composite as a template,[38,39] so that there is tremendous scope for improvement of these materials for various applications. Research on synthesis of different metal nitride–carbides is ongoing.

Tantalum carbides and nitrides as electrocatalysts for HER

Different Ta phases from the nitrides to the carbides are expected to possess different activities for catalysis. For many catalytic applications, nanoparticle synthesis is essential to device performance by enhancing the number of catalytically active sites. Although bulk tantalum nitride and carbide materials were reported to possess relatively low activities for electrochemical HER (overpotentials of >0.4 V were reported),[14,40] Applying this synthetic approach to prepare nanoparticle not only introduced an increased number of active sites with these unique surface facets but also may have introduced a new electronic state, which perturbs d electron states and results in improved electrochemical activity. Thus, the synthesized Ta nanoparticles were tested for electrochemical HER by using a RDE at constant rotational speed of 1600 rpm. CV experiments were performed in 0.05 M H_2SO_4 at a scan rate of 5 mV s^{-1} between -0.5 and 0.3 V vs. an RHE. Fig. 8A shows the voltammograms for the samples synthesized at different temperatures under N_2. The reported current density was obtained using the geometrical surface area of the electrode (0.07 cm^2) with the same catalyst weight loading (0.5 mg cm^{-1}). The sample synthesized under N_2 at 1023 K exhibited a cathodic current with an onset potential of only -0.16 V vs. RHE, which clearly demonstrated the beneficial effects of the nanoparticle synthesis on the electrocatalytic activity. Then, as the current was decreased with increasing reaction temperature, the onset potential exhibited a negative shift. The HER current of the tantalum carbide TaC sample synthesized at 1573 K was observed at a relatively high potential at -0.26 V vs. RHE. Thus, the sample synthesized under nitrogen at 1023 K exhibited the highest HER catalytic performance among all of the samples prepared in this study, with a HER overpotential below 200 mV. The higher current density observed for the sample

might be attributed to the high surface area as confirmed through BET analyses (Table 1). As the reaction temperature was increased, the HER current decreased due to decreasing sample surface area, which would accordingly reduce the number of active sites available on the surface for hydrogen evolution. Notably, all of the catalysts were very stable when subjected to hundreds of cycles as long as the investigated potential range was used. Similarly, a carbonaceous residue that is in contact with the nanoparticles, as observed in the TEM images (Fig. 7), may function as an electronic bridge to improve electronic conductivity. The beneficial effects of the carbon residue was also argued in the literature for tungsten carbide nanoparticles synthesized in a similar manner.[15]

Unfortunately, a phase change from a nitride phase to a carbide phase happened concurrently with the loss of surface area, and the effects of the active surface phase for HER apart from the surface area effects were difficult to surmise. The major phase of the active catalyst synthesized at 1023 K was TaN with its surface oxidized (Fig. 6), which is known to possess a low activity for HER.[14] However, when the ultrafine nanoparticles were formed, an electrocatalytic function was observable even with the oxide formation.[41,42] In such a short distance (~1 to 2 nm), electron tunneling may occur from the conductive substrate to the catalyst surface,[43] and thus, non-conductive materials can start functioning as electrocatalysts. Nanoparticles are thus expected to play a significant role in the field of electrocatalysis, and tremendous scope for non-noble metal materials to improve their electrocatalytic performance by designing nanomaterials exists.

The well-known reaction steps of HER in acidic solutions are the following:[44]

1. Discharge reaction of a proton to form an adsorbed hydrogen atom (Volmer reaction).

$$M + H_3O^+ + e^- \rightleftharpoons MH_{ads} + H_2O \qquad (1)$$

2. Combination of an adsorbed hydrogen atom with a proton and an electron to form molecular hydrogen (Heyrovsky reaction).

$$MH_{ads} + H_3O^+ + e^- \rightleftarrows H_2 + M + H_2O \quad (2)$$

3. Combination of two adsorbed hydrogen atoms to form molecular hydrogen (Tafel reaction).

$$MH_{ads} + MH_{ads} \rightleftarrows H_2 + 2M \quad (3)$$

In the equations, M denotes an active site of the catalyst, and MH_{ads} donates a hydrogen atom adsorbed at that site. HER starts with the proton discharge step (Volmer reaction, (1)) and follows either the electrodesorption step (Heyrovsky reaction, (2)) or the proton recombination step (Tafel reaction, (3)).[44] The HER mechanism can be studied through analyzing the Tafel plot obtained from the polarization curves. The Tafel slope (b) is an inherent property of the catalyst and is determined by the rate-limiting step of HER. The empirical values of the Tafel slopes extracted from the Tafel plot can provide insights into the probable mechanisms for HER in the catalytic surface. In acid solutions, if the Volmer reaction (1) is the rate-determining step or the rates of (1) and (2) are comparable, a high slope value at room temperature is obtained (≈120 mV dec^{-1}) while a Volmer–Heyrovsky mechanism (2) will return a slope close to 40 mV dec^{-1}.[45,46] The Pt (110) surface is one of the most active catalysts for HER and that under acidic conditions its mechanism is known to proceed through the Volmer–Tafel reaction exhibiting a slope close to 30 mV dec^{-1}.[9,44] The recombination step is the rate-determining step at a low overpotential, which is consistent with the strong Pt–H bond. At relatively high overpotentials, the Tafel slopes (Fig. 9B) obtained from the polarization curves of the tantalum carbide and nitride samples

were in the range of 103–158 mV dec^{-1} irrespective of the obtained crystal phases. These high Tafel slopes are consistent with the Volmer reaction (1) as the rate-determining step, suggesting that the surface coverage of the hydrogen species is low and that the hydrogen is relatively weakly adsorbed at steady-state kinetics.[9,44] Further studies can be made possible by tuning this metal–hydrogen bond, which is a descriptor for the activity correlation for HER.[5]

Conclusions

Different ultrafine nanocrystals of TaCN with various C/N ratios were synthesized with a size range from 3 to 20 nm using confined pores of a mpg-C_3N_4 template. The nitride form was first obtained at relatively low temperatures (≥1123 K), which in turn reacts with the carbonaceous residue originating from C_3N_4 template to form a carbide phase at higher temperatures. Tantalum carbide was more preferably produced than nitride when the weight ratio of the C_3N_4 template was richer, confirming the role of mpg-C_3N_4 as a carbon source (when it is in excess). Two forms of tantalum nitride, namely TaN and Ta_3N_5, were selectively formed under N_2 and NH_3 flow, respectively.

Electrochemical measurements demonstrated that the sample synthesized under N_2 at 1023 K exhibited the highest and most stable HER current in acidic media among the samples prepared in this study. This result can be attributed to the very small particle size (~3 nm on average) and the high surface area, which was confirmed by BET analysis (107 m^2 g^{-1}). As the reaction temperature increased, the HER current decreased due to particle aggregation, which accordingly reduced the surface area of the exposed active sites for hydrogen adsorption. This study clearly shows that the tantalum nitride–carbide

nanocrystals serve as excellent and stable electrocatalysts for HER even in highly acidic media. Furthermore, tremendous scope for further improvement through enhancing the dispersion of the materials or through introducing hetero-atoms exists.

References

(1) W. Kreater and H. Hofmann, Int. J. Hydrogen Energy, **1998**, 23, 661.

(2) J. A. Turner, Science, **2004**, 305, 972.

(3) N. S. Lewis and D. Nocera, Proc. Natl. Acad. Sci. U. S. A., **2006**,103, 15729.

(4) S. Trasatti, J. Electroanal. Chem., **1972**, 39, 163.

(5) J. Greeley, T. F. Jaramillo, J. Bonde, I. Chorkendorff and J. K. Nørskov, Nat. Mater., **2006**, 5, 909.

(6) E. Santos and W. Schmickler, ChemPhysChem, **2006**, 7, 2282.

(7) E. Santos and W. Schmickler, Chem. Phys., **2007**, 332, 39.

(8) J. K. Nørskov, T. Bligaard, J. Rossmeisl and C. H. Christensen, Nat. Chem., **2009**, 1, 37.

(9) R. Subbaraman, D. Tripkovic, D. Strmcnik, K.-C. Chang, M. Uchimura, A. P. Paulikas, V. Stamenkovic and N. M. Markovic, Science, **2011**, 334, 1256.

(10) R. Subbaraman, D. Tripkovic, K.-C. Chang, D. Strmcnik, A. P. Paulikas, P. Hirunsit, M. Chan, J. Greeley,V. Stamenkovic and N.M. Markovic, Nat. Mater., **2012**, 11, 550.

(11) T. F. Jaramillo, K. P. Jørgensen, J. Bonde, J. H. Nielsen, S. Horch and I. Chorkendorff, Science, **2007**, 317, 100.

(12) M. A. Lukowski, A. S. Daniel, F. Meng, A. Forticaux, L. Li and S. Jin, J. Am. Chem. Soc., **2013**, 135, 10274.

(13) D. Voiry, H. Yamaguchi, J. Li, R. Silva, D. C. B. Alves, T. Fujita, M. Chen, T. Asefa, V. B. Shenoy, G. Eda and M. Chhowalla, Nat. Mater., **2013**, 12, 850.

(14) S. Wirth, F. Harnisch, M. Weinmann and U. Schr¨oder, Appl. Catal., B, **2012**, 126, 225.

(15) A. T. Garcia-Esparza, D. Cha, Y. Ou, J. Kubota, K. Domen and K. Takanabe, ChemSusChem, **2013**, 6, 168.

(16) W.-F. Chen, C.-H. Wang, K. Sasaki, N. Marinkovic, W. Xu, J. T. Muckerman, Y. Zhu and R. R. Adzic, Energy Environ. Sci., **2013**, 6, 943.

(17) R. Ohnishi, K. Takanabe, M. Katayama, J. Kubota and K. Domen, J. Phys. Chem. C, **2013**, 117, 496.

(18) L. Johansson, Surf. Sci. Rep., **1995**, 21, 177.

(19) Y. Liu, T. G. Kelly, J. G. Chen and W. E. Mustain, ACS Catal., **2013**, 3, 1184.

(20) R. B. Levy and M. Boudart, Science, **1973**, 181, 547.

(21) Y.-H. Chang, J.-B. Wu, P.-J. Chang and H.-T. Chiu, J. Mater. Chem., **2003**, 13, 365.

(22) O. Y. Khyzhun and V. A. Kolyagin, J. Electron Spectrosc. Relat. Phenom., **2004**, 137, 463.

(23) L. Shi, Z. Yang, L. Chen and Y. Qian, Solid State Commun., **2005**, 133, 117.

(24) C. L. Yeh and E. W. Liu, Ceram. Int., **2006**, 32, 653.

(25) J. M. C´ordoba, M. J. Sayagu´es, M. D. Alcal´a and F. J. Gotor, J. Am. Ceram. Soc., **2007**, 90, 381.

(26) J. K. Schaeffer, C. Capasso, R. Gregory, D. Gilmer, L. R. C. Fonseca, M. Raymond, C. Happ, M. Kottke, S. B. Samavedam, P. J. Tobin and B. E. White, J. Appl. Phys., **2007**, 101, 014503.

(27) M. Lei, H. Z. Zhao, H. Yang, B. Song and W. H. Tang, J. Eur. Ceram. Soc., **2008**, 28, 1671.

(28) J. Polonsk´y, I. M. Petrushina, E. Christensen, K. Bouzek, C. Prag, J. E. T. Andersen and N. J. Bjerrum, Int. J. Hydrogen Energy, **2012**, 37, 2173.

(29) A. Fischer, M. Antonietti and A. Thomas, Adv. Mater., **2007**, 19, 264.

(30) A. Fischer, J. O. M¨uller, M. Antonietti and A. Thomas, ACS Nano, **2008**, 2, 2489.

(31) A. Thomas, F. Goettmann and M. Antonietti, Chem. Mater., **2008**, 20, 738.

(32) Y.-S. Jun, W. H. Hong, M. Antonietti and A. Thomas, Adv. Mater., **2009**, 21, 4270.

(33) C. Giordano, C. Erpen, W.-T. Yao and M. Antonietti, Nano Lett., **2008**, 12, 4659.

(34) C. Giordano, C. Erpen, W.-T. Yao, B. Milke and M. Antonietti, Chem. Mater., **2009**, 21, 5136.

(35) C. Giordano and M. Antonietti, Nano Today, **2011**, 6, 366.

(36) M. Groenewolt and M. Antonietti, Adv. Mater., **2005**, 17, 1789.

(37) Y. Fukasawa, K. Takanabe, A. Shimojima, M. Antonietti, K. Domen and T. Okubo, Chem.–Asian J., **2011**, 6, 103.

(38) J. Chen, K. Takanabe, R. Ohnishi, D. Lu, S. Okada, H. Hatasawa, H. Morioka, M. Antonietti, J. Kubota and K. Domen, Chem. Commun., **2010**, 46, 7492.

(39) S. Isogai, R. Ohnishi, M. Katayama, J. Kubota, D. Y. Kim, S. Noda, D. Cha, K. Takanabe and K. Domen, Chem.–Asian J., **2012**, 7, 286.

(40) A. C. C. Tseung and B. S. Hobbs, Platinum Met. Rev., **1969**, 13, 146.

(41) J. Seo, D. Cha, K. Takanabe, J. Kubota and K. Domen, Chem. Commun., **2012**, 48, 9074.

(42) J. Seo, L. Zhao, D. Cha, K. Takanabe, M. Katayama, J. Kubota and K. Domen, J. Phys. Chem. C, **2013**, 117, 11635.

(43) A. J. Bard and L. R. Faulkner, in Electrochemical Methods: Fundamentals and applications, Wiley, New York, **2001**.

(44) B. E. Conway and B. V. Tilak, Electrochim. Acta, **2002**, 47, 3571.

(45) J. G. N. Thomas, Trans. Faraday Soc., **1961**, 57, 1603.

(46) J. Bockris, I. A. Ammar and K. M. S. Hug, J. Phys. Chem., **1957**, 61(7), 879.

List of figures

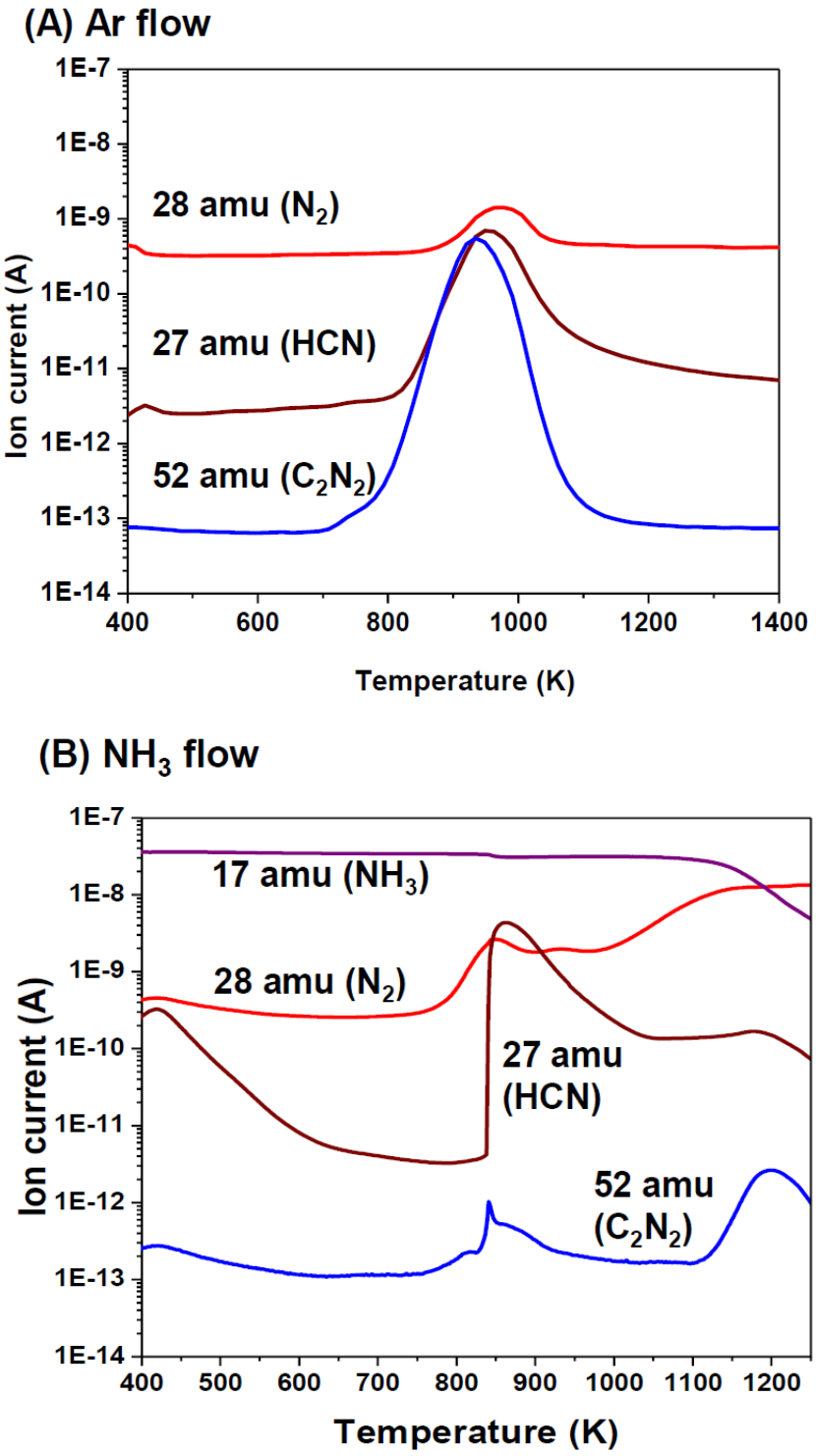

Fig. 1 Mass signals obtained during the nanoparticle synthesis under (A) Ar and (B) NH_3.

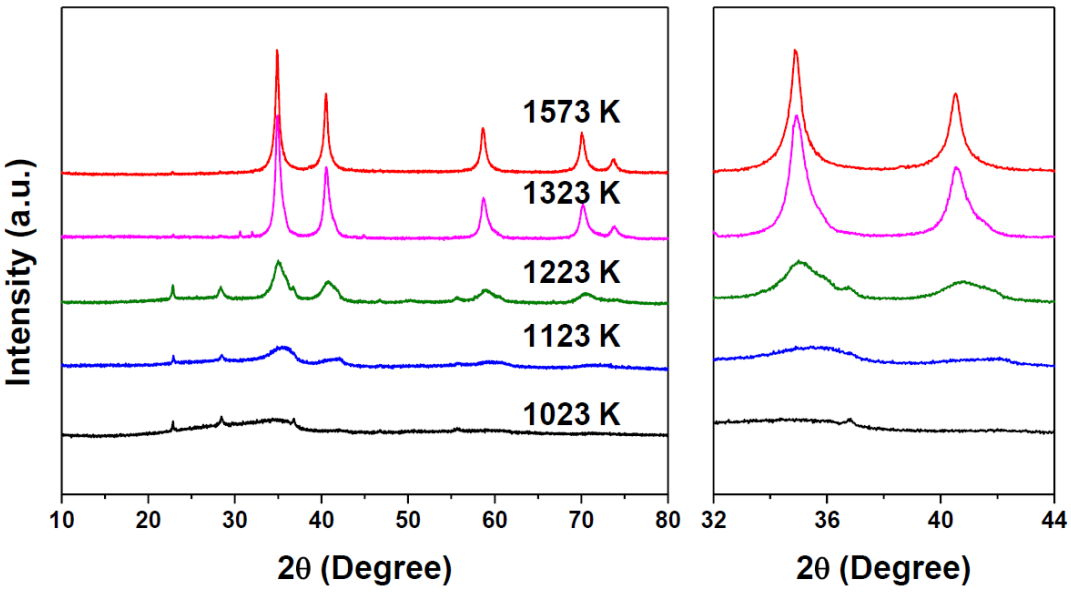

Fig. 2 The effects of reaction temperature on the XRD patterns of the tantalum based products synthesized under N_2 flow.

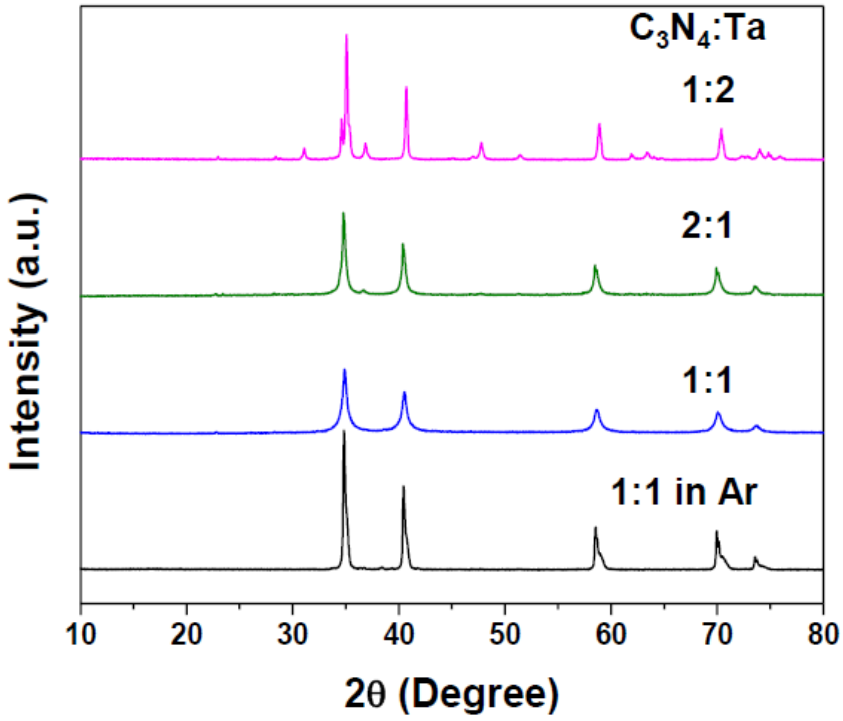

Fig. 3 The effects of the differences in the tantalum-to-carbon nitride weight ratio on the XRD patterns of the tantalum-based products synthesized at 1573 K under N_2 or Ar flow.

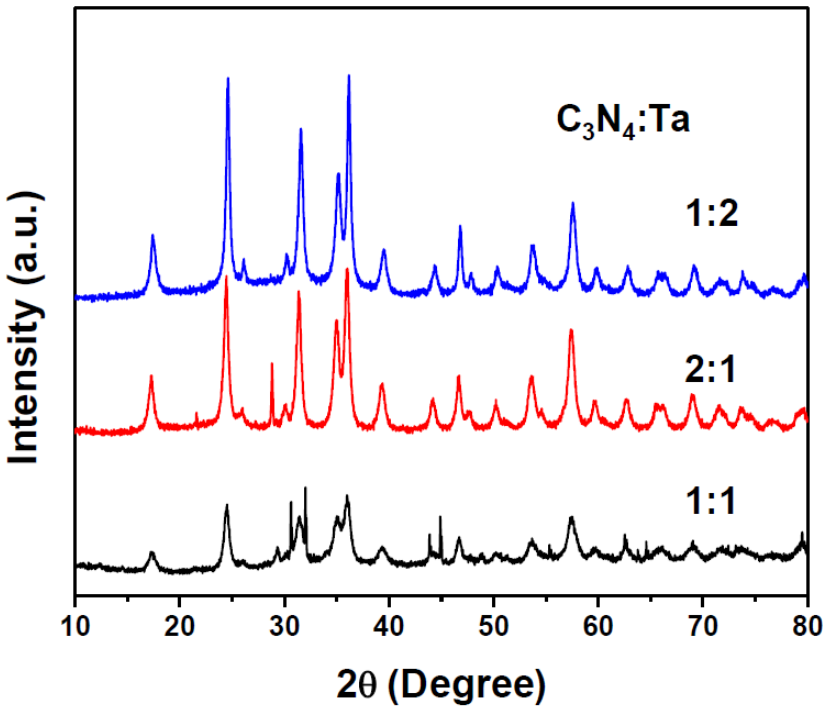

Fig. 4 The effects of the differences in the tantalum-to-carbon nitride weight ratio on the XRD patterns of the tantalum-based products synthesized at 1023 K under NH_3 flow.

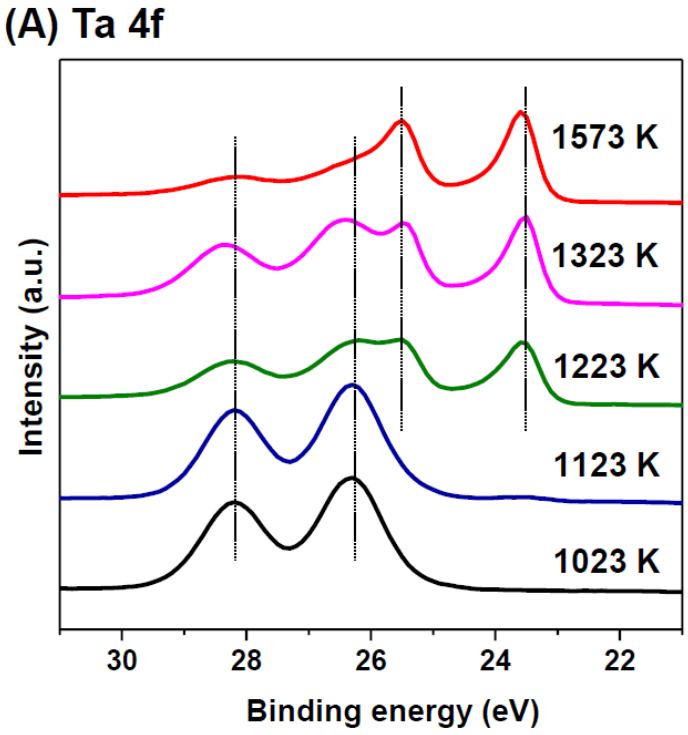

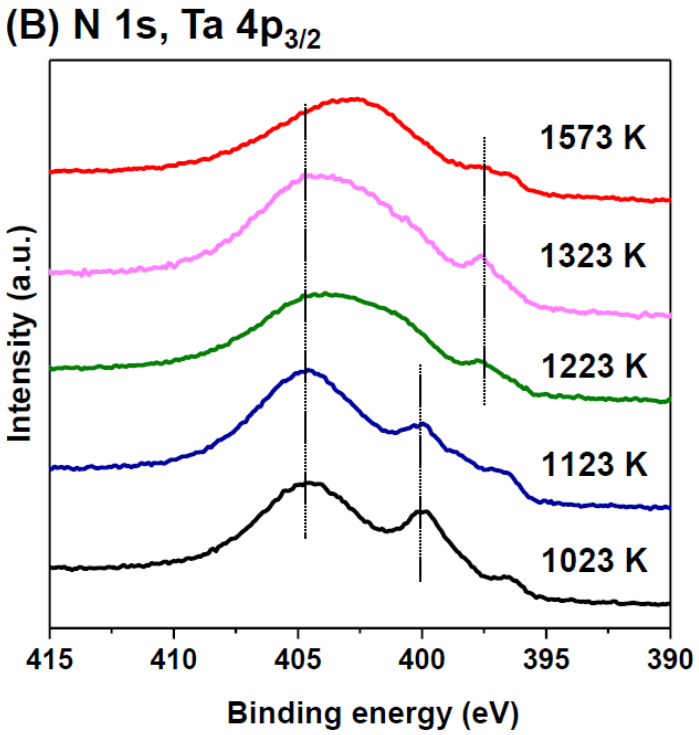

Fig. 5 XPS spectra for (A) Ta 4f (B) N 1s, Ta $4p_{3/2}$, and (C) C 1s of the tantalum based products obtained at different temperatures under N_2 flow.

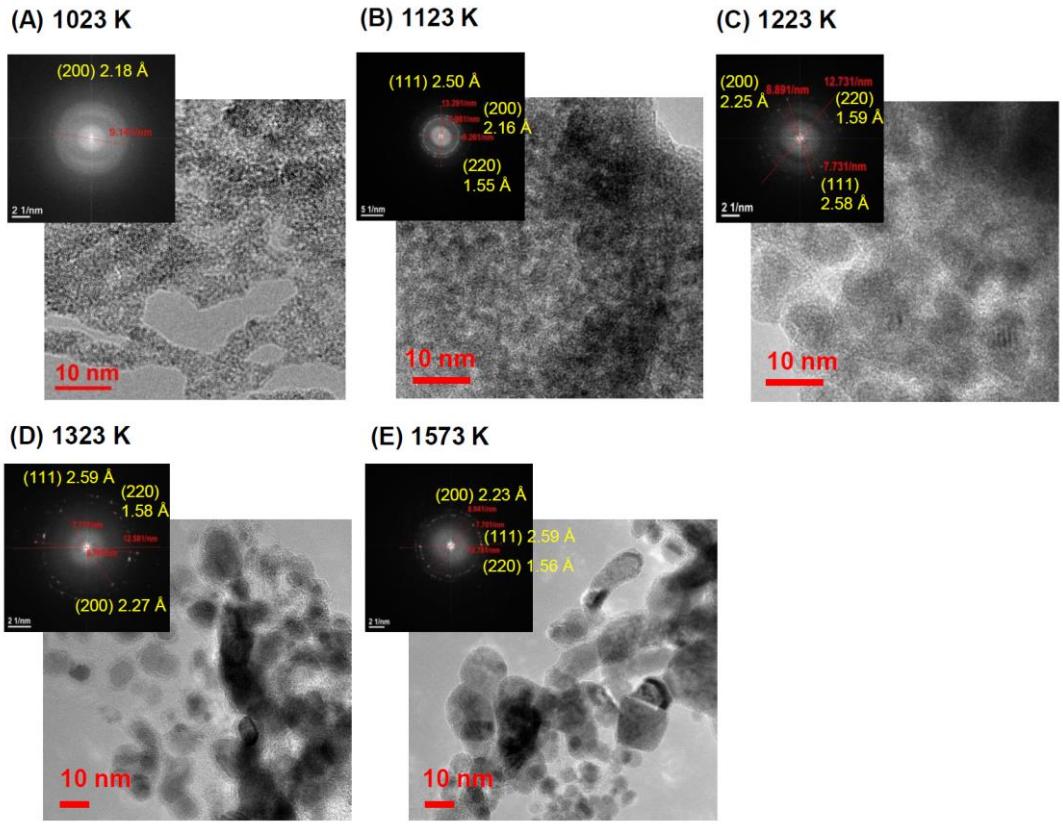

Fig. 6 TEM micrographs of the Ta-based products synthesized at different temperatures.

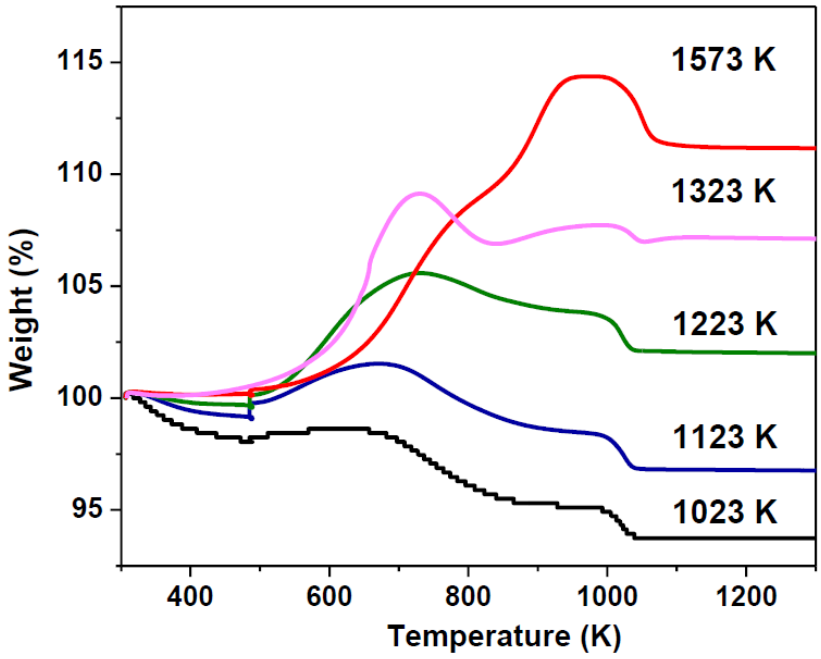

Fig. 7 TGA of the tantalum-based products synthesized at different temperatures under air flow.

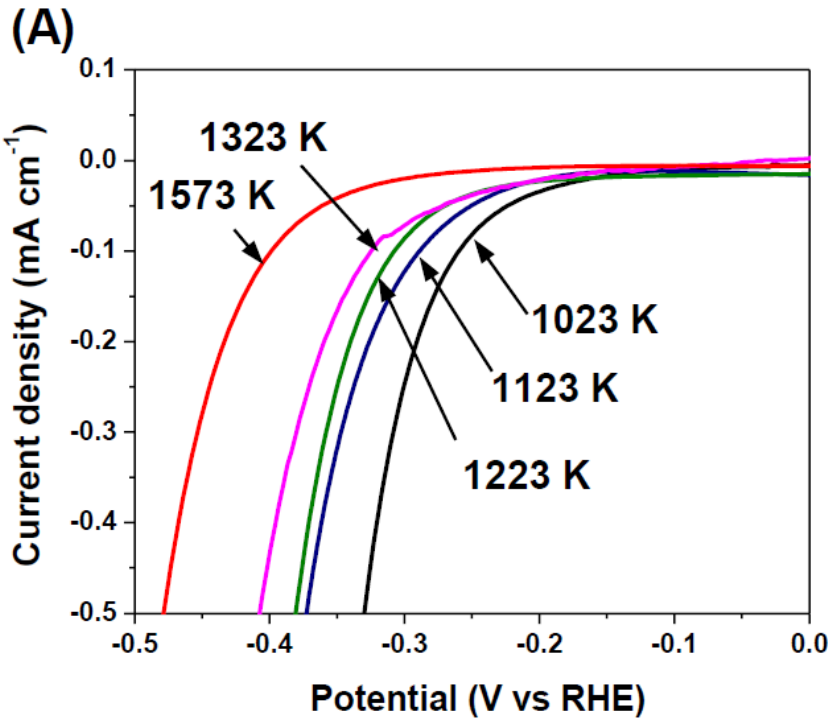

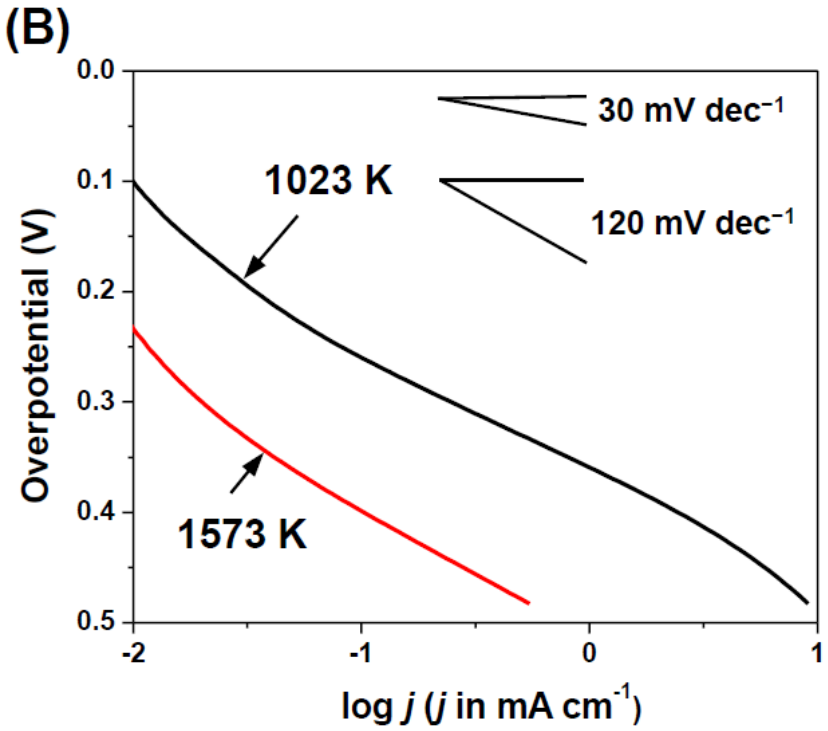

Fig. 8 (A) HER voltammograms of tantalum-based samples synthesized at different temperatures under N_2 flow. (B) HER Tafel plots for the tantalum-based samples synthesized at 1023 K and at 1573 K (0.05 M H_2SO_4 aq., in Ar, 1600 rpm, 5 mV s^{-1}, 298 K).

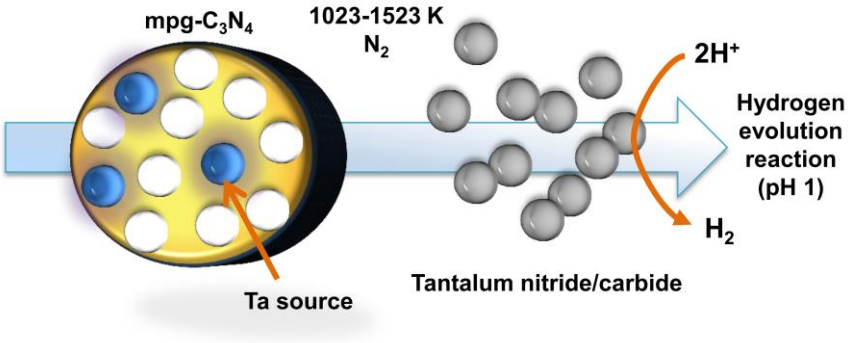

List of tables

Precursor weight ratio mpg-C_3N_4 : $TaCl_5$	Temperature (K) under N_2 flow	C (%)	N (%)	Crystalline size (nm)	BET surface area (m^2/g)	Phase
1:1	1023	3.7	4.8	-	107	(TaN)
1:1	1123	4.6	4.5	5	85	TaN
1:1	1223	4.8	3.0	6	81	Ta_2CN, TaC
1:1	1323	6.4	2.0	14	32	TaC
1:1	1573	10.5	0.9	19	99	TaC
2:1	1573	7.3	0.8	26	18	TaC
1:2	1573	2.4	3.8	33	1	Ta_2CN, TaN, TaC

Table 1 Elemental analyses, reaction temperatures, phase assignments from the XRD diffractograms, crystallite size evaluations from the Scherrer equation, and BET surface areas for the tantalum-based products obtained at various temperatures and precursor mpg-C_3N_4/$TaCl_5$ weight ratios under N_2 flow.

Precursor weight ratio mpg-C_3N_4 : $TaCl_5$	Temperature (K) under NH_3 flow	C (%)	N (%)	Crystalline size (nm)	BET surface area (m^2/g)	Phase
1:1	1023	0.09	9.1	16	29	Ta_3N_5
2:1	1023	0.91	10.8	18	2.3	Ta_3N_5
1:2	1023	0.15	8.8	20	34	Ta_3N_5

Table 2 Elemental analyses, reaction temperatures, phase assignments from the XRD diffractograms, crystallite size evaluations from the Scherrer equation, and BET surface areas for the tantalum-based products obtained t various temperatures and precursor mpg-C_3N_4/$TaCl_5$ weight ratios under NH_3 flow.

CHAPTER 4

Molybdenum carbide–carbon nanocomposites synthesized from a reactive template for electrochemical hydrogen evolution

Molybdenum carbide nanocrystals (Mo_2C) with sizes ranging from 3 to 20 nm were synthesized within a carbon matrix starting from a mesoporous graphitic carbon nitride (mpg-C_3N_4) template with confined pores. A molybdenum carbide phase (Mo_2C) with a hexagonal structure was formed using a novel synthetic method involving the reaction of a molybdenum precursor with the carbon residue originating from C_3N_4 under nitrogen at various temperatures. The synthesized nanocomposites were characterized using powder X-ray diffraction (XRD), temperature-programmed reaction with mass spectroscopy (MS), CHN elemental analyses, thermogravimetric analyses (TGA), nitrogen sorption, X-ray photoelectron spectroscopy (XPS), and transmission electron microscopy (TEM). The results indicated that the synthesized samples have different surface structures and compositions, which are accordingly expected to exhibit different electrocatalytic activities toward the hydrogen evolution reaction (HER). Electrochemical measurements demonstrated that the sample synthesized at 1323 K exhibited the highest and most stable HER current in acidic media, with an onset potential of -100 mV vs. RHE, among the samples prepared in this study. This result is attributed to the sufficiently small particle size (~8 nm on average) and accordingly high surface area (308 m^2 g^{-1}), with less oxidized surface entrapped within the graphitized carbon matrix.

Introduction

Hydrogen is considered a clean energy carrier and a promising candidate for the replacement of petroleum fuels.[1,2] Currently, most hydrogen for industrial purposes is produced from the steam reforming of natural gas or methane, which generates carbon dioxide as an undesired by-product.[3] The development of alternative technologies for the production of clean energy from renewable resources remains a challenge. The electrolysis of water is achieved by a system associated with a sustainable and greenhouse-gas-free source to generate hydrogen, with the required electricity being derived from renewable energy sources such as sunlight, wind, or geothermal energy.[4–6] During water electrolysis, the hydrogen evolution reaction (HER) occurs, which requires an effective catalyst to reduce the overpotential and consequently increase the efficiency of the reaction. To date, the electrocatalytic HER depends on the use of noble metals, such as Pt, as active and stable electrocatalysts. However, Pt is an expensive metal and suffers from a global supply shortage.[7–14] Many attempts have been made to develop non-noble-metal cathode materials which are required to be active and stable enough to replace the Pt-group metals under extreme conditions. Among them, a tremendous amount of attention has been given to d^0 metal sulfides, such as WS, [15] Mo_2S, [15–17] and metal carbides, such as WC,[18] TaC,[7] and Mo_2C.[19,20] Group VI transition-metal carbides are proved to be stable under a wide range of electrocatalytic operating conditions.[19–22] These compounds exhibit good corrosion resistance, high stability, high melting points, and high mechanical strength.[21] The experimental and theoretical investigations have been performed to elucidate the electronic structure of metal carbides.[23,24] The hybridization occurs between the metal d orbitals and the carbon s- and p-orbitals and resulted in an expansion in the d-band structure of the

metal, approaching the d-band of Pt.[3,23,24] Thus, group-VI transition-metal carbides possess catalytic properties similar to those of the Pt-group metals, which makes them promising candidates to replace the noble metals in hydrogen-generation catalysts, especially in electrocatalysts.[3,19,20] Antonietti and coworkers,[25–31] and other studies[7,18,32–34] demonstrated the use of the reactive template (mpg-C_3N_4) and urea-glass method to synthesize various metal nitride and carbide nanomaterials. In this method, carbon nitride or urea precursor not only provides confined space for nanoparticle formation, but also chemical sources of nitrogen and carbon. A novel synthetic approach was reported to prepare high-surface-area tantalum nitride/carbide and tungsten carbide utilizing mesoporous graphitic carbon nitride (mpg-C_3N_4) as a reactive template under various conditions.[7,18] The obtained nanomaterials exhibited tremendous improvements in stability and electrocatalytic activity for the HER in acidic media.[7,18] Thus, this synthetic approach to form nanocarbide crystals presents an opportunity to prepare additional transition-metal carbides and to utilize them in various applications, particularly the electrochemical HER. It has been known that molybdenum carbides are active in various catalytic reactions, especially carbon conversion and hydrogenolysis-type reactions.[21] As for the HER, the electrocatalytic activity of commercial Mo_2C has been investigated and several reports have demonstrated how the use of microparticles would result in low activity.[19,20] Very recently, Chen et al. reported the highly active Mo_2C/carbon nanotube (CNT) composites prepared by a relatively simple carburization process. The obtained Mo_2C/CNT exhibited a HER cathodic current with an overpotential of 63 mV at 1 mA cm^{-2}, showing the promise of the material as an HER electrocatalyst.[20] In this study, a novel nanocomposite of molybdenum carbide and carbon was designed via the reaction of a molybdenum precursor with mpg-

C_3N_4 at various temperatures under flowing nitrogen. The confinement of mesopores to within a few nanometers was utilized to restrict the size of the molybdenum species, which are surrounded by carbon originating from C_3N_4 decomposition. This system enables direct utilization of the molybdenum species as electrocatalysts. The obtained molybdenum carbide–carbon nanocomposites exhibited a stable and remarkable improvement in their electrocatalytic performance towards the HER in acidic media compared with the performance of previously reported bulk materials.

Experimental

Synthesis of the molybdenum carbide–carbon nanocomposite

The molybdenum-based nanocomposite was prepared using the reactive hard-templating method. The synthetic procedure was performed while the ratio of mpg-C_3N_4/$MoCl_5$ was maintained at 1: 1. First, a dark-green solution was prepared from molybdenum chloride (0.5 g; $MoCl_5$; ≥99.9% Aldrich) dissolved in ethanol (0.5 ml), as described in eqn (1).[35]

$$MoCl_5 + 2C_2H_5OH \longrightarrow MoCl_3(OC_2H_5)_2 + 2HCl \quad (1)$$

The pores of the reactive template (0.5 g) were subsequently immersed in the aforementioned solution. The final mixture was placed in an alumina boat crucible and heated to a temperature in the range of 1023 to 1573 K under a 100 ml min^{-1} flow of N_2. At the end of the synthetic procedure, a passivation process was performed by flowing a mixture of 1% O_2 in He at 100 ml min^{-1} at room temperature. Caution is required when using this procedure because the thermal decomposition of C_3N_4 causes the formation of hydrogen cyanide and cyanogen gases.

Characterization

The synthesized samples were characterized using elemental analyses (C, H, and N), X-ray diffraction (XRD), N_2 sorption, thermogravimetric analyses (TGA), X-ray photoelectron spectroscopy (XPS), a temperature-programmed reaction with mass spectroscopy (MS), and transmission electron microscopy (TEM). Elemental analyses were performed using a Flash 2000 Thermo Scientific CHNS/O analyzer. The XRD patterns of the products were collected on a Bruker DMAX 2500 X-ray diffractometer equipped with a Cu Kα radiation source (λ=0.154 nm). The N_2 sorption studies were conducted using a Micrometrics ASAP 2420 to determine the Brunauer–Emmett–Teller (BET) surface area, the Barrett–Joyner–Halenda (BJH) pore size, and the pore volume. The formation mechanism of molybdenum carbide was investigated by detecting the products in the gas phase during nanoparticle synthesis using an OMNI Star (GSD320 O1) portable mass spectrometer equipped with a tungsten filament from Pfeiffer Vacuum. The mass spectrometer was connected at the furnace outlet to study the decomposition products under N_2 flow of 100 ml min^{-1}. A Mettler- Toledo TGA/DSC1 Star system was utilized to carry out TGA under a 100 ml min^{-1} flow of air. XPS studies were carried out using a Kratos Axis Ultra DLD spectrometer equipped with a monochromatic Al Kα X-ray source (hν=1486.6 eV) operating at 150 W, a multi-channel plate and a delay line detector under 1.0 $x10^{-9}$ Torr vacuum. The survey and high-resolution spectra were collected at fixed analyzer pass energies of 160 and 20 eV, respectively. A transmission electron microscope of model TITAN G2 80-300 ST was used to characterize the sample morphology and to determine the particle size. The microscope was operated at an electron beam energy of

300 keV. Selected area electron diffraction (SAED) patterns were obtained to determine the inter-planar d-spacings of the crystalline phases present in the samples.

Electrochemical measurements

The electrocatalytic activities of the samples toward the HER were studied using a rotating disk electrode (RDE). The working electrode was first prepared using the following procedure First, 2 mg of molybdenum-based nanocomposite was dispersed in 169 ml of ethanol and sonicated for 30 min. Then, 56.3 ml of Nafion solution was added to the mixture, and the final solution was sonicated for 30 min. Next, 2 ml of the suspension was drop-coated onto a glassy carbon electrode (GCE) with a geometric surface area of 0.071 cm^2 to provide a weight density of 0.25 mg cm^{-2}. Finally, the electrode was placed in an oven and heated at 373 K under air for 1 h.

The electrocatalytic measurements were conducted using a research-grade potentiostat system (VMP3) from BioLogic Science Instruments. The electrochemical cell used in this study was a three-electrode cell. An Ag/AgCl electrode saturated in KCl was used as a reference electrode. The counter electrode was a carbon rod and all the electrodes were immersed in the same electrolyte solution (0.05MH_2SO_4; Fisher Chemical, trace metal grade). Cyclic voltammetry (CV) experiments were performed at a scan rate of 5 mV s^{-1} from -0.60 to 0.39 V vs. a reversible hydrogen electrode (RHE) for hydrogen evolution while maintaining a constant rotational speed of 1600 rpm. Electrochemical impedance spectroscopy (EIS) was performed for Mo_2C (commercial) and Mo_2C synthesized at 1323 K in acid solution (0.05 M H_2SO_4) from 1000 kHz to 100 mHz at different HER overpotentials (300, 400 and 500 mV).

Results and discussion

Temperature-programmed reaction of Mo–C_3N_4 investigated by mass spectroscopy

The reaction pathway of the reactive template C_3N_4 with Mo precursor was investigated by detecting the formed products in the gas phase during the synthesis. The MS signals were collected under a flow of inert Ar (100 ml min^{-1}) from 318 to 1573 K at a heating rate of 28 K min^{-1}. The signals for 17, 27, 28, 44, and 52 amu were detected between 600 and 1000 K and were assigned to NH_3, HCN, N_2, CO_2, and C_2N_2, respectively. The spectra of the major four components observed—HCN, N_2, CO_2 and C_2N_2 are shown in Fig. 1. The peak maxima were drastically shifted to lower temperatures of approximately 875 K in the case of samples prepared with a molybdenum source, whereas the peak maxima of samples without a molybdenum species were at 965 K. This suggests that a reaction occurred between mpg-C_3N_4 and the molybdenum precursor [$MoCl_3(OC_2H_5)_2$]. The formation of HCN, N_2, and C_2N_2 was consistent with the decomposition product from mpg-C_3N_4;[36] however, the HCN signal was intensified. An increase in the nitrogen signal was also observed, which should indicate the presence of excess carbon as shown in eqn (2) (small z). As a result, molybdenum–carbon composites are formed, and a further temperature increase may lead to molybdenum reacting with the excess carbon. The precursor and the remaining solvent likely contained more hydrogen, which improved the formation of the hydrogen-containing gaseous species (HCN and trace NH_3). Likewise, the oxygen-containing product (CO_2), which was detected in the low-temperature region, should originate from the precursor. When eqn (2) is unbalanced to release more nitrogen-containing gases, a carbon residue should be formed as a solid; substantial amounts of carbon residue were, in fact, observed, as will be discussed later.

X-ray diffraction (XRD)

The produced nanocomposites were characterized by XRD to determine their crystal structure. The XRD patterns are presented in Fig. 2 for the samples synthesized under flowing nitrogen at various temperatures from 1023 to 1573 K. The crystallite sizes obtained using the Scherrer equation are listed in Table 1. The XRD pattern for the sample synthesized at 1023 K contains no apparent diffraction peaks, which can be interpreted as the samples consisting of either ultrafine particles or an amorphous phase. In the case of the samples synthesized between 1123 and 1573 K, the XRD patterns contain eight major peaks at 2θ = 34.4, 38, 39,4, 52.2, 61.7, 69.5, 74.5, and 75.3°, which are indexed to (100), (002), (101), (102), (110), (103), and (112) planes of hexagonal Mo_2C (PDF-00-001-1188) or (PDF-00- 035-0787). This finding confirms that molybdenum carbide was solely formed even at 1123 K, unlike the nitride formation observed in the case of other metals, such as Ti, Nb, and Ta.[7] The peaks become sharper with increasing synthesis temperature, most likely because of the particle aggregation prevalent at high temperatures. A new shoulder peak appears in the XRD pattern of the sample prepared at 1573 K, consistent with the formation of orthorhombic Mo_2C (PDF-01-071-0242) in addition to the observed hexagonal structure.

Elemental analyses (CHN)

Elemental analyses were performed to determine the elemental compositions of carbon and nitrogen in the synthesized samples. The results shown in Table 1 indicate that the nitrogen content was very low, even at 1023 K, which confirms that nitrogen was almost completely gasified at temperatures below 1023 K, as indicated by the MS signals (Fig. 2). The carbon

content slightly increased from 21% to 24% with increasing reaction temperature. The carbon content exceeded the theoretical stoichiometry in the molybdenum carbide phase Mo_2C (6%), which suggests the presence of excess carbon in a separate phase that is either amorphous or graphitized. This result confirms that molybdenum carbide nanocrystals are present in the carbon matrix which accordingly form the nanocomposite structure that affects the electrocatalytic activity as discussed in the electrochemical measurements section.

Transmission electron microscopy (TEM)

TEM observations were performed on the samples synthesized at temperatures from 1023 to 1573 K. The TEM images and SAED patterns of the samples are presented in Fig. 3. The sample synthesized at 1023 K (Fig. 4A) contained very fine spherical particles with a size of ~2–5 nm in the matrix of the carbonaceous species, apparently utilizing the confinement effects of such small spacings (Fig. 1C). The corresponding SAED pattern reveals three diffraction rings with radii of 0.243, 0.209, and 0.147 nm; these radii correspond to the interatomic spacings of the (002), (102), and (110) planes of the hexagonal Mo_2C crystal structure, respectively. Excess carbon that originated from a residue of the C_3N_4 template was observed between the nanoparticles of the sample. As shown in Fig. 4B, the sample synthesized at 1123 K contains small spherical nanoparticles in the 4–10 nm size range. The SAED pattern reveals three diffraction rings with radii of 0.179, 0.149, and 0.126 nm; these radii correspond to the interatomic spacings of the (102), (110), and (112) planes of the Mo_2C hexagonal crystal structure, respectively. These results are consistent with the XRD patterns presented in Fig. 3. The TEM image in Fig. 4C (1223

K) shows the formation of small nanoparticles in the 6–15 nm size range. The carbonaceous residue resulting from the low-temperature synthesis is less prominent in this image, which indicates that the reaction of the carbon residue with the Mo precursor was enhanced at higher temperatures. The SAED pattern contained three diffraction rings with radii of 0.256, 0.231, and 0.127 nm; these radii correspond to the (100), (101), and (112) crystal planes, respectively, of the hexagonal Mo_2C structure. In the case of the TEM image of the sample prepared at 1323 K (Fig. 4D), the size of the nanoparticles ranges from 8 to 25 nm. The carbonaceous residue observed at lower temperatures was almost entirely consumed during the formation of carbide nanoparticles at 1323 K. The corresponding SAED pattern revealed additional diffraction rings, which indicated an increase in the particle size and crystallinity of the sample compared with those of the samples synthesized at lower temperatures. The corresponding SAED pattern reveals three strong rings with radii of 0.241, 0.263, and 0.234 nm; these radii correspond to the (002), (100), and (101) crystal planes, respectively, of the hexagonal Mo_2C structure. In addition, a 1 nm crystalline layer with a d-spacing of 0.35 nm was observed around the Mo_2C nanoparticles. The obtained d-spacing corresponds to the interatomic spacings of graphitized carbon.[37] The sample synthesized at 1573 K (Fig. 4E) contained nanoparticles in the size range of 15–35 nm, which suggests that the nanoparticles aggregated. The corresponding SAED pattern also revealed additional diffraction rings with radii of 0.260, 0.153, and 0.131 nm; these radii correspond to the interatomic spacings represented by the (100), (110), and (112) planes, respectively, of the hexagonal Mo_2C structure. Similarly, the Mo_2C nanoparticles were surrounded by a thicker layer (2 nm) of graphitized carbon.

Overall, the TEM images clearly show the successful formation of nanocrystals using the confinement of the mpg-C_3N_4 reactive template. The amount of carbon residue involved in the formation of Mo_2C nanoparticles gradually decreased with increasing temperature until being completely consumed and aggregated at 1573 K. The size of the nanoparticles at different temperatures exhibits a bimodal distribution. The first distribution begins at a size of ~2 nm at 1023 K, followed by a gradual increase in the size. The number of such produced nanoparticles appeared to increase when the reaction temperature was increased to 1573 K. This result should correlate with the creation of graphitic carbon, which protects the particles from growing. For the second distribution, the obtained nanoparticles at 1023 K are larger than ~5 nm. As the reaction temperature was increased, the size increased to 35 nm at 1573 K because of particle aggregation. Essentially, such aggregation leads to a decrease in the number of active surface sites with increasing reaction temperature. This result suggests that some of the Mo_2C nanoparticles aggregate beyond the confined size of the mpg-C_3N_4 pores. At temperatures greater than 1223 K, the carbon residue clearly graphitized, as observed in the layered structure surrounding the Mo_2C nanoparticles in the TEM images; the thickness of this structure increased with increasing temperature. The graphitized carbon on the surface might affect the electrocatalytic activity of Mo_2C toward the HER.

N_2 sorption

N_2 sorption measurements were performed to determine the BET surface area of the synthesized samples. The results are listed in Table 1 and demonstrate that the surface area of the products increased from 120 to 308 $m^2\ g^{-1}$ with increasing reaction temperature.

Apparently, the graphitized carbon residue greatly contributes to the surface area. The obtained high surface area of the produced Mo_2C nanoparticles would significantly enhance the catalytic performance by providing abundant catalytic sites.

According to the MS and TEM results, C_3N_4 decomposed below 1050 K and the remaining carbon originating from the decomposition reacted with the molybdenum precursor to produce Mo_2C nanoparticles. The increase in surface area with increasing reaction temperature resulted from an increase in the production of Mo_2C nanoparticles and porous graphite. The porosity formation was maximized at 1323 K in this case, giving the highest surface area (308 cm^2 g^{-1}). When the reaction temperature was increased further to 1573 K, the produced Mo_2C nanoparticles combined and aggregated, which caused a sudden decrease in the surface area.

X-ray photoelectron spectroscopy (XPS)

XPS measurements were performed to study the surface chemical compositions and oxidation states of the samples. The Mo 3d, O 1s, and C 1s spectra are presented in Fig. 4. The Mo 3d XPS spectra (Fig. 5A) of the samples synthesized from 1023 to 1323 K contained two peaks that decreased in intensity with increasing reaction temperature. These peaks were observed at the following binding energies: 235.6 and 232.5 eV for Mo $3d_{3/2}$ and Mo $3d_{5/2}$, which were assigned to Mo^{6+} (MoO_3).[38,39] An additional peak at 228.7 eV for Mo $3d_{5/2}$ was observed for the sample synthesized at 1023 K and was assigned to Mo^{4+} (MoO_2).[40] Mo^{4+} state may also indicates the presence of molybdenum oxycarbide phase. For the samples synthesized at 1123, 1223, and 13231323 K. The produced Mo_2C nanoparticles then combined and aggregated at 1573 K, the Mo $3d_{5/2}$ signal observed at

228.1 eV increased in intensity with increasing reaction temperature.[41] This peak became prominent and shifted to 228.0 eV at 1573 K, which confirms the formation of Mo_2C.[39,41] In addition to this peak, a Mo $3d_{3/2}$ signal was observed at 231.3 eV in the spectrum of the sample prepared at 1573 K; this signal was close to 231.1 eV characteristic value of Mo_2C.[42] The O 1s spectrum (Fig. 5B) for samples prepared at temperatures from 1023 to 1323 K contained a characteristic signal at 530.4 that was assigned to O^{2-} in MoO_3; the intensity of this signal decreased with increasing reaction temperature.[39] The C 1s XPS spectra (Fig. 5C) contained a characteristic peak attributed to graphite at 284.4 eV.[43] This peak became sharper with increasing reaction temperature, indicating that the concentration of graphitized carbon increased with increasing reaction temperature. According to the XPS results, an oxide layer formed on all the samples but decreased in intensity with increasing reaction temperature until almost disappearing at 1573 K. This oxide layer resulted from the passivation process that occurred at the end of the synthetic procedure when the samples were exposed to ambient air after being removed from the furnace at room temperature. The C 1s XPS spectrum indicates the formation of crystalline layers of graphitized carbon that increased in concentration with increasing reaction temperature. This result is consistent with the elemental analysis, XRD, and TEM results. Thus, not only the carbide species but also the oxide layers on the surface (as an insulator) play a key role in determining the electrocatalytic activities of the materials toward the HER, as will be discussed later.

Thermogravimetric analyses (TGA)

TGA of the synthesized samples under flowing air up to 1273 K were performed to provide an estimate of the composition of the synthesized material and to predict its thermal stability in air. Whereas oxidation of the carbonaceous residue is expected to decrease the weight of the samples, the oxidation of the molybdenum carbide species leads to an increase in weight. The TGA results are shown in Fig. 5. For samples synthesized at temperatures less than 1323 K, a slight weight loss below 500 K was detected, which indicates that the samples might adsorb a small amount of water on their surface. However, an obvious weight loss occurred in the temperature range of approximately 620 to 720 K, which was attributed to oxidation of the carbonaceous residue from the C_3N_4 remaining in the samples. The decrease in weight continued to 800 K in the case of the sample synthesized at 1023 K, which was due to the presence of a large amount of carbon residue. The samples then oxidized and remained stable up to 1050 K. For the samples synthesized at high temperatures, i.e., at 1323 and 1573 K, a small weight loss was observed between 600 and 700 K, which is attributed to the decomposition of a small amount of carbonaceous residue.

When the heating exceeded 720 K, the Mo_2C samples began to oxidize to molybdenum trioxide and carbon dioxide. The weight gain was almost constant up to 1050 K, where a sudden decrease that indicated the complete evaporation of molybdenum trioxide was detected. The TGA results suggest that complex oxidation of the materials occurred for carbon and molybdenum species. At 1323 K, a larger amount of carbide phase is proven to exist as observed at weight increase above 800 K.

Discussion regarding molybdenum carbide–carbon nanocomposite syntheses

Overall, molybdenum carbide nanoparticles with sizes ranging from 2 to 50 nm that were surrounded by a graphitic carbon matrix were synthesized by the reaction of a C_3N_4 template with a molybdenum precursor under flowing nitrogen at various temperatures from 1023 to 1573 K. The smaller size of the obtained Mo_2C (~2 nm) at 1023 K compared with the pore size of mpg-C_3N_4 (~6 nm) implies that crystal growth occurred before the complete decomposition of the mpg-C_3N_4 framework.

The mass spectroscopy results (Fig. 2) confirmed the gasification of nitrogen present in the carbon nitride template and that molybdenum carbide formed through the reaction of the molybdenum precursor with the carbon residue originating from the decomposition of C_3N_4. The TEM images (Fig. 4) confirm that the size distribution of the nanoparticles produced at various temperatures is bimodal; i.e., (1) only a gradual increase in the size (~2–15 nm) that coincides with an increase in the number of produced nanoparticles was observed and (2) the nanoparticles extensively aggregated to form particles approximately 50 nm in size. These findings result from the reaction of the molybdenum precursor with the carbon residue originating from C_3N_4 inhibiting or facilitating the aggregation with increasing reaction temperatures (i.e., the carbo-thermal reduction process). The observed increase in the surface area with increasing reaction temperature resulted from the production of graphitized carbon in conjunction with an increase in the number of Mo_2C nanoparticles with increasing temperature as explained in the first model in the TEM section.

The amount of carbon residue involved in the formation of Mo_2C nanoparticles gradually decreased with increasing reaction temperature until being completely consumed at 1323

K. Then the produced Mo_2C nanoparticles subsequently combined and aggregated when the temperature increased further to 1573 K, which caused a sudden decrease in the surface area. At low temperatures, the unreacted carbonaceous residue captured the Mo_2C nanoparticles and formed aggregates that were connected between the particles. At temperatures above 1223 K, the carbon residue graphitized and formed layers surrounding the Mo_2C nanoparticles, which increased in thickness at 1573 K.

Because of the small size of the produced Mo_2C nanoparticles (~2–15 nm), their surfaces became easily oxidized after they were exposed to ambient air. The XPS results (Fig. 5) suggest that the oxide layer decreases with increasing reaction temperature. This result occurs because, at low temperatures, the size of the produced Mo_2C nanoparticles is smaller and they are unstable compared with the particles obtained at high temperatures. At 1573 K, almost no oxide was observed due to the large particle size of Mo_2C, which enhanced its stability and inhibited oxidation.

Molybdenum carbide–carbon nanocomposite as electrocatalysts for the HER

Nanoparticle synthesis is essential for improving the HER performance by increasing the number of catalytically active sites. It is known that molybdenum carbide nanoparticles exhibit good electrocatalytic activity toward the HER. The applied synthesis method of molybdenum carbide nanoparticles not only obtained an increased number of active sites with unique surface facets but also introduced graphitized carbon surrounded Mo_2C nanoparticles which enhanced the conductivity of the nanocomposites and accordingly improved their electrocatalytic activity for the HER. Molybdenum-based nanocomposites synthesized at various temperatures and commercial Mo_2C were tested for the

electrochemical HER using an RDE at a constant rotational speed of 1600 rpm. CV experiments were performed in 0.05 M H_2SO_4 at a scan rate of 5 mV s^{-1} between -0.6 and 0.39 V vs. RHE. The catalytic activity of carbide materials is known to depend on their surface structure and composition. The XPS data (Fig. 5) indicate that the surface of the obtained Mo_2C nanoparticles at different temperatures forms MoO_3 layers and that the extent of these oxide layers decreases at high temperatures. Thus, the nanocomposite materials prepared at different temperatures are expected to possess different electrocatalytic activities. Fig. 6A presents the voltammograms for the molybdenum based nanocomposites synthesized at various temperatures and commercial Mo_2C. The reported current density was obtained using a geometrical surface area of an electrode (0.07 cm^2) with the same catalyst weight loading (0.25 mg cm^{-2}). The HER cathodic current increased as the reaction temperature was increased from 1023 to 1323 K because of the decreased extent of oxide layers observed on the surface with increasing synthesis temperature. In addition, the surface area increased with increasing reaction temperature, which would increase the number of active sites available on the surface for hydrogen evolution. Molybdenum-based nanocomposites synthesized at 1323 K exhibited the highest HER cathodic current among the samples prepared in this study, with an onset potential of only -100 mV vs. RHE, similar to the reported values for Mo_2C based materials.[19,20] This highest current density is attributed to the sample's small particle size and accordingly high BET surface area (308 m^2 g^{-1}), which would increase the number of active sites available on the surface for proton adsorption. The presence of 1 nm of graphitized carbon surrounding Mo_2C improved the conductivity and accordingly electron transfer. The extent of oxide layers (as an insulator) observed on the surface of the sample decreased compared with that

observed for other samples. Unfortunately, when the reaction temperature was increased to 1573 K, the HER current of Mo_2C decreased and occurred at a higher potential of -0.15 V vs. RHE because of the sudden decrease in the surface area due to particle aggregation. Beneficial effects of nano-sizing are obvious from the result of commercial Mo_2C, the particle size of which is large (>100 nm). The stability was tested using Mo_2C synthesized at 1323 K at a constant potential of -0.18 V vs. RHE (Fig. 6B). The result indicates that the catalytic current decreased to 60% after 3 h and then became stable for 25 h. The slight decrease of the HER activity using an Mo_2C catalyst is consistent with the literature[19,20] and the stability of the active species remains the issue to be solved. The differences in electrocatalytic activities were further elucidated between Mo_2C (commercial) and Mo_2C synthesized at 1323 K by electrochemical impedance spectroscopy (EIS) analysis. The result is displayed as a Nyquist plot where x- and y-axes are the real and negative imaginary parts of impedance, respectively. The charge transfer resistances for the samples were determined from the semicircle recorded at different overpotentials. Overall, the charge transfer resistances for both samples decreased as the overpotential increased (Fig. 6D). The smaller value of impedance for Mo_2C prepared at 1323 K than for commercial Mo_2C is due to the small particle size (~8 nm) that improves the minimized distance to the surface. Also, the graphitized carbon layer with a thickness of about 1 nm around the nanoparticles may function as an electronic bridge which will accordingly enhance the electronic conductivity and improve electron transfer reaction at the surface of the electrode.

The well-known HER mechanism under acidic solutions includes the following steps:[44]

(1) Discharge of a proton to form an adsorbed hydrogen atom (Volmer reaction):

$$M + H_3O^+ + e^- \rightleftharpoons MH_{ads} + H_2O \qquad (3)$$

(2) Combination of an adsorbed hydrogen atom with a proton and an electron to form molecular hydrogen (Heyrovsky reaction):

$$MH_{ads} + H_3O^+ + e^- \rightleftarrows H_2 + M + H_2O \quad (4)$$

(3) Combination of two adsorbed hydrogen atoms to form molecular hydrogen (Tafel reaction):

$$MH_{ads} + MH_{ads} \rightleftarrows H_2 + 2M \quad (5)$$

In eqn (3)–(5), M denotes an active site of the catalyst and MH_{ads} denotes a hydrogen atom adsorbed at that site. The HER starts with the proton discharge step (Volmer reaction, eqn (3)) and is followed by either the electrodesorption step (Heyrovskyreaction, eqn (4)) or the proton recombination step (Tafel reaction, eqn (5)).[44]

The HER mechanism can be studied through the analysis of the Tafel plots obtained from polarization curves. The Tafel slope (b) is an inherent property of a catalyst and is determined by the rate-limiting step of the HER. The empirical values of the Tafel slopes extracted from the Tafel plot can provide insight into the probable mechanisms for the HER on the catalytic surface. In acidic solutions, if the Volmer reaction (3) is the rate determining step or if the rates of (3) and (4) are comparable, a high slope value at room temperature is obtained (≈120 mV dec^{-1}). In contrast, a Volmer–Heyrovsky mechanism (4) will return a slope of approximately 40 mV dec^{-1}.[45,46] The Tafel slope of approximately 30 mV dec^{-1} is known to involve the Volmer– Tafel reaction.[13,44] Tafel slopes (Fig. 7C) obtained from the polarization curves from 0.2 to 0.25 V of the molybdenum-based nanocomposites were in the range of 110–235 mV dec^{-1}. These high Tafel slopes are consistent with the Volmer reaction (3) being the rate-determining step and suggest that

the surface coverage of the hydrogen species is low and that hydrogen is relatively weakly adsorbed with steady-state kinetics.[13,44]

Conclusions

Molybdenum carbide–carbon nanocomposites were successfully prepared through the reaction of the molybdenum precursor with the carbon residue originating from C_3N_4 decomposition under nitrogen at various temperatures. The obtained nanocomposites show that the samples have different surface structures and compositions and are accordingly expected to exhibit different electrocatalytic activities toward the HER. Electrochemical measurements demonstrated that the sample synthesized at 1323 K exhibited the highest and most stable HER current in acidic media among the samples prepared in this study. This result is attributed to the combination of the sample's small particle size (~8 nm on average) and its accordingly high surface area, which was confirmed by the BET analysis (308 m2 g^{-1}), as well as to the graphitized carbon layer on its surface. When the reaction temperature was further increased to 1573 K, the HER current decreased due to particle aggregation, which consequently reduced the surface area of the exposed active sites for hydrogen adsorption. This study clearly demonstrates that the molybdenum carbide–carbon nanocomposites serve as excellent electrocatalysts for the HER, even in highly acidic media. The electrocatalytic performance would be further improved through removing the oxide layers from the surface, enhancement of the dispersion of the nanocrystals in the carbon matrix and via the introduction of hetero-atoms.

References

(1) E. Navarro-Flores, Z. Chong and S. Omanovic, J. Mol. Catal. A: Chem., **2005**, 226, 179.

(2) M. S. Dresselhaus and I. L. Thomas, Nature, **2001**, 414, 332.

(3) W.-F. Chen, J. T. Muckerman and E. Fujita, Chem. Commun., **2013**, 49, 8896.

(4) W. Kreater and H. Hofmann, Int. J. Hydrogen Energy, **1998**, 23(661), 3.

(5) J. A. Turner, Science, **2004**, 305, 972.

(6) N. S. Lewis and D. Nocera, Proc. Natl. Acad. Sci. U. S. A., **2006**, 103, 15729.

(7) N. S. Alhajri, H. Yoshida, D. A. Anjum, A. T. Garcia-Esparza, J. Kubota, K. Domen and K. Takanabe, J. Mater. Chem. A, **2013**, 1, 12606.

(8) S. Trasatti, J. Electroanal. Chem. Interfacial Electrochem., **1972**, 39, 163.

(9) J. Greeley, T. F. Jaramillo, J. Bonde, I. Chorkendorff and J. K. Nørskov, Nat. Mater., **2006**, 5, 909.

(10) E. Santos and W. Schmickler, ChemPhysChem, **2006**, 7, 2282.

(11) E. Santos and W. Schmickler, Chem. Phys., **2007**, 332, 39.

(12) J. K. Nørskov, T. Bligaard, J. Rossmeisl and C. H. Christensen, Nat. Chem., **2009**, 1, 37.

(13) R. Subbaraman, D. Tripkovic, D. Strmcnik, K.-C. Chang, M. Uchimura, A. P. Paulikas, V. Stamenkovic and N. M. Markovic, Science, **2011**, 334, 1256.

(14) R. Subbaraman, D. Tripkovic, K.-C. Chang, D. Strmcnik, A. P. Paulikas, P. Hirunsit, M. Chan, J. Greeley, V. Stamenkovic and N.M.Markovic, Nat. Mater., **2012**, 11, 550.

(15) T. Y. Chen, Y. H. Chang, C. L. Hsu, K. H. Wei, C. Y. Chiang and L. J. Li, Int. J. Hydrogen Energy, **2013**, 28, 12302.

(16) T. F. Jaramillo, K. P. Jørgensen, J. Bonde, J. H. Nielsen, S. Horch and I. Chorkendorff, Science, **2007**, 317, 100.

(17) M. A. Lukowski, A. S. Daniel, F. Meng, A. Forticaux, L. Li and S. Jin, J. Am. Chem. Soc., **2013**, 135, 10274.

(18) A. T. Garcia-Esparza, D. Cha, Y. Ou, J. Kubota, K. Domen and K. Takanabe, ChemSusChem, **2013**, 6, 168.

(19) L. Liao, S. Wang, J. Xiao, X. Bian, Y. Zhang, M. D. Scanlon, X. Hu, Y. Tang, B. Liu and H. H. Girault, Energy Environ. Sci., **2014**, 7, 387.

(20) W.-F. Chen, C.-H. Wang, K. Sasaki, N. Marinkovic, W. Xu, J. T. Muckerman, Y. Zhu and R. R. Adzic, Energy Environ. Sci., **2013**, 6, 943.

(21) L. Johansson, Surf. Sci. Rep., **1995**, 21, 177.

(22) Y. Liu, T. G. Kelly, J. G. Chen and W. E. Mustain, ACS Catal., 2013, 3, 1184. 23 J. R. Kitchin, J. K. Nørskov, M. A. Barteau and J. G. G. Chen, Catal. Today, **2005**, 105, 66.

(23) J. R. Kitchin, J. K. Nørskov, M. A. Barteau and J. G. G. Chen, Catal. Today, **2005**, 105, 66.

(24) J. G. Chen, Chem. Rev., **1996**, 96, 1477.

(25) A. Fischer, M. Antonietti and A. Thomas, Adv. Mater., **2007**, 19, 264.

(26) A. Fischer, J. O. M¨uller, M. Antonietti and A. Thomas, ACS Nano, **2008**, 2, 2489.

(27) A. Thomas, F. Goettmann and M. Antonietti, Chem. Mater., **2008**, 20, 738.

(28) Y.-S. Jun, W. H. Hong, M. Antonietti and A. Thomas, Adv. Mater., **2009**, 21, 4270.

(29) C. Giordano, C. Erpen, W.-T. Yao and M. Antonietti, Nano Lett., **2008**, 12, 4659.

(30) C. Giordano, C. Erpen, W.-T. Yao, B. Milke and M. Antonietti, Chem. Mater., **2009**, 21, 5136.

(31) C. Giordano and M. Antonietti, Nano Today, **2011**, 6, 366.

(32) R. Ohnishi, K. Takanabe, M. Katayama, J. Kubota and K. Domen, J. Phys. Chem. C, **2013**, 117, 496.

(33) Y. Fukasawa, K. Takanabe, A. Shimojima, M. Antonietti, K. Domen and T. Okubo, Chem. –Asian J., **2011**, 6, 103.

(34) L. Yuliati, J.-H. Yang, X. Wang, K. Maeda, T. Takata, M. Antonietti and K. Domen, J. Mater. Chem., **2010**, 20, 4295.

(35) G. Raj, Adv. Inorg. Chem., Krishna Prakashan Media Ltd., India, 12th edn, **2010**, vol. 2.

(36) M. Groenewolt and M. Antonietti, Adv. Mater., **2005**, 17, 1789.

(37) R. Wang, J. Yang, K. Shi, B. Wang, L. Wang, G. Tian, B. Bateer, C. Tian, P. Shen and H. Fu, RSC Adv., **2013**, 3, 4771.

(38) C. Diaz, V. Lavayen and C. Dwyer, J. Solid State Chem., **2010**, 183, 1595.

(39) W. Lisowski, A. H. J. van den Berg, L. J. Hanekamp and A. van Silfhout, Surf. Interface Anal., **1992**, 19, 93.

(40) F. Werfeli and E. Minni, J. Phys. C: Solid State Phys., **1983**, 16, 6091.

(41) T. Clair, S. Oyama, D. Cox, S. Otani, Y. Ishizawa, R. Lo, K. Fukui and Y. Iwasawa, Surf. Sci., **1999**, 426, 187.

(42) E. G. Derouane, V. Parmon, F. Lemos and F. Ribeiro (Sustainable strategies for the upgrading of natural gas, fundamental challenges and opportunities), July, **2003**.

(43) W. Chen, H. Xu, L. Liu, X. Gao, D. Qi, G. Peng, S. Tan, Y. Feng, K. Loh and A. Wee, Surf. Sci., **2005**, 596, 176.

(44) B. E. Conway and B. V. Tilak, Electrochim. Acta, **2002**, 47, 3571.

(45) J. G. N. Thomas, Trans. Faraday Soc., **1961**, 57, 1603.

(46) J. Bockris, I. A. Ammar and K. M. S. Hug, J. Phys. Chem., **1957**, 61, 879.

List of figures

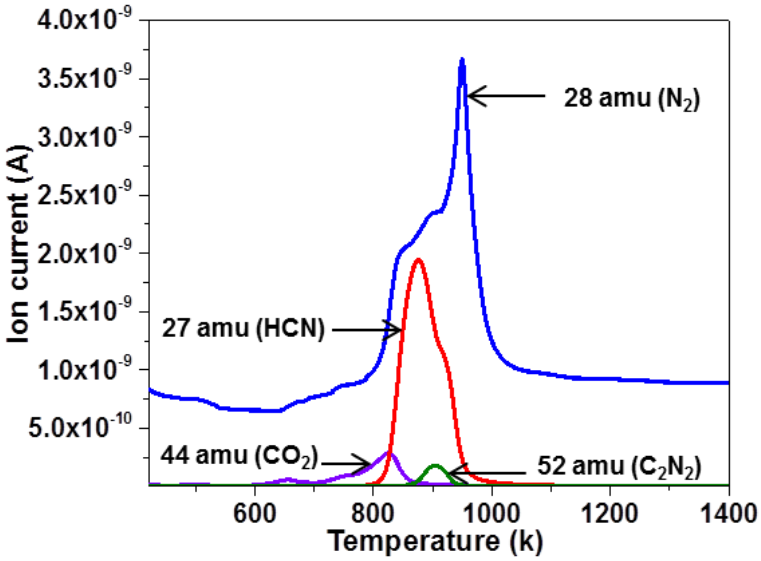

Fig. 1 MS signals obtained during the nanocomposite synthesis under Ar.

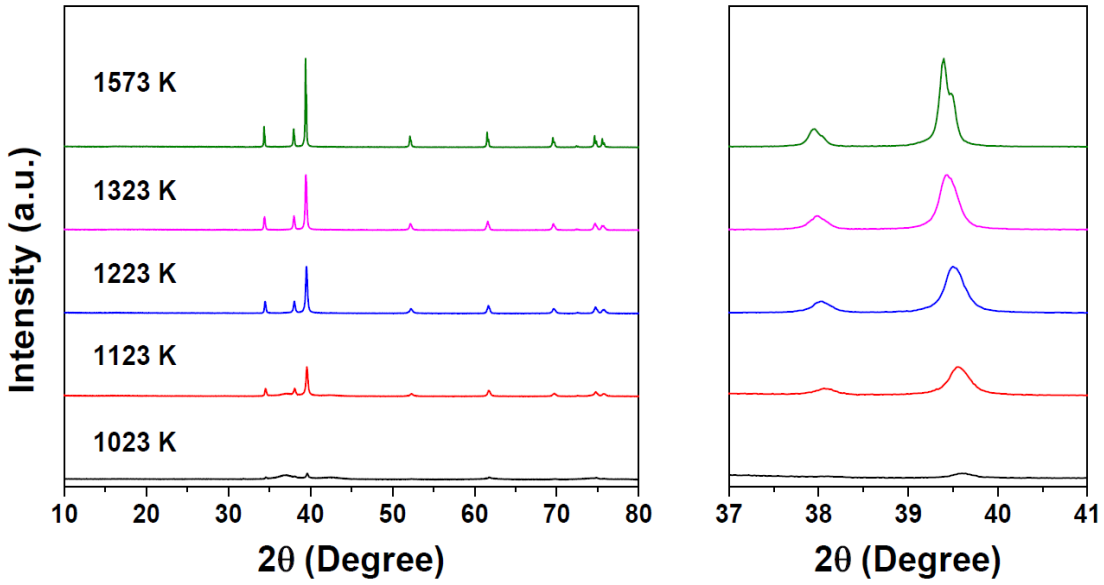

Fig. 2 The effects of the reaction temperature on the XRD patterns of molybdenum carbide–carbon nanocomposites synthesized under N_2 flow.

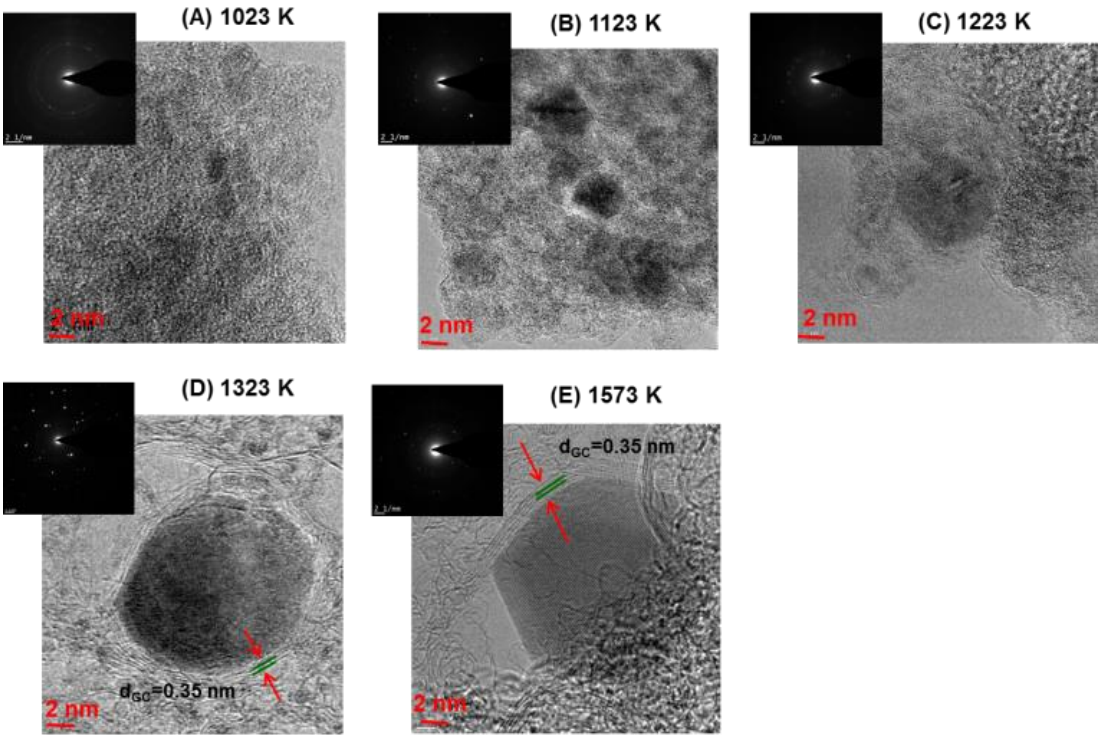

Fig. 3 TEM micrographs of molybdenum carbide–carbon nanocomposites synthesized at different temperatures.

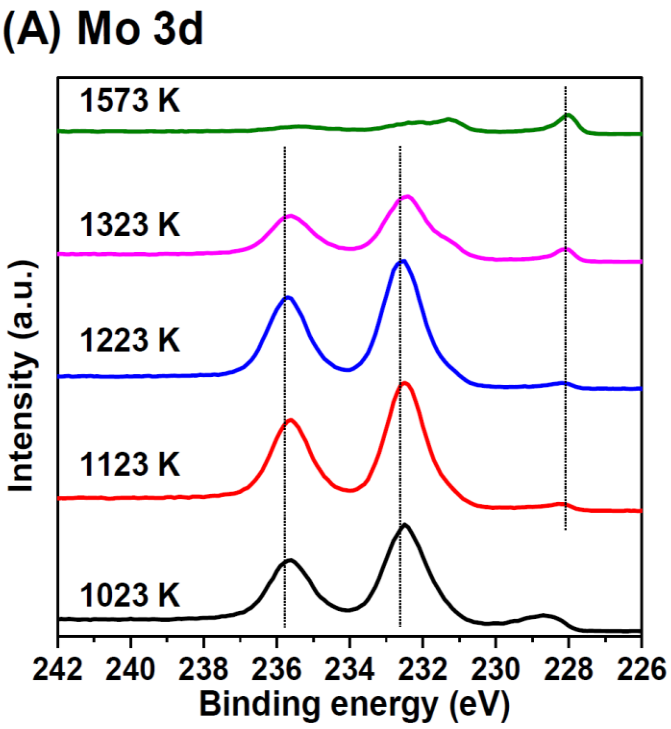
(A) Mo 3d
1573 K
1323 K
1223 K
1123 K
1023 K
Intensity (a.u.)
242 240 238 236 234 232 230 228 226
Binding energy (eV)

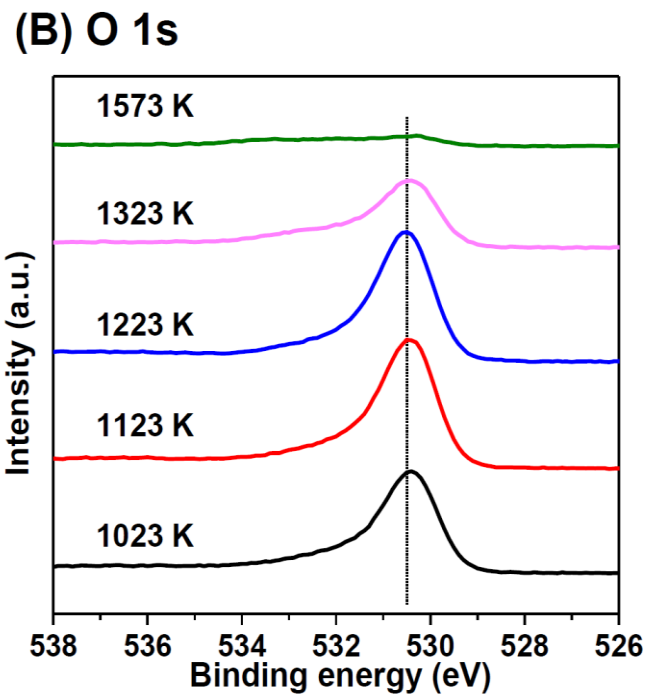
(B) O 1s
1573 K
1323 K
1223 K
1123 K
1023 K
Intensity (a.u.)
538 536 534 532 530 528 526
Binding energy (eV)

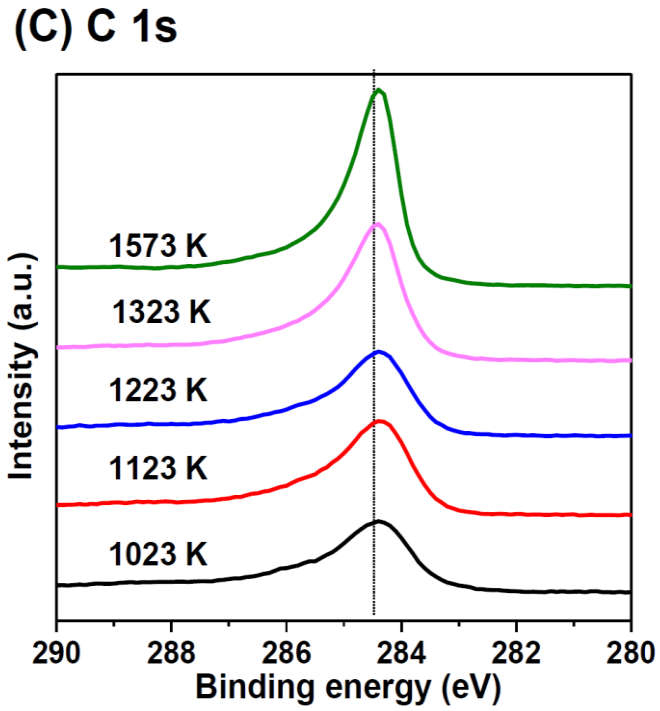

Fig. 4 XPS spectra for (A) Mo 3d (B) O 1s and (C) C 1s of molybdenum carbide–carbon nanocomposites obtained at different temperatures under N_2 flow.

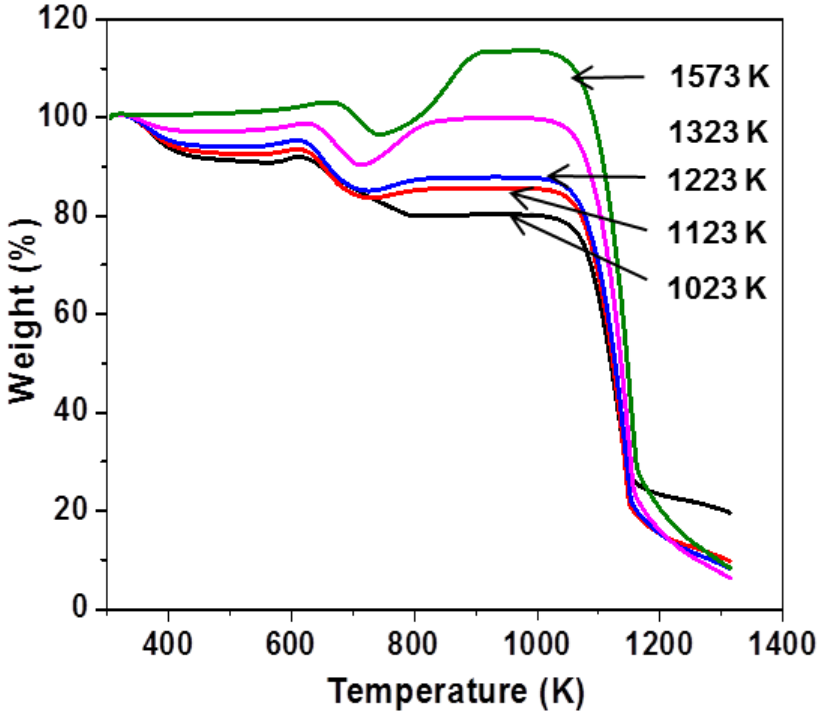

Fig. 5 TGA results of molybdenum carbide–carbon nanocomposites synthesized at different temperatures under air flow.

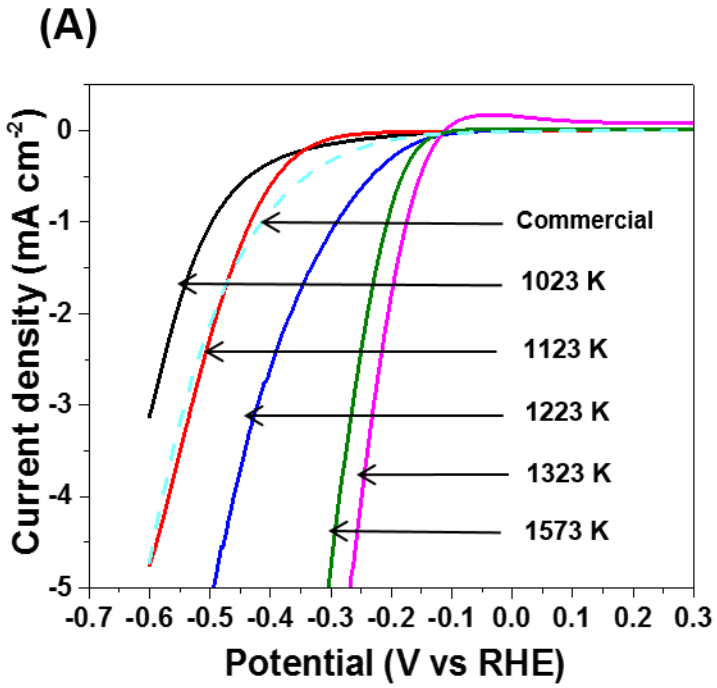

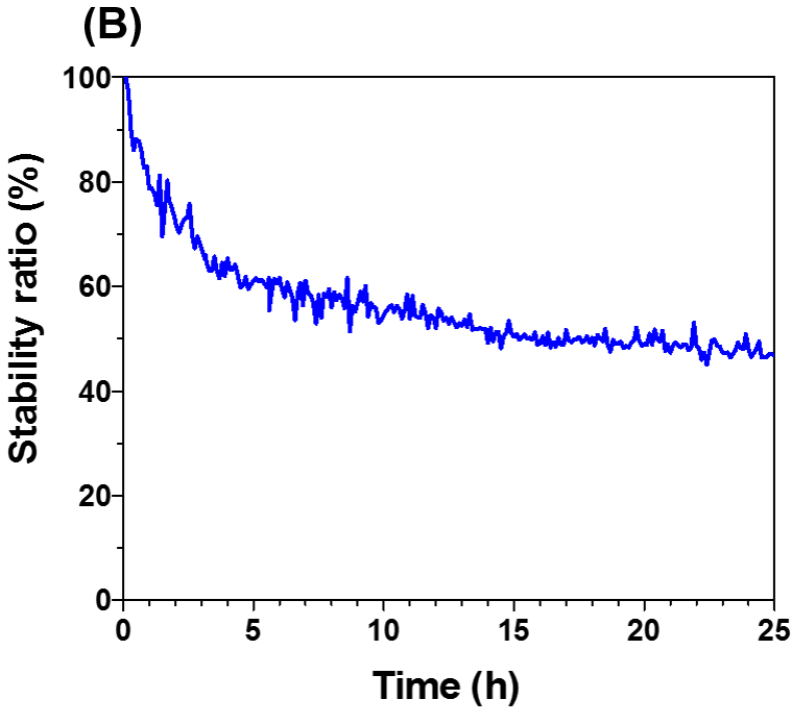
(B)
Stability ratio (%)
Time (h)
0
20
40
60
80
100
0
5
10
15
20
25

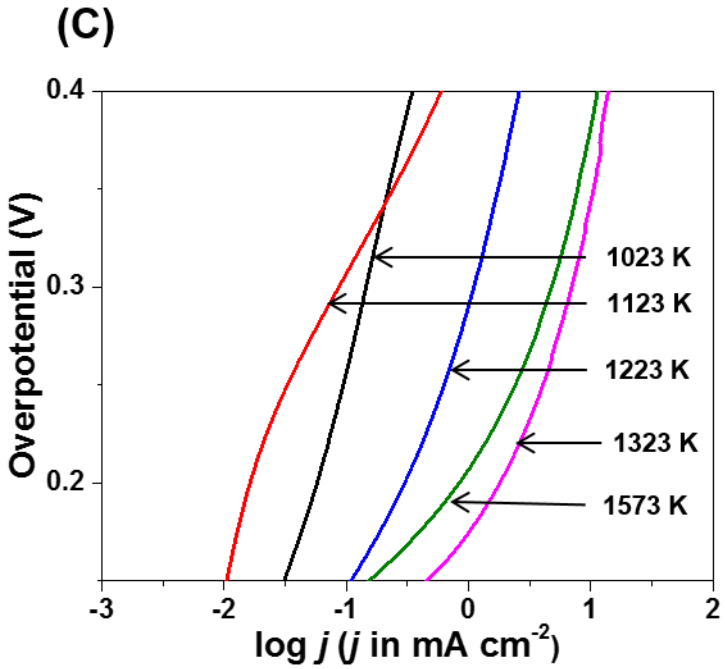
(C)
Overpotential (V)
log j (j in mA cm-2)
0.2
0.3
0.4
-3
-2
-1
0
1
2
1023 K
1123 K
1223 K
1323 K
1573 K

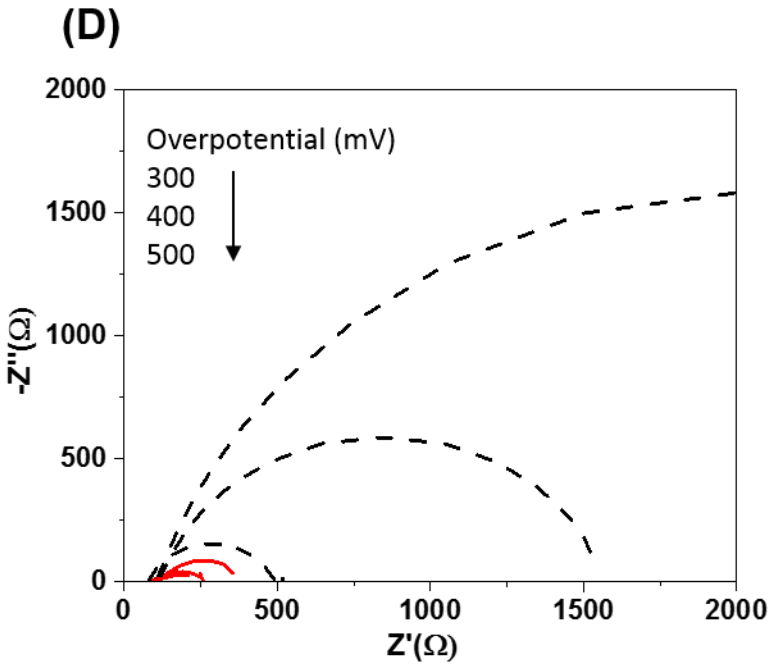

Fig. 6 (A) HER voltammograms of molybdenum carbide–carbon nanocomposites synthesized at different temperatures under N2 flow and commercial Mo2C, (B) stability test of Mo2C synthesized at 1323 K at -0.18 V vs. RHE, (C) HER Tafel plots for the nanocomposites (0.05M H_2SO_4 aq., in Ar, 1600 rpm, 5 mV s^{-1}, 298 K), and (D) Nyquist plot of commercial Mo_2C (black dotted lines) and Mo_2C prepared at 1323 K (red solid lines) recorded at different overpotentials (300, 400 and 500 mV) in 0.05 M H_2SO_4.

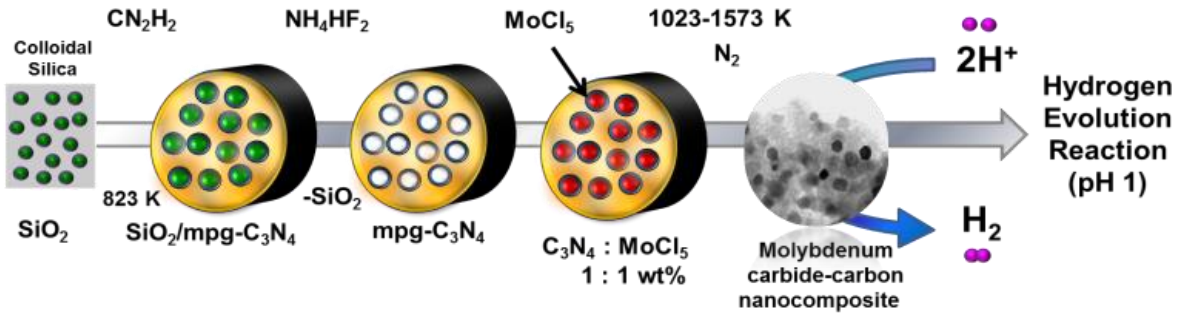

List of tables

Temperature (K) under N_2 flow	C (%)	N (%)	Crystalline size (nm)	BET surface area (m^2/g)	Phase
1023	21	1.3	-	120	Mo_2C
1123	21	0.9	26	141	Mo_2C
1223	22	0.6	27	300	Mo_2C
1323	22	0.4	31	308	Mo_2C
1573	24	0.07	52	277	Mo_2C

Table 1 Synthesis temperature, elemental analyses, phase assignments from the XRD diffractograms, crystallite size evaluations from the Scherrer equation, and BET surface areas for molybdenum carbide–carbon nanocomposites obtained at various temperatures under N_2 flow.

CHAPTER 5

Conclusions

This study introduced a new procedure to synthesize a whole class of interstitial nitride, carbonitride and carbide nanoparticles with size as small as 3 nm through the reaction of a metal precursor with the mpg-C_3N_4 template which acts a confinement for particle formation and as a source of carbon and nitrogen.

Different phases of tantalum based compounds can be produced by altering the reaction conditions. TaN, Ta_2CN, and TaC, with cubic structure, can be formed under a flow of nitrogen by changing the reaction temperatures. Different phases of tantalum nitride, namely TaN and Ta_3N_5, were selectively produced under N_2 and NH_3 flow, respectively. The formation of TaC, Ta_2CN, and TaN can be controlled by altering the weight ratio of the C_3N_4 template relative to the Ta precursor at 1573 K under a flow of nitrogen where high C_3N_4/Ta precursor ratio generally resulted in high carbide content rather than nitride.

In addition, I investigated the reactivity of the transition metals of group IV-VI with the reactive template under a flow of N_2 at different temperatures in the range of 1023 to 1573 K while keeping the weight ratio constant at 1:1. The results show that Ti, V, Nb, Ta, and Cr reacted with mpg-C_3N_4 at 1023 K to form nitride phase with face centered cubic structure. The nitride phase destabilized at higher temperature $\geq$1223 K to form carbonitride and carbide phases. Whereas, Mo and W produce a hexagonal structure of carbide irrespective of the applying reaction temperature. The proved trend is influenced by the reactivity of the transition metals towards nitrogen and carbon fragments which primarily depends on the electronic structure of d-band of the transition metals.

The tendency to form transition metal nitrides and carbides was strongly driven by the free energy of formation. The observed trend indicates that the free energy of formation of nitride is relatively lower for group IV and V transition metals, whereas the carbide phase is thermodynamically more favorable for group VI, in particular for Mo and W. The thermal stability of nitride decreases at high temperature due to the evolution of nitrogen gas.

The electrocatalytic activities of the produced interstitial nitride, carbonitride and carbide nanoparticles were tested for hydrogen evolution reaction in acid media and the results demonstrated that molybdenum carbide nanoparticles exhibited the highest HER current with over potential of 100 mV vs. RHE, among the samples prepared in this study. This result is attributed to the sufficiently small particle size (8 nm on average) and accordingly high surface area (308 m^2 g^{-1}). Also, the graphitized carbon layer with a thickness of 1 nm on its surface formed by this synthesis provides excellent electron path to the catalyst which will improve the rate of electron transfer reaction.

This procedure provides a control over size and shape of the produced nanoparticles which can be achieved by adjusting the size and shape of the original silica used to prepare the reactive template. Thus, this method offers chances to prepare the desired size, shape and phase of transition metal carbide and nitride suitable for a specific reaction which is undoubtedly the optimum objectives in materials chemistry.

Although using mpg-C_3N_4 as a reactive template to synthesize interstitial nitride and carbide nanoparticles is considered to be a successful approach for most of the transition

metals, it shows some limitation when it comes to Zr and Hf. This is attributed to the formation of zirconium and hafnium oxides which are very stable materials which accordingly can not react with nitrogen fragments to produce nitride nanoparticles. In order to overcome the formation of stable oxide, oxygen free solvent should be used and the preparation method is required to be conducted in the glovebox followed by heating using quartz schlenk tube.

In addition, this method leads to the formation of carbon residue in the final product in particular for nitride nanoparticles. However, the amount of resultant carbon residue can be controlled by changing the weight ratio of carbon nitride with respect to a metal precursor. Also, the amount of amorphous carbon increases as the pore size of the template decreases which indicates that the pore size of the template can provide control over the size of the produced nanoparticles as well as the amount of residual carbon. It was observed that heating the product at 600 $^{\circ}$C under a flow of NH_3 was effectively applied to remove the carbon residue. Currently, O_2 plasma treatment is used to eliminate carbon without affecting the phase of the product.

Moreover, caution is required during synthesis as the thermal decomposition of C_3N_4 causes the formation of hydrogen cyanide and cyanogen gasses.

As for the synthetic procedure, a multiple step synthesis was applied in this thesis where mpg-C_3N_4 was synthesized first through heating a mixture of cyanamide with an aqueous colloidal silica suspension composed of silica nanoparticles at 823 K for 4 h. The final mixture was then thoroughly washed with a 4 M ammonium hydrogen difluoride to remove the silica. After that, carbide and nitride nanoparticles were produced through applying a

drop impregnation process on the reactive template and the final mixture was heated at temperature ≥ 1023 K under a flow of nitrogen. It should be mentioned that carbide and nitride nanoparticles can be also synthesized by applying one step method where a metal precursor such as metal oxide is mixed with cyanimide and then pressed into a pellet. After that, the pellet is put into a silica ampoule, evacuated and heated at temperature ≥ 1023 K. During the reaction, cyanamide undergoes condensation process and transformed to g-C_3N_4 that functions as a carbon and nitrogen source to produce nitride and carbide nanoparticles. However, control over size and shape is not possible in this facile route which confirms the importance of the applied synthetic procedure demonstrated in this thesis, in which mesoporous graphite C_3N_4 acts as a confinement for particle growth and provides the required control over size and shape of the resultant nanoparticles that primarily reflects the original size and shape of the silica used to prepare the template.

As for electrocatalytic performance, the presence of oxide on the surface of interstitial nitride and carbide nanoparticles decreases their electrocatalytic activities towards hydrogen evolution reaction. In addition, the interaction of carbide and nitride that have oxidized surfaces with electrolyte under applied potential is complex and in order to understand the actual catalytic site and causes of deactivation of the catalyst, in situ spectroscopic technique such as XPS is required.

The electrocatalytic performance would be further improved through removing the oxide layers from the surface. A possible way is to avoid exposure of the nanoparticles to ambient

air after removing from the furnace and carry out the electrocatalytic measurements under an inert atmosphere.

In addition, there are some strategies to improve the electrocatalytic activities through optimizing hydrogen binding energy by introducing promotors such as Co and Ni in the molybdenum carbide phase. Also, interaction with support such as CNT and graphene.